Author:
Sabines Chesterking, Javier

Title:
Overcoming Practical Limitations to Realise Photonic Quantum-Enhanced Measurements

Overcoming Practical Limitations to Realise Photonic Quantum-Enhanced Measurements

by

Juan Javier Sabines Chesterking

A thesis submitted in partial fulfillment for the degree of

Doctor of Philosophy

in the Faculty of Science

School of Physics

October 2018

Declaration of Authorship

I declare that the work in this dissertation was carried out in accordance with the requirements of the University's Regulations and Code of Practice for Research Degree Programmes and that it has not been submitted for any other academic award. Except where indicated by specific reference in the text, the work is the candidate's own work. Work done in collaboration with, or with the assistance of, others, is indicated as such. Any views expressed in the dissertation are those of the author.

Abstract

In theory, quantum states of lights can be used to perform measurements with a level of precision beyond that which can be attained with their classical counterparts. In practice, they can only do so when the components that we use to generate, manipulate and measure them, operate beyond specific thresholds. In this thesis, we seek to address different obstacles that hinder our ability to fully exploit quantum-metrological schemes. We mainly focus our attention in quantum-enhanced optical transmission measurements. For this we make use of photon pair sources and take advantage of the photon number correlations of the sources to suppress noise in parameter estimation. With this approach we are able to reach a level of precision beyond the shot-noise limit without the use of post-selection. We achieve this by implementing feed-forward and using a CCD camera with high detection efficiency. We have been able to obtain measurements of transmission with a maximum factor of advantage of 1.66 when compered to an ideal classical experiment using a noiseless coherent source and a 100% efficient detector. We have also studied the roll of photon distinguishability in quantum-enhanced phase estimation, where we have performed experiments with two and four-photons states controlling their level of distinguishability and we demonstrate that fully indistinguishable photons are not required to obtain quantum-enhanced measurements.

Acknowledgements

I would like to start by thanking Jonathan Matthews for supervising me throughout my PhD. You have done a fantastic job supervising me and all of your students. We are all very grateful for that.

I would also like to thank everyone else in QET Labs for their support and friendship.

Gracias a Lorena por ser y por estar siempre presente. Y ante todo gracias a mi familia; sin ustedes nada de esto hubiese sucedido y nada de esto tendría sentido.

A mi familia.

Manuscripts

† Indicates manuscripts which are part of this thesis.

- † *Sub-Shot-Noise Transmission Measurement Enabled by Active Feed-Forward of Heralded Single Photons.*
  Sabines-Chesterking, J., Whittaker, R., Joshi, S. K., Birchall, P. M., Moreau, P. A., McMillan, A., ... & Matthews, J. C. F.
  Physical Review Applied, 8(1), 014016, (2017).

- † *Demonstrating an absolute quantum advantage in direct absorption measurement.*
  Moreau, P. A., Sabines-Chesterking, J., Whittaker, R., Joshi, S. K., Birchall, P. M., McMillan, A., ... & Matthews, J. C. F.
  Scientific Reports, 7(1), 6256, (2017)

- † *Beating the Shot-Noise Limit with Sources of Partially-Distinguishable Photons*
  Patrick M. Birchall, Javier Sabines-Chesterking, Jeremy L. O'Brien, Hugo Cable, Jonathan C. F. Matthews
  arXiv:1603.00686 (2016)

- *Optical implementation of spin squeezing.*
  Ono, T., Sabines-Chesterking, J., Cable, H., O'Brien, J. L., & Matthews, J. C.
  New Journal of Physics, 19(5), 053005, (2017).

Presentations

- *Achieving sub-shot-noise absorption-spectroscopy with avalanche photodiodes and with a charge-coupled device.*
  Sabines-Chesterking J., Whittaker R., Moreau P.-M., McMillan A., Joshi S., Birchall P., ... &Matthews J. C. F
  CLEO, San Jose, California United States, 5-10 June (2016). (Talk)

- *Achieving sub-shot-noise absorption-spectroscopy with avalanche photodiodes and with a charge-coupled device.*
  Sabines-Chesterking J., Whittaker R., Moreau P.-M., McMillan A., Joshi S., Birchall P., ... &Matthews J. C. F
  Quantum 2017, Turin, Italy, 7-13 May (2017). (Talk)

- *Achieving sub-shot-noise absorption-spectroscopy with avalanche photodiodes and with a charge-coupled device.*
  Sabines-Chesterking J., Whittaker R., Moreau P.-M., McMillan A., Joshi S., Birchall P., ... &Matthews J. C. F
  Photon 16, Leeds, UK, 5-8 September (2016). (Poster)

Contents

List of Figures

Chapter 1

Introduction and Outline

1.1 Introduction

Advancements in science and technology come hand in hand with new developments on our ability to perform more precise and accurate measurements. Breakthroughs in metrology open new scientific horizons and have far-reaching influence in different fields of science. In the past three decades, measurement and sensing schemes that exploit quantum phenomena have been put forth, promising a vast range of applications. From interferometry with squeezed states of light for gravitational wave detection[1] to super-resolution microscopy [2], quantum enhanced tools offer the possibility to overcome classical limits of sensitivity. The road from conception to applications for these tools has now gone beyond the stage of proof of principle. We are now at a point where we need to focus our attention in engineering these technologies so that they come out of the physics laboratory and become part of our scientific tool-box with which we can measure objectswe produce, explor our enviroment and investigate the universe.

In the present thesis we set our efforts on overcoming some pertinent practical limitations in quantum enhanced optical metrology. In particular we have centered our attention in performing optical measurements of transmission with precision that goes beyond the

shot-noise limit. We have realized a series of experiments that address well known obstacles in optical quantum metrology, such as post-selection, inefficient detection of photons and distinguishability. We expect that our efforts help to bridge the gap between the development of new quantum technologies and their real-life applications.

1.2 Thesis outline

The work presented throughout this thesis is my contribution to a collaborative effort. Hence, my personal contributions are outlined at the beginning of each chapter. This thesis is written in a way such that chapters are self contained, in some cases notation might differ between chapters. Whenever there is a change in notation there will be a footnote stating the differences.

Chapter 2 contains the theoretical background that supports the rest of the thesis. It contains a review of parameter estimation using Fisher information, a brief description of different quantum states of light and their statistics, an overview of spontaneous parametric down conversion, a description of some optical effects that are used throughout the experiments and a brief description of the detectors used in the experiments.

In chapter 3 we report the construction of a polarization independent optical switch to implement feed-forward on a heralded single-photon source based on spontaneous parametric down conversion. With this we perform a quantum enhanced transmission estimation protocol without using post-selection.

In chapter 4 we use the tools developed in chapter 3 and appendix A to build a raster-scanning microscope using a photon-pair source. Here we use a hybrid detection scheme combining and avalanche photo-diode that provides time of arrival information and enables heralding single photons with which we then image and object and then detect them with a high efficiency CCD camera. With these tools we were able to record images below the shot-noise-limit. The results presented in this chapter also present an absolute quantum advantage.

In chapter 5 we optimize the coupling efficiency of an spontaneous parametric down conversion source by manipulating the spatial shape of the pump beam. This was achieved using a spatial light modulator running a genetic algorithm.

In chapter 6 we investigate the roll of photon distinguishability in quantum enhanced phase measurements. We show this analytically and demonstrate it experimentally using a multi-photon down conversion source pumped with a pulsed laser. We show how states containing partially-distinguishable photons can achieve quantum-enhanced sensitivity even when presenting low-visibility quantum interference. This in stark contrast to other experimental imperfections as for example loss.

In chapter 7 we summarize our results and provide conclusions and outlook for the tools developed throughout this thesis.

In appendix A we make use of a high efficiency CCD camera and the down conversion sources reported in chapter 3 to perform a quantum enhanced transmission measurement with an absolute advantage. This in contrast to the results in chapter 3 where there would be no quantum advantage if we compared our results to with an ideal (noiseless) coherent state measured with a 100% efficient detector. This chapter provides context to the results in chapter 5 and highlights the difference between a quantum advantage when compared to a classical scheme using inefficient detectors and an absolute quantum advantage.

Chapter 2

Background

2.1 Parameter estimation and Fisher information

When we perform an experiment to determine a parameter or a set of parameters, from a sample it is not always the case that the outcomes of the experiment would directly give us the desired information. In general we need to estimate the parameter from a finite set of experimental outcomes which not necessarily lead to the true value of the parameter under investigation. In particular, the statistical nature of quantum mechanics imposes limits on the precision with which we could measure a physical system using a quantum probe. A quantum mechanical measurement scheme is depicted in Fig. 2.1

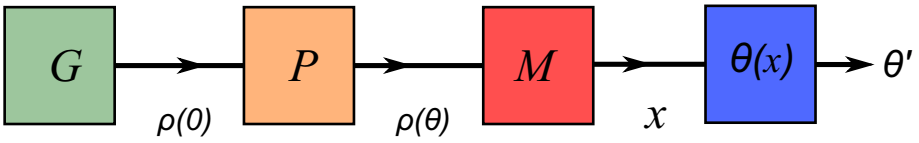

FIGURE 2.1: **Schematic of the parameter-estimation procedure.** A procedure G generates a probe state, $\rho(0)$, then the process under study, P (which is dependent on θ), evolves the state into $\rho(\theta)$. Then a positive-operator valued measure (POVM), M, yields an outcome x from which we estimate the parameter under investigation θ obtaining an estimate value θ' .

For example, let us consider an experiment where the goal is to estimate a single parameter θ. The experiment would consist of a series of measurements of an observable, which is

dependent on θ, with the outcomes x, following a probability distribution $p(\theta|x)$. Then we can extract the value of θ using a function of x also known as an estimator: $\Theta(x)$. Estimators are not unique and may not return the true value of the parameter under investigation, for this reason it is necessary to construct a framework with which we could determine the precision of an estimator. The performance of a given estimator is quantified by the mean square error (MSE) from the true value of the unknown parameter

$$\Delta^2\Theta = \langle(\Theta(x) - \theta)^2\rangle = \int p(x|\theta)(\Theta(x) - \theta)^2 dx. \tag{2.1}$$

We expect that, on average the estimator will yield the true value of the parameter θ. When this is true we say that the estimator is unbiased:

$$\langle\theta\rangle = \int p(x|\theta)(\Theta(x)) = \theta. \tag{2.2}$$

We refer to an estimator as optimal if it is unbiased and is one that minimizes $\Delta\Theta^2$ for all θ. Finding the right estimator is not a simple task, still, one may always construct a lower bound for the MSE of any unbiased estimator, this is known as the Cramér-Rao lower bound (CRB) [3]:

$$\Delta\Theta^2 \geq \frac{1}{F(\theta)}, \tag{2.3}$$

where F is the Fisher information, expressed as:

$$F(\theta) = \int dx \frac{1}{p(x|\theta)} \left(\frac{\partial p(x|\theta)}{\partial\theta}\right)^2. \tag{2.4}$$

Since $F(\theta)$ is a function of $p(x|\theta)$, which in turn is determined by the state of the system $\rho(\theta)$ and a POVM $\hat{E}_x$, this means we need to construct probes with suitable states and observables to perform a measurement [4]. However, for a given experiment, with a

chosen set of observables, whose estimator saturates the CRB, there might be a different set of observables with their respective estimator that would yield a higher precision. We can construct a mathematical framework for general POVMs, this is the also known as quantum Fisher information. Quantum Fisher information differs significantly in the operational sense due the fact that the probability $p(x|\theta)$ results from measurement by the quantum operator $E(x)$ rather than a mere classical experiment [5]. According to BornâĂŹs rule,$p(x|\theta) = \mathrm{Tr}[E(x), \rho_\theta]$ represents the conditional probability of obtaining the outcome x when the given value of the parameter is θ. In the quantum world, the parameter estimation problem can be thought of as the problem of searching for the set of measurements $E(x)$ that yields the optimal value of (1). Therefore, the quantum Fisher information can be defined as

$$\mathcal{F}_\theta = \max F_\theta \tag{2.5}$$

Further, using the notion of symmetric logarithmic derivative (SLD) introduced in [6] we obtain an alternate expression for the QFI.

$$\Delta\Theta^2 \geq \frac{1}{\mathcal{F}(\rho_\theta)}, \tag{2.6}$$

where $\mathcal{F}$ is the quantum Fisher information (QFI) defined as:

$$\mathcal{F} = \mathrm{tr}\left[\rho_\theta \mathcal{L}_\theta^2(\rho_\theta)\right], \tag{2.7}$$

and $\mathcal{L}$ is the symmetric logarithmic derivative, which can be defined for any state ρ_θ via the relation:

$$\dot{\rho}_\theta = \frac{1}{2}\left(\rho_\theta \mathcal{L}_\theta + \mathcal{L}_\theta \rho_\theta\right). \tag{2.8}$$

It is important to notice that the QFI is only determined by the dependence of ρ_θ on the estimated parameter and therefore we can estimate the sensitivity of a probe state

without considering any particular POVM nor estimator [3]. There is an explicit expression for $\mathcal{L}_\theta$ in terms of the eigenvalues and eigenvectors of the probe's density matrix $\rho_\theta = \sum_i p_i(\theta \left|\psi(\theta)\right\rangle \left\langle\psi(\theta)\right|)$:

$$\mathcal{L}(\rho_\theta) = \sum_{i,j} \frac{2}{p_i + p_j} \left\langle\psi_i\right| \frac{\partial \rho_\theta}{\partial \theta} \left|\psi_j\right\rangle \left|\psi_i\right\rangle \left\langle\psi_j\right| . \tag{2.9}$$

For a pure state where the parameter is encoded by a unitary operator $\left|\psi(\theta)\right\rangle = e^{i\hat{H}\theta} \left|\psi\right\rangle$ the quantum fisher information simplifies to:

$$\mathcal{F}(\psi_\theta) = 4\left(\left\langle\psi\right| \hat{H}^2 \left|\psi\right\rangle - \left\langle\psi\right| \hat{H} \left|\psi\right\rangle^2\right) = \mathrm{Var}_\psi(\hat{H}), \tag{2.10}$$

so that, for the pure state estimation case, the QFI is proportional to the variance of $\hat{H}$ and the quantum Cramér-Rao bound takes the form of a energy-time uncertainty relation [3]:

$$\Delta^2\theta \Delta^2 H \geq \frac{1}{4N}, \tag{2.11}$$

where N is the number of times the measurement was repeated.

In conclusion, determining the QFI can help us explore alternative measurement schemes, an example of this can be found in [7, 8] although in does not give much information about the practicality of these alternatives. On the other hand FI is a good metric to understand the performance of a defined experimental technique with a chosen set of POVMs and it could also be useful when compared to the QFI so that we can understand how far are we from an ideal measurement scheme.

2.2 Quantum-states of light

Investigating the properties of a sample where light is used as probe require measurements of either the transmissivity, phase, absorption, position, or deflection of a light beam. These measurements are all bounded by classical limits being either the shot-noise or the Rayleigh limit. There are different quantum states that can overcome these limits. Through out this work we are mostly interested in states that are used to obtain an advantage in transmission and phase estimation with regards to the shot noise limit.

The precision of optical measurements which rely on precisely quantifying the intensity of a beam of light are subject to many different sources of noise like electronic Shot-noise in photo-detectors, background light, mechanical instabilities and others but fundamentally these measurements are limited by the noise in the photon-number distribution of the source of light. In the following subsections we will briefly discus the photon-number statistics of Fock states, and coherent states due to there relation to photon counting based metrological schemes.

2.2.1 Fock States

We will start with Fock states since they serve as a basis to represent any arbitrary state and operator of the electromagnetic field [9].

Fock states are states of light with a fixed number of photons, they are the eigenstates of the photon-number operator $\hat{n}$

$$\hat{n}\,|n\rangle = n\,|n\rangle\,, \tag{2.12}$$

where $\hat{n} = \hat{a}^\dagger \hat{a}$ is defined in terms of the creation operator $\hat{a}^\dagger$ and the annihilation operator $\hat{a}$ which act on a number state according to

$$\begin{aligned} \hat{a}^\dagger |n\rangle &= \sqrt{n+1}\, |n+1\rangle\,, \\ \hat{a}\, |n\rangle &= \sqrt{n}\, |n-1\rangle\,. \end{aligned} \tag{2.13}$$

So that an arbitrary Fock state, $|n\rangle$, can be expressed by applying the creation operator n times on a vacuum state

$$|n\rangle = \frac{\hat{a}^{\dagger n}}{\sqrt{n!}} |0\rangle\,. \tag{2.14}$$

The probability of detecting n photons in a Fock state, $|n\rangle$, is given by $P(n) = \delta_{n1}$. This means that the variance of the photon-number distribution of a Fock state is zero, making them an ideal probe state for experiments based on intensity measurements [10]. However, in practice it is challenging if not impossible to generate and manipulate Fock states since any optical component that introduces loss would degrade the state into a mixture. For example the state $|1\rangle$ would degrade with loss into

$$\hat{\rho} = (1-p)\, |0\rangle \langle 0| + p\, |1\rangle \langle 1|\,, \tag{2.15}$$

where p is the probability of detecting the state $|1\rangle$ and $(1-p)$ could be understood as the loss in the channel where $|1\rangle$ propagates. This type of states are alsoreferred to as binomial states of light since they follow a binomial photon-number distribution [11]. In general these states are described by the density matrix

$$\hat{\rho} = \sum_n p_n\, |n\rangle \langle n|\,, \tag{2.16}$$

Having a probability distribution given by

$$p(n) = \binom{N}{n} \eta^n (1-\eta)^{N-n}, \tag{2.17}$$

where η and $(\eta - 1)$ are the probabilities of the two possible outcomes of a Bernoulli trial and N is the total number of trials. Binomial states lie in between the coherent state, the most classical state allowed in quantum theory and the less classical one the Fock state [12].

2.2.2 Coherent States

In classical optics, light is described by a electromagnetic wave with a well defined and constant phase. A quantum optical description of such a wave would require to build upon a bridge between the classical and the quantum model. This is best done by a coherent state of light. Coherent states describe the state of a quantum harmonic oscillator.Mathematically a coherent state is defined as the eigenstate of the annihilation operator

$$\hat{a}\,|\alpha\rangle = \alpha\,|\alpha\rangle\,. \tag{2.18}$$

It can also be expressed in terms of a linear superposition of Fock states [9]

$$|\alpha\rangle = \sum_{n=0}^{\infty} C_n\,|n\rangle\,. \tag{2.19}$$

Where if $\hat{a}$ acts on Eq.2.19 we get

$$\hat{a}\,|\alpha\rangle = \sum_{n=0}^{\infty} C_n\sqrt{n}\,|n-1\rangle = \alpha\sum_{n=0}^{\infty} C_n\,|n\rangle\,, \tag{2.20}$$

equating coefficients of $|n\rangle$ in the two series expressions of Eq.2.20 and dividing through by $\sqrt{n}$

$$C_n\sqrt{n} = \frac{\alpha}{\sqrt{n}}C_{n-1}, \tag{2.21}$$

leading to

$$|\alpha\rangle = C_0 \sum_{n=0}^{\infty} \frac{\alpha^n}{\sqrt{n!}} |n\rangle \tag{2.22}$$

From normalization requirements on $|\alpha\rangle$ we obtain that $|C_0| = e^{\frac{-|\alpha|^2}{2}}$ so that we could express $|\alpha\rangle$ as

$$|\alpha\rangle = e^{-\frac{1}{2}|\alpha|^2} \sum_{n=0}^{\infty} \frac{\alpha^n}{\sqrt{n!}} |n\rangle \,. \tag{2.23}$$

So when we calculate the probability of detecting n photons in α we get:

$$p_n = |\langle n|\, \alpha\rangle|^2 = \frac{|\alpha|^{2n}}{n!} e^{-|\alpha|^2}, \tag{2.24}$$

from 2.24 we notice that a coherent state has Poissonian photon statistics with an average number of photons $|\alpha|^2$.

2.2.3 NOON states and Holland-Burnett states.

In this subsection we will discuss quantum states that have an advantage for estimating an optical phase. An example of such states are $NOON$ states. A $N00N$ state is the superposition of a number state between two distinct modes, where $n > 1$. It is mathematically be expressed as [13]:

$$|\psi\rangle_{N00N} = \frac{|N\rangle_a |0\rangle_b + |0\rangle_a |N\rangle_b}{\sqrt{2}}. \tag{2.25}$$

To understand the advantage in phase sensitivity using NOON states, let us compare the difference between the output state of a coherent and a $NOON$ state entering a Mach-Zehnder interferometer (MZI). If we inject a classical state of light into a MZI, we can

deduce a phase shift by computing the difference in intensity at the output ports, a and b, of the interferometer $M = I_a - I_b = I_{IN} \cos\varphi$. Mathematically we can describe the effect of the interferometer in terms of the unitary evolution of a state acquiring a phase described by $\hat{U}(\varphi) = e^{i\phi\hat{n}}$

$$\begin{aligned} \hat{U}_\varphi |\alpha\rangle &= e^{i\varphi} |\alpha\rangle , \\ \hat{U}_\varphi |N\rangle &= e^{iN\varphi} |N\rangle . \end{aligned} \tag{2.26}$$

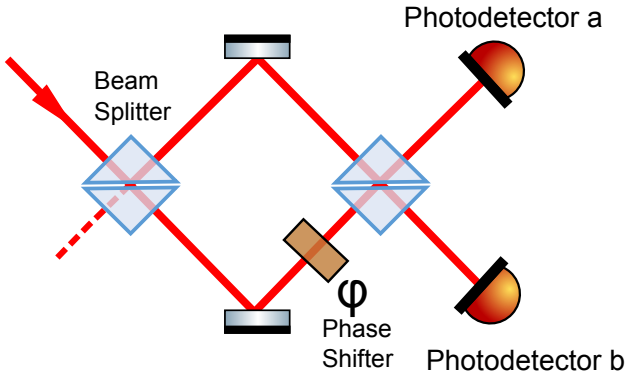

FIGURE 2.2: **Mach-Zehnder interferometer.** A Mach-Zehnder interferometer is a device used to measure the phase difference between two spatial modes of light which originally come from a single spatial mode that has been divided and recombined using beam splitters. At the output of the interferometer we obtain a phase dependent intensity in ports a and b.

We notice from 2.26 that the behavior of a $NOON$ state after the phase shifter is very different from that of a coherent state. The action of a phase shifter operator on a coherent states is independent of the number of photons, however there is an N dependence on the phase when it is applied to a $NOON$ state. This means that the phase of a $NOON$ states in a MZI evolves N times faster than the phase of a coherent states. The resulting effect of $NOON$ states is equivalent to having photons with an effective wavelength of λ/N.

We can also notice from figure 2.3 that the slope at the crossing point with the horizontal axis of $NOON$ states is steeper. This translates into a greater accuracy of a phase estimation. Which in the classical case is limited by our ability to measure the intensity

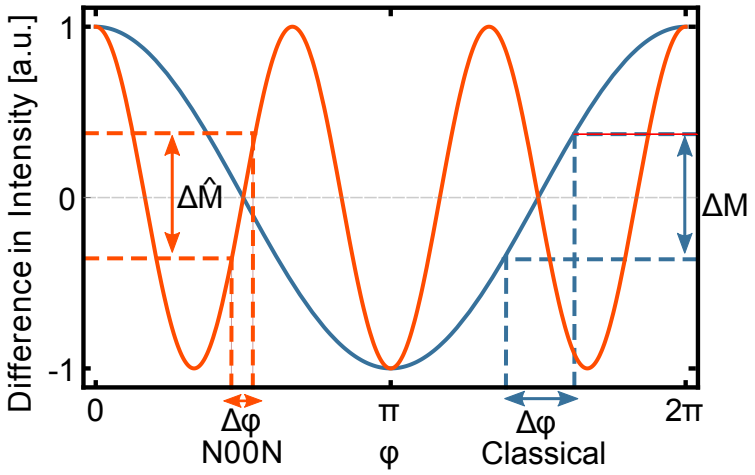

FIGURE 2.3: **Simulated interference fringes in a Mach-Zehnder interferometer** The graph shows a comparison between the interference fringes using as an input a coherent state (blue) and a $N = 3$ $N00N$ state (orange). In the figure ΔM is the difference in intensity between the output arms of the MZI. Adapted from [13].

difference between the arms of the MZI i.e., the shot noise limit $\Delta\varphi = 1/\sqrt{N}$. In the case of $NOON$ states we are counting photons N at a time, where $\Delta M_{NOON} = 1/N$, in this case the precision on φ would be

$$\Delta\varphi_{NOON} = 1/N, \tag{2.27}$$

which is equal to the Heisenberg limit following the uncertainty relation between phase and number of photons [13].

Generating $NOON$ states is experimentally challenging and they are difficult to manipulate, they are extremely fragile since loosing one photon in either mode would collapse the state turning them obsolete. Therefore Holland-Burnett (HB) states are commonly used to approximate NOON states [14–16]. Holland-Burnett states are defined as the dual Fock states $|\psi\rangle_{HB} = |n, n\rangle$, in general terms they are described by the density operator

$$\rho = \sum_n c_n \, |nn\rangle \, \langle nn| \tag{2.28}$$

HB states can be generated from multi-photon pairs using spontaneous parametric down conversion (SPDC). When the two beams of an SPDC process with $n/2$ photons each, $|n/2, n/2\rangle$, are injected into the input ports of a MZI interferometer we get the following state after it passes through the first beam splitter of the interferometer and the phase shifter

$$|\psi\rangle_{HB} \rightarrow \sum_{n=0}^{n/2} C_n \, |2n, n-2n\rangle \tag{2.29}$$

where C_n is given by

$$C_n = \frac{\sqrt{(2n!)(N-2n)!}}{2^{n/2} n! \, (n/2-n)!} e^{2in\varphi} \tag{2.30}$$

Due to photon bunching arising from nonclassical interference, the uncertainty of the photon number difference between the paths inside the interferometer is $\sqrt{n(n+2/2)}$. So we could say that HB states approximate $NOON$ states in that they can achieve Heisenberg scaling for phase estimation [15].

2.3 A source of quantum states of light: Spontaneous parametric down-conversion.

Experimental demonstrations and applications of optical quantum effects require single photon sources. In an ideal scenario a single photon source would emit indistinguishable photons, with a small spectral bandwidth, on demand, in a single spatial mode, with low probability of multi-photon events, high repetition rates and with a high emission efficiency [17]. There are many different single photon sources available including quantum dots, atomic cascades, attenuated lasers, nitrogen vacancy centers (NV centers), and spontaneous parametric sources like four wave mixing (FWM) and spontaneous parametric down-conversion (SPDC). All of them have advantages and disadvantages but the

workhorse for proof of principal experiments in quantum optics and the one used throughout this work is SPDC. Parametric down-conversion satisfies most of the aforementioned requirements, there biggest drawback is that the emission process is probabilistic. Since the generation process in SPDC comes in pairs of photons we could herald a photon by detecting the presence of its companion and multiplex various sources to turn them into semi-deterministic sources, this process, also referred as feed-forward, is a technique used in the experiment presented later in Chapter 3.

SPDC is a non-linear effect in which a second order non-linear material is illuminated with a bright pump beam. Pump photons are then absorbed by the material and spontaneously remitted as photon pairs, commonly referred to as signal and idler. The re-emited photon pairs are constrained by energy and momentum conservation conditions

$$\begin{aligned} \omega_s + \omega_i &= \omega_p, \\ k_s + k_i &= k_p. \end{aligned} \tag{2.31}$$

This means that the sum of the energy (momentum) of the down-converted photons would add up to the energy (momentum) of the parent pump photon.

Creating the conditions under which momentum conservation is possible is called phase matching. Phase matching can be achieved using birefringent materials where the distinct wavelengths (λ) involved in the process travel with different refractive indices given by the Sellmeier equation

$$n_E(\theta, \lambda) = \frac{1}{\sqrt{\left(\frac{\sin(\theta)}{n_e(\lambda)}\right)^2 + \left(\frac{\cos(\theta)}{n_o(\lambda)}\right)^2}}, \tag{2.32}$$

where n_e is the refractive index of the extraordinary polarization (along the crystal axis), n_o the refractive index for ordinary polarization (perpendicular to the crystal axis) and

(θ) between the direction of propagation and the crystal axis. Eq. 2.32 determines the type of emission of the SPDC process: colinear or non-colinear, Type-I (pump and down-converted photon have perpendicular polarizations) or Type-II (signal and idler photons have perpendicular polarizations).

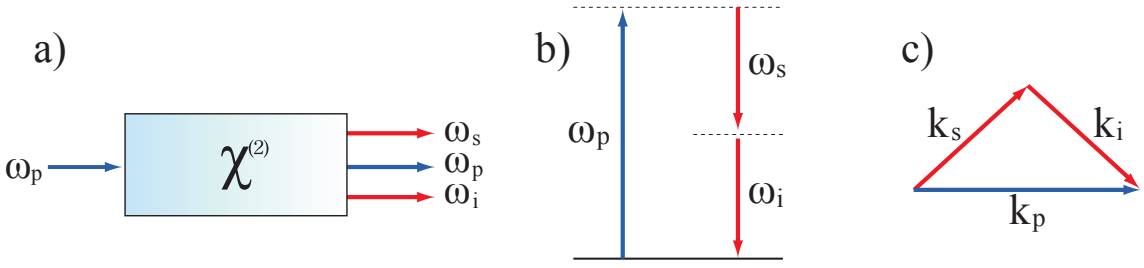

FIGURE 2.4: **SPDC and conservation conditions.** a)SPDC interaction diagram. In a SPDC process a pump photon with frequency ω_p and wave vector k_p splits into two photons with frequencies ω_s and ω_i and wave vectors k_s and k_i. b) Energy conservation. c) Momentum conservation.

Aligning a crystal to satisfy phase matching conditions is challenging, and the spectral range which can be phase-matched is small. An alternative method to achieve phase matching using birefringent materials is by designing a material that allows a phase mismatch, but compensates it by using a position dependent periodic non-linearity. In this instance it is not necessary to have different polarization states of the involved waves. This method is usually referred to as quasi phase-matching (QPM). QPM does not modify the energy conservation conditions but it does change the momentum conservation by introducing an extra term, $K = 2\pi/\Lambda$

$$k_p = k_i + k_s + K, \tag{2.33}$$

where Λ is the poling period of the material. The down-conversion spectrum of a QPM crystal can be tuned by controlling the temperature of the crystal. This in turn would generate a thermal expansion effectively changing the value of Λ. Throughout this thesis we have used a periodically poled potassium titanyl phosphate (PPKTP) crystals phase matched to down-convert 404 nm light into 808 nm with a poling period of $\Lambda \approx 10$ μm at 25° C.

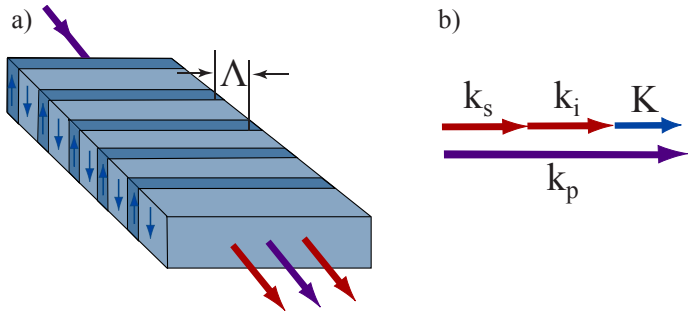

FIGURE 2.5: **Quasi phase matching.** a)Periodic poling of nonlinear material. b) Momentum conservation for QPM.

SPDC is very similar process to optical parametric amplification, only that in the case of SPDC vacuum is amplified rather than a seeding beam. A full treatment of the theory of SPDC can be found in [18]. Here, we only derive the output state of the process, following the treatment in [19], given the interaction Hamiltonian $\hat{H} = i\xi\hat{a}_s^\dagger\hat{a}_i^\dagger + i\xi^*\hat{a}_s\hat{a}_i$, where ξ contains properties of both the pump and the non-linearity. In this case when the evolution operator, $\exp\left[-i\hat{H}t\right]$, acts on a vacuum $|0,0\rangle_{s,i}$ we obtain:

$$
\begin{aligned}
|\psi\rangle_{\text{SPDC}} &= \hat{U}\,|0,0\rangle_{s,i} \\
&= \exp\left[-i\hat{H}t\right]|0,0\rangle_{s,i} \\
&= \exp\left[-it(i\xi\hat{a}_s^\dagger\hat{a}_i^\dagger + i\xi^*\hat{a}_s\hat{a}_i)\right]|0,0\rangle_{s,i} \\
&= \sum_{j=0}^{\text{inf}} \frac{\gamma^j}{j!}(\hat{a}_s^\dagger)^j(\hat{a}_i^\dagger)^j\,|0,0\rangle_{s,i} \\
&= \sum_{j=0}^{\text{inf}} \gamma^j\,|j,j\rangle_{s,i} \\
&= |0,0\rangle_{s,i} + \gamma\,|1,1\rangle_{s,i} + \gamma^2\,|2,2\rangle_{s,i} + ... + \gamma^n\,|n,n\rangle\,,
\end{aligned}
\tag{2.34}
$$

where $\gamma = \xi t$ is the gain parameter and $|\gamma|^2$ is probability of pump photon conversion to down-converted photons. In the low gain regime, $\gamma << 1$, so the SPDC state can be reduced to the following approximation:

$$|\psi\rangle_{\text{SPDC}} = |0,0\rangle_{s,i} + \gamma\,|1,1\rangle_{s,i} \tag{2.35}$$

In Chapter 6 we perform an experiment using a pulsed laser where γ is sufficiently high to observe 4 photon events. In the rest of this work experiments operate under conditions where higher order terms are negligible.

2.4 Optical effects

2.4.1 Pockels effect

As discussed in the previous section SPDC can be used as a single photon source, SPDC and other parametric sources have the disadvantage of generating photons at random times. One way of turning a spontaneous source into a pseudo-deterministic source is by heralding [20]. When a protocol requires that a single-photon should only be delivered conditionally on the successful detection of its correlated pair it is necessary to introduce a delay and a fast optical switch, this procedure is called feed-forward [21, 22]. There are many different ways to perform optical switching, in Chapter 3 we will describe an experiment that uses an electro-optic effect to operate a fast optical switch. In this section we will briefly discuss the Pockels effect which is what our switch was based on.

The Pockels effect or linear electro-optic effect is the change of the refractive index of a medium due to an external electric field. The effect is linearly proportional to the applied electric field strength

Mathematically, the Pockels effect is best described via the induced deformation of the index ellipsoid,

$$1 = \sum_{j=1}^{3} \frac{x_j^2}{n_{x_j}^2} + \begin{bmatrix} x_1^2 & x_2^2 & x_3^2 & 2x_1x_2 & 2x_1x_3 & 2x_2x_3 \end{bmatrix} \begin{bmatrix} r_{11} & r_{12} & r_{13} \\ r_{21} & r_{22} & r_{23} \\ r_{31} & r_{32} & r_{33} \\ r_{41} & r_{42} & r_{43} \\ r_{51} & r_{52} & r_{53} \\ r_{61} & r_{62} & r_{63} \end{bmatrix} \cdot \begin{bmatrix} E_1 \\ E_2 \\ E_3 \end{bmatrix}, \tag{2.36}$$

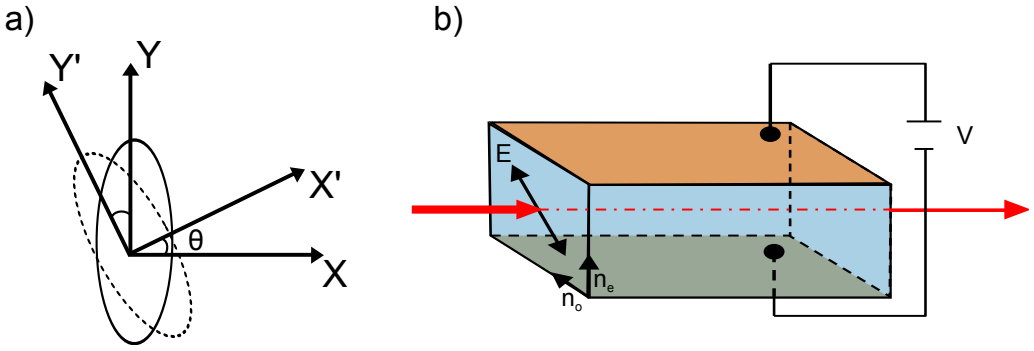

FIGURE 2.6: **Pockels effect.** a)Induced rotation of the principal axis of the refractive index ellipsoid. b) A voltage is applied perpendicular to the propagation axis of the beam between the facets parallel to the propagation axis (transverse electro-optic effect). The applied voltage changes the effective refractive index and there introduces a phase shift rotating the polarization of the input beam.

where r_{ij} are the electro-optic coefficients of the crystal, x_i are the entries of the coordinate system of the crystal and E_i are the components of the electric field [23]. In the case of lithium noibate (LN) which is the material used in the experiments presented in this thesis the electro optic tensor is given by [24]:

$$\begin{bmatrix} 0 & -r_{22} & r_{13} \\ 0 & r_{22} & r_{13} \\ 0 & 0 & r_{33} \\ 0 & r_{42} & 0 \\ r_{42} & 0 & 0 \\ -r_{22} & 0 & 0 \end{bmatrix}. \tag{2.37}$$

When a transverse voltage is applied to the crystal along $x_2 = y$, with $x_1 = x$, and $x_3 = z$ Eq. 2.36 reduces to [25]:

$$\begin{aligned} 1 = \left(\frac{1}{n_o^2} - r_{22}E_y\right) x'^2 + \left[\left(\frac{1}{n_o^2} + r_{22}E_y\right)\cos^2\theta + \frac{\sin^2\theta}{n_e^2} + r_{42}E_y \sin 2\theta\right] y'^2 \\ + \left[\left(\frac{1}{n_o^2} + r_{22}E_y\right)\sin^2\theta + \frac{\cos^2\theta}{n_e^2} - r_{42}E_y \sin 2\theta\right] z'^2 \end{aligned} \tag{2.38}$$

If we assume that $\cos^2\theta \simeq 1$ and $\sin^2\theta \simeq \theta$ then we can express the new principal refractive indices as

$$\begin{aligned}
\frac{1}{n_{x'}^2} &= \frac{1}{n_o^2} - r_{22}E_y, \\
\frac{1}{n_{y'}^2} &= \frac{1}{n_o^2} + r_{42}E_y\theta + \frac{\theta^2}{n_o^2}, \\
\frac{1}{n_{z'}^2} &= \left(\frac{1}{n_o^2} + r_{22}E_y\right)\theta^2 - 2r_{42}E_y\theta + \frac{1}{n_e^2}.
\end{aligned} \tag{2.39}$$

Considering θ to be very small the new indices would correspond to the original ones where

$$\begin{aligned}
n_x^2 &= n_o^2(1 + \frac{1}{2}n_o^2 r_{22}E_y), \\
n_y^2 &= n_o^2(1 - \frac{1}{2}n_o^2 r_{22}E_y), \\
n_z^2 &= n_e^2.
\end{aligned} \tag{2.40}$$

In the absence of an electric field the beam only experiences n_o, this means that when there is no voltage applied the polarization of the input beam is unperturbed. When a voltage is applied the x and y components of the beam would experience a phase difference:

$$\Delta\phi = \frac{2\pi L}{\lambda_0}(n_x - n_y) = \frac{4\pi L n_o^3 r_{22} V}{\lambda d}, \tag{2.41}$$

where d is the distance between the electrodes, L is the length of the crystal and λ_0 is the wavelength of the beam in vacuum. Form this last equation we can calculate the voltage required to induce a π phase shift:

$$V_\pi = \frac{\lambda_0 d}{4Ln_o^3 r_{22}} \tag{2.42}$$

2.4.2 Spatial light modulation using liquid crystals

In chapter 6 we perform an experiment where we shape the phase front of an optical beam to improve the coupling efficiency of a down-conversion source using a spatial light modulator (SLM). Here we will briefly describe how an SLM operates.

Spatial light modulators are miniaturized displays consisting of μm-sized pixels. Each pixel is filled with rod shaped liquid crystals (LC), which are long chains of molecules that exhibit liquid-like properties but also have long range ordering in their orientation, as solids do. These crystals are birefringent so that by controlling the orientation of the crystals it is possible to introduce phase retardation onto an optical wave. In an SLM the crystals are sandwiched between to glass substrates. On the surface of the glass, there are electrodes and orientation grooves that force the crystal rods to be aligned along them. The two glass substrates are rotated perpendicular to each other resulting in a twisted orientation of the LC molecules. When a voltage is applied across the electrodes the crystals align along the direction of the field. Due to the birefringence of the crystals, when a beam traverses through them it will acquire a phase depending on the orientation of the crystals (this in principle would also introduce a polarization rotation but the device is engineered such that the polarization would be unaffected for a specific input polarization). Then, when a beam is spread across multiple pixels we can then modulate its phase-front.

2.5 Optical detectors

For the purpose of optical quantum technologies an ideal single-photon detector would be one for which the detection efficiency is 100%, it has a fast response time (so that it is possible to determine with high precision the time of arrival of a photon in order to perform coincidence based measurements), the rate of dark-counts is zero, the dead time after a photon-detection event is zero, and the timing jitter is also zero. In addition,

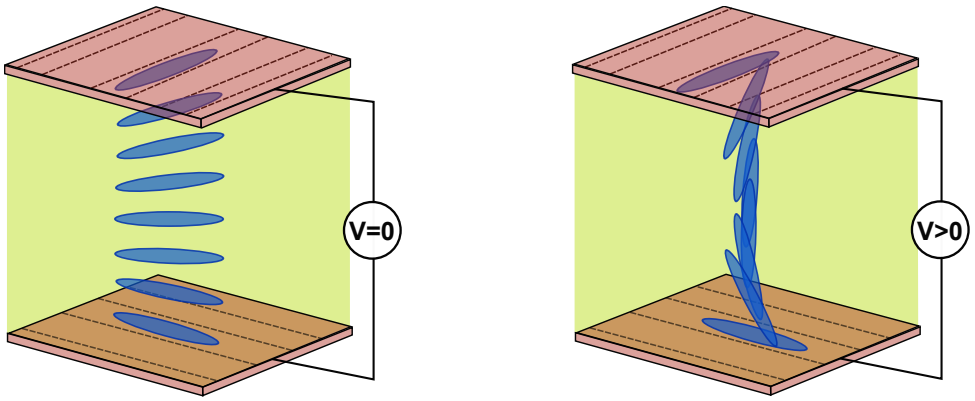

FIGURE 2.7: **Liquid crystal in SLM.**. On the left hand side, when no voltage is applied the crystal are oriented in a helix-like structure. When we apply a voltage the the crystals reorient themselves having their longer axis parallel to the electric field between the electrodes. In this case the beam would experience a different optical depth and hence a different phase shift when a we apply a voltage.

an ideal single-photon detector would have the ability to resolve the number of photons in an incident pulse [17]. There are many types of detectors which satisfy some of the aforementioned requirements, for the specific tasks that we investigate throughout this thesis we are mainly interested in detectors which perform with high single photon detection efficiency. Transition-edge sensors (TES) can achieve the highest reported efficiencies with 98% [26]. Superconducting-nanowire single-photon detectors (SNSPD) have the second highest reported efficiencies with 93% [27]. However both TES and SNSPDs require cryogenic temperatures to operate which makes them expensive and unpractical. Charged-couple-devices are a high-efficiency alternative for measuring intensities with efficiencies above 90% and sensitive down to the single photon level [28]. However CCDs are unable to perform time resolved measurements since their response time is too slow ($\sim$1.4 μs). Avalanche-photodiodes are the most practical and most commonly used detectors in the field of quantum optics, they typically have efficiencies around 70% in the near infrared [17] and response times in the order of tens of picoseconds [29]. In the experiments presented in this thesis we performed measurements using APDs and CCDs. For this reason we discuss their performance in the following subsections.

2.5.1 Avalanche-photodiode

An avalanche-photodiode (APD) is an optical detector designed to operate in strong reverse bias. In this device incident photons are absorbed creating electron-hole pairs which are subsequently cascaded amplifying the photocurrent by a significant factor. This means that when operated slightly above the breakdown threshold voltage, APDs can be used for single photon counting where a single electron-hole pair can trigger a strong avalanche [30].

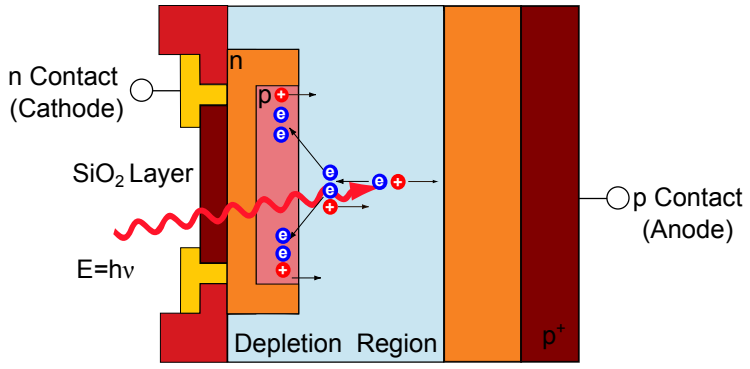

FIGURE 2.8: **Avalanche-photo-diode.** An APD contains a pn junction consisting of a positively doped region, p, and a negatively doped region, n, having an area of neutral charge between them called the depletion region. Photons entering the diode first pass through the silicon dioxide layer and then through the n and p layers before entering the depletion region where they generate electrons-hole pairs that are then cascaded in the p region. Adapted from [31].

APDs are commonly used for coincidence based measurements due to their fast response time which is in the order of tens of picoseconds. The response time of an APD is mainly limited by the transit time of the charge carriers within the depletion region. Therefore there is a trade-off between response time and the quantum efficiency (a bigger depletion region has higher efficiency but a slower response time and vice versa). Moreover the quantum efficiency is also related to the amount of noise that can be tolerated by the detector. Noise occurs when electron hole pairs are spontaneously generated due to the revers bias voltage (alson known as dark-counts). While photodiodes have been reported with almost unit efficiency [32], APDs have to trade-off efficiency for noise reduction in order to be able to readout the photo-current generated by a single photon. In the

experiments reported throughout this thesis we used APDs manufactured by Excellitas which have a dark-coutn rate of ∼600 Hz and a spectral efficiency curve shown in 2.9:

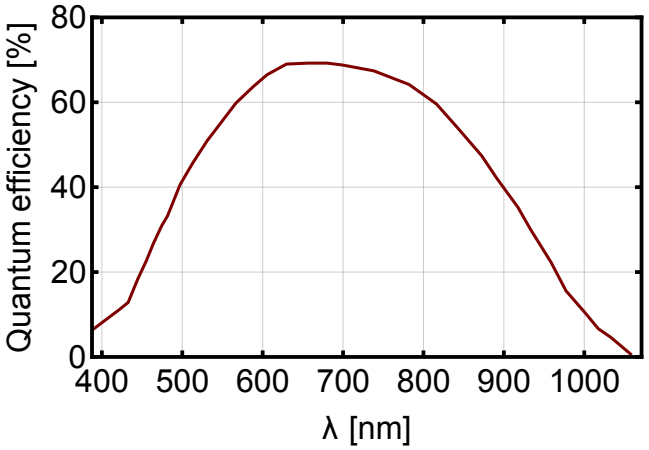

FIGURE 2.9: **Avalanche-photo-diode efficiency.** Typical photon detection efficiency as a function of wavelength for Excelitas SPCM APD [33]. The quantum efficiency of a detector is defined as the ratio of the number of successfully amplified electron-hole pairs to the number of incident photons.

APDs are unable to perform photon-number resolving measurements since one or more photons can trigger the same avalanche pulse, spatial or temporal multiplexing have been proposed as a way to perform pseudo-number resolving measurements [34–36].

2.5.2 Charge-coupled device

A high sensitivity alternative to superconducting detectors that can provide a quantum efficiency of up to 95% [37] at lower cost is a charged-coupled device. A charge-coupled device (CCD) is a light-sensitive integrated circuit composed of a matrix of metal oxide semiconductor (MOS) capacitors. This type of detector is useful when it is desired to obtain spatial information at low illumination levels as it is in the case of microscopy [38], Raman spectroscopy [39] or Astronomy [40]. Each MOS, also known as pixel, operates as a photodiode and a storage device able to trap and hold photon-induced charge carriers under the right electrical bias conditions. In order to determine the photon flux arriving at each pixel it is necessary to measure the stored charges which is done at a read out node where the signal is amplified. In order to transport charges, voltages are applied to each

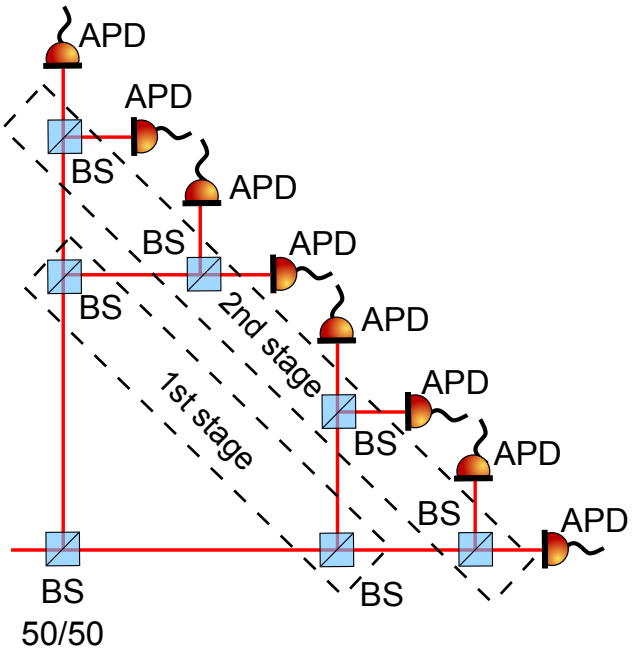

FIGURE 2.10: **Multiplexed detection scheme.** APDS are not able to discriminate between one or more incident photons. Multiplexing is way around this, by dividing the input beam via an arrangement of beamsplitters and distributing the incident light into an array of detectors we can assume that the probability of having more than one photon in each detector is very small and therefore determine the input number of photons. Adapted from [36]

pixel's controlling the movement of charges from one pixel to the next, or from one row of pixels to the next until transferred to the read out node as seen in Fig. 2.11. This process is slow and prevents the camera from obtaining precise time of arrival information of the incoming photons, making CCDs incompatible with coincidence based measurements.

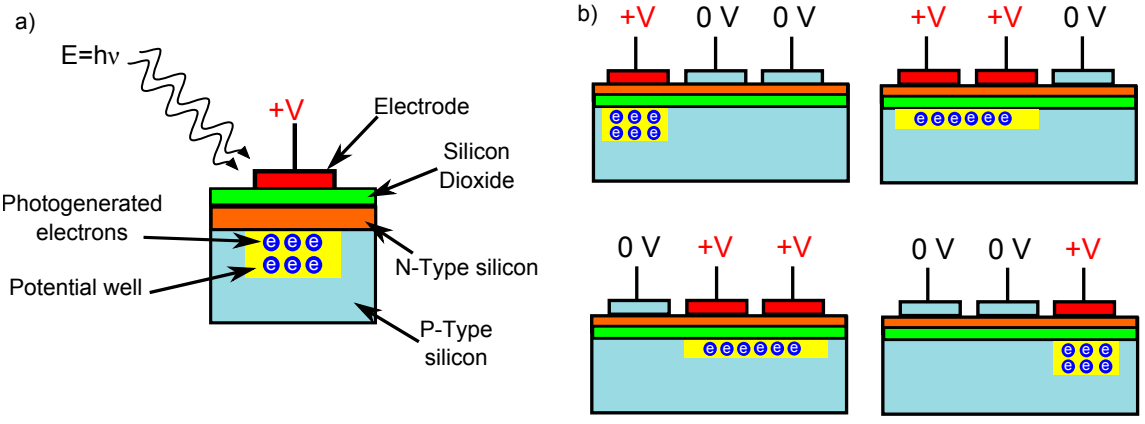

FIGURE 2.11: **Charge-coupled device.** a)The basic MOS structure. b) Progression of charge transfer with applied voltage. Adapted from[41]

The process of transferring charge introduces noise since single electrons can be generated during charge drift. Most of the noise in A CCD comes from readout amplification and thermal generation of free carriers which occurs when silicon atoms liberate electrons due kinetic vibrations [42]. Cooling the CCD reduces the accumulation of thermally released charge. Cooling the CCD also provides the additional advantage of improving the charge transfer efficiency. Other ways of increasing the efficiency of the camera are by introducing anti-reflection coatings, increasing the depletion region and by back illumination (where the sensor is back-thinned and the light is delivered through the back making it easier for the incident photons to reach and be absorbed in the active layer of the sensor [43])

In the experiments discussed in Chapter A and Chapter 4 we used an iDus 420 Bx-DD camera manufactured by Andor, a camera commonly used for low intensity spectroscopy. This camera has a specified readout noise as low as 4 electrons and an overall noise factor of 1.41 so that the signal to noise ratio of an input signal would be given by [44]:

$$\mathrm{SNR} = \frac{\frac{\mathrm{QE}}{100} \times N}{\left(\sqrt{\frac{\mathrm{QE}}{100} \times N}\right) \times 1.41}, \tag{2.43}$$

where N is the number of photons in the signal and QE is the quantum efficiency of the camera. The spectral sensitivity of the camera is shown in Fig. 2.12 having a peak efficiency of 90%.

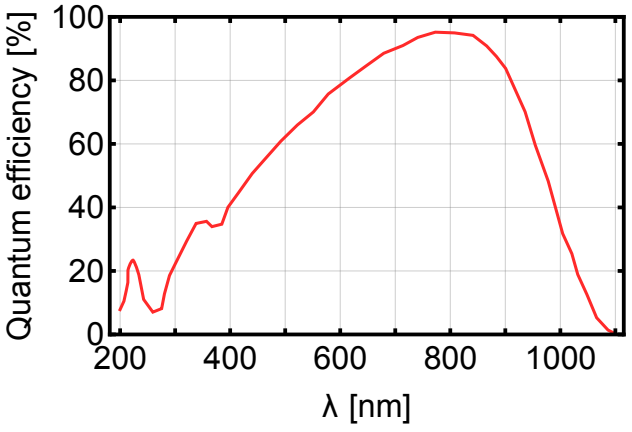

FIGURE 2.12: **Andor CCD efficiency.** Typical quoted quantum efficiency as a function of wavelength for Andor iDus 416 at -95° C [45].

Chapter 3

Sub-shot-noise transmission measurement using optically gated single photons

This chapter is based on the manuscript: *Sub-shot-noise transmission measurement enabled by active feed-forward of heralded single photons* by J. Sabines-Chesterking, R. Whittaker, S. K. Joshi, P. M. Birchall, P. A. Moreau, A. McMillan, H. V. Cable, J. L. O'Brien, J.G. Rarity, and J. C. F. Matthews, Phys. Rev. Applied 8, 014016 (2017) [46].

Statement of Work: Jonathan Matthews, John Rarity and I conceived and designed the experiment. I conceived the switch configuration and its assembly. Siddarth Joshi and Rebecca Whittaker built the source which I then aligned and optimized. I carried out the experiment. I performed the data analysis with consultation from Hugo Cable, Jonathan Matthews, Patrick Birchall and Paul-Antoine Moreau. This work was performed under the supervision Jonathan C. F. Matthews.

3.1 Introduction

Quantum mechanics quantifies the highest precision that is achievable in each type of optical measurement [47–49]. Single photon probes measured with single photon detectors are in principle optimal for gaining the most precision per-unit intensity when measuring optical transmission [10]. Entangled multiple-photon states can be engineered to achieve quantum enhanced precision in interferometry [49] and parameter estimation. However, in practice, optical loss and low component efficiencies prevent an advantage from being achieved using single photon detectors [50]. One approach is to use post-selection to ignore negative measurement outcomes that arise due to loss, while only recording positive results — this has proven to be highly successful for observing underlying physics in proof-of-principle experiments whilst testing quantum technology [51]. But for quantum metrology, post-selection used on its own leads to more photons being exposed to a measured sample than are used for data analysis, and therefore generally leads to worse overall performance than using classical strategies [52]. Another way to reduce the impact of lower component efficiency is to incorporate fast optical switching and an optical delay with schemes that are based on heralded generation of quantum sates [53]. This then enables use of a quantum state conditioned on the successful detection of a correlated signal — this is referred to as feed-forward and can be used to engineer quantum states that have increasing complexity and utility for quantum metrology [54, 55].

Feed-forward is key for demonstrations of optical quantum computing [56], it has been used in experiments that increase the generation rate [57–61] and signal-to-noise ratio [62] of heralded single photons, it has been used to calibrate single photon detectors [63] and it has also been applied to gather evidence of single photon sensitivity in animal vision [64]. Jakeman and Rarity proposed in Ref. [53] using feed-forward with correlated photon pairs to enable sub shot noise optical transmission measurements when component efficiency is otherwise not sufficient to permit a quantum advantage in passive direct detection [28, 65, 66]. But despite becoming identified as key to more general multi-photon entangled quantum state engineering for quantum metrology [54, 55], feed-forward has

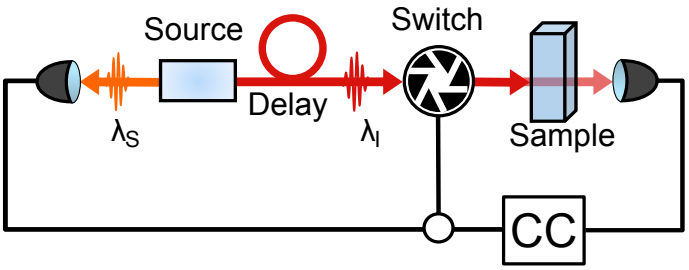

FIGURE 3.1: **Photon pair feed-forward transmission measurement.** Photon pairs of signal (λ_S) and idler (λ_I) photons are simultaneously emitted into two channels. Once a signal photon is detected, it opens a switch in the idler photon's channel to allow probing of a sample with the idler photon. The transmission estimate is obtained from the ratio of the number of coincidence detection (CC) and signal photon detection events.

not been implemented for quantum enhanced parameter estimation. Here we implement the proposal featured in Ref. [53] (Fig. 3.1) to realise sub shot noise measurement of transmissivity, using single photon detectors that are too low in efficiency to enable sub shot noise performance in a passive measurement.

3.2 Theory

The transmissivity η of a sample is in general estimated by measuring the reduction of light intensity from a known mean input value $\bar{N}_{\text{in}}$, to a reduced mean value $\bar{N}_{\text{out}}$ according to $\eta = \bar{N}_{\text{in}}/\bar{N}_{\text{out}}$. The precision with which η can be measured is dependent on the type of light used to probe the channel. When estimating η with an ideal coherent state probe $|\alpha\rangle$, the precision will be given by $(1/\Delta^2\eta)_\alpha = \nu\bar{N}_{\text{in}}/\eta$, where $\bar{N}_{\text{in}}$ is the average number of probe photons and ν is the number of repetitions of the measurement. This is the shot-noise limit and it is the upper-bound on the precision achievable with classical measurements [49]. Higher precision can therefore be achieved by increasing the input intensity and the number of repetitions. For a fixed intensity and fixed number of repetitions ν, non-classical states of light can provide an enhancement in precision over coherent state probes. The photon number probability distribution of a Fock state of $\bar{N}_{\text{in}} = N_{\text{in}}$ photons after passing through a lossy channel follows the Binomial distribution $P(N_{\text{out}}, N_{\text{in}}, \eta) = \binom{N_{\text{in}}}{N_{\text{out}}}\eta^{N_{\text{out}}}(1-\eta)^{N_{\text{in}}-N_{\text{out}}}$. So for fixed $\bar{N}_{\text{in}}$ and ν, the Fock state probe

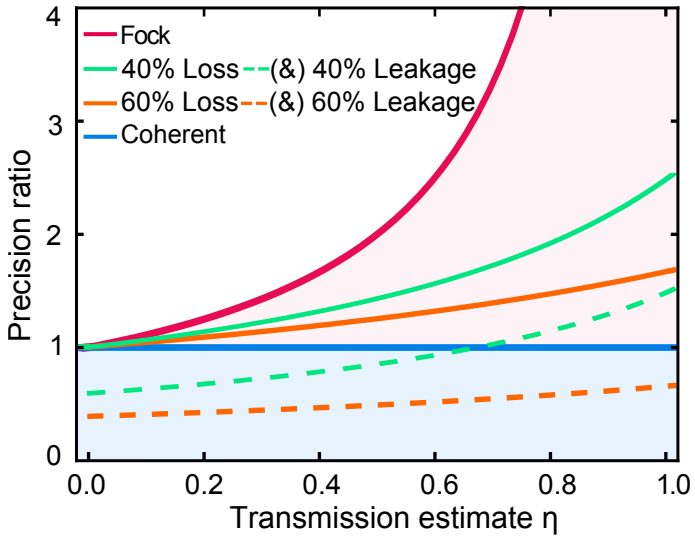

FIGURE 3.2: **Theoretical performance of the photon pair feed-forward transmission measurement.** Precision achievable relative to coherent states is plotted as a function of sample transmission η for an average input intensity of $\bar{N} = 1$ photons. The pink curve represents the ideal case of a heralded Fock state with no setup loss ($\eta_{\text{det}}.\eta_{\text{source}} = 1$), aside from the sample's transmission, and no switch leakage ($\eta_S = 1$). Illustrating the effect of experimental imperfections, the green and orange solid curves correspond to mixed states with setup losses $\eta_{\text{det}}.\eta_{\text{source}} = 0.4$ and $\eta_{\text{det}}.\eta_{\text{source}} = 0.6$ and with $\eta_S = 1$. The green and orange dashed curves represent respectively performance with $\eta_{\text{det}}.\eta_{\text{source}} = 0.4$ and leakage $1 - \eta_S = 0.4$, and $\eta_{\text{det}}.\eta_{\text{source}} = 0.6$ and $1 - \eta_S = 0.6$. The blue curve represents the shot noise limit. The light pink region reflects the area where there is a quantum advantage.

achieves a higher precision than the coherent state [10]:

$$(1/\Delta^2\eta)_F = \nu\bar{N}_{\text{in}}/\eta(1-\eta) > (1/\Delta^2\eta)_\alpha. \tag{3.1}$$

The performance of Fock states can be accessed by using correlated photon pairs generated from a spontaneous parametric down conversion process (SPDC). Signal photons of each correlated pair are sent directly for detection to herald the presence of the corresponding idler photon which is used to probe a sample. The transmissivity of the photons through the sample can then be estimated from the Klyshko (heralding) efficiency [67] of the idler channel η_I, which is the ratio of the number of photons detected coincidentally across the two channels N_C and the total number of detected herald (signal) photons N_S: $\eta_I = \bar{N}_C/\bar{N}_S$.

To obtain a quantum advantage using the Klyshko efficiency as the transmission estimator it is required to have a strong correlation between the number of signal and idler photons such that the difference between the coincidence and the signal count is due only to the absorption of the sample [28, 65, 66]. This is generally not the case when there is loss in either the signal or the idler channel, so when system performance prohibits having a high correlation, one can selectively analyze subsets of recorded data in post-selection to observe sub-shot noise behaviour [68]. However, in practice, a sample measured with post-selected events will be over-exposed, with photons that are unaccounted for due to lost counterpart heralding photons. This results in a strategy that performs worse than using a coherent state when analysis is normalized to per input probe photon. By introducing an optical switch into the setup, as sketched in Fig. 3.1, that only allows photons incident on a sample when a signal photon has been successfully detected, we increase the level of correlation and suppress the detrimental effect of loss in the signal channel. This changes the efficiency parameter $\eta_S = N_C/N_I$ from being the transmissivity of the signal channel into a parameter that describes the percentage of the idler photons detected after the switch that were correlated to detected signal photons. The parameter $1 - \eta_S$ therefore describes the leakage of unheralded idler photons through the switch. However, there are still three main mechanisms that can degrade the performance of the photon pair strategy using a switch. The first is loss of the idler photon in the photon source (including feed-forward optics) $1 - \eta_{\text{source}}$ and at the detector $1 - \eta_{\text{det}}$, which together with sample transmission η redefines the Klyshko efficiency $\eta_I = \eta_{\text{source}}.\eta.\eta_{\text{det}}$. For a single photon Fock state, $\rho = |1\rangle\langle 1|$, η_I modifies the state according to

$$\rho \to \rho' = (1 - \eta_I)|0\rangle\langle 0| + \eta_I|1\rangle\langle 1|, \tag{3.2}$$

which still follows a (sub-Poissonian) Binomial distribution and therefore still outperforms coherent states per input photon. But as loss increases $\eta_{\text{source}}.\eta_{\text{det}} \to 0$, the measured photon number distribution tends towards Poissonian. The second degradation mechanism is imperfect optical switching that allows unheralded photons to leak through the sample,

this is quantified by $1 - \eta_S$. The third mechanism is dark counts in the signal detector that can herald false idler photons into the idler channel — this effect becomes negligible when dark count rates are low compared to signal photon detection rates.

We plot examples of the effect of loss and leakage in Fig. 3.2, in terms of the ratio, Γ, between the precision achievable using a Fock state that has either been degraded by loss or incorrectly heralded with switch leakage, denoted $1/(\Delta^2\eta)_{F'} = \eta_S/\eta(1 - \eta\eta_I)$, and the precision achievable with a coherent state probe $1/(\Delta^2\eta)_\alpha = 1/\eta$ with the same detector efficiency. This ratio is a figure of merit that determines when a quantum advantage is obtained—that is when $\Gamma = \eta_S/(1 - \eta.\eta_I) > 1$. Note that this expression leads to the condition found in Ref. [53] where it was shown that for obtaining a quantum advantage over using a coherent state it is necessary that

$$\eta_I + \eta_S > 1. \tag{3.3}$$

3.3 Experimental setup

The experimental setup we used to implement feed-forward transmission measurement is shown in Fig. 3.5. Photon pairs were generated via collinear type II SPDC using a periodically-poled potassium titanyl phosphate crystal (PPKTP), pumped with a continuous wave (CW) laser diode ($\lambda_p = 403.9$ nm) and spectrally tuned by controlling its temperature. The spectral range of the source is shown in Fig. 3.3.

The wavelengths of the signal and idler photons usded in this experiment were $\lambda_s = 792$ nm and $\lambda_i = 824$ nm, each with a spectral width of ± 0.4 nm. After down conversion the pump was removed using a 715 nm long-pass filter (LPF) and a 50 nm wide bandpass filter (BPF) centered at 808 nm. Photon pairs were split deterministically using a polarization beamsplitter (PBS), sending the idler photon through the delay line while the correlated signal photon was collected with a single mode fibre and detected using an avalanche photodiode (APD).

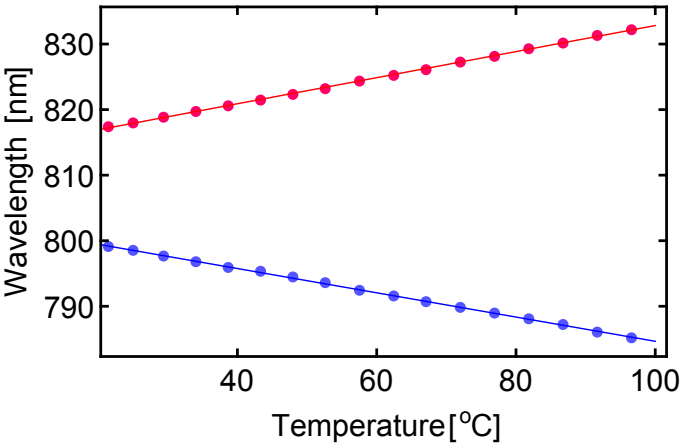

FIGURE 3.3: **Spectral range of the source.** The plot shows the spectral response of the down converted photons as a function of the crystal's temperature. This plot was obtained using a Shamrok single photon spectrometer. The signal photons (horizontally polarized) are shown in red and the idler photons (vertically polarized) in blue.

The detected signal photon triggered an optical switch implemented with a Pockels cell modulator composed of two lithium niobate crystals that rotated the polarization of an incoming photon by 90° when inactive and preserved the photon's polarization when activated. The halfwave voltage of the device at the wavelength of interest is 200 V. The switching rise time was 500 ns, this value is limited by the slew rate of the voltage amplifier that drives the Pockels cell.

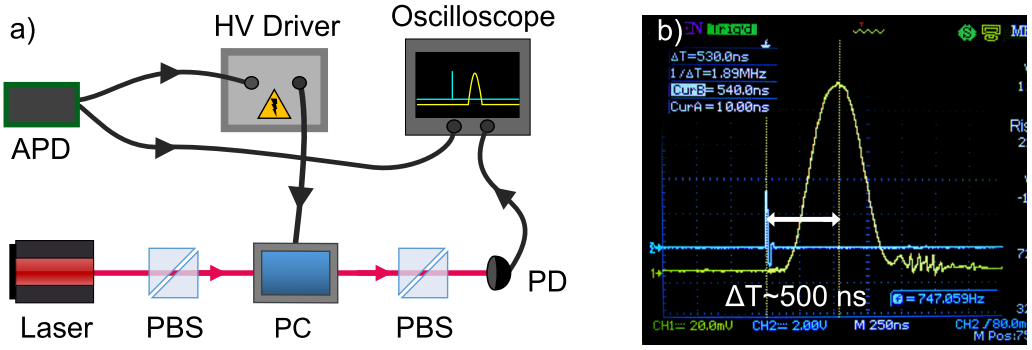

FIGURE 3.4: **Switch characterization.** The setup shown in a) was built to determine the switching rise time. Dark counts from a free running APD triggered the Pockels cell allowing a diode laser to be detected using fast photo-diode (PD). The signal from the APD and the photo diode were both sent to an oscilloscope to determine the delay between both signals. In b) we show the optical response of the Pockels cell. We obtained a rise time of 500 ns and a switching window of ~ 0.75 μs. The parameters shown in b) for the oscilloscope screen are of no relevance and should be ignored.

The extinction ratio achieved with this device is > 15 dB although it is ultimately limited by the polarization optics used at the output of the Pockels cell. This value was obtained using a strong coherent beam and would differ from the value obtained with single photons due to the long swithcing window time that allows unheralded photons to leak through the switch.

To compensate for any polarization rotations in the delay fibre, the Pockels cell was set inside a Sagnac loop, similar to the one reported in [69], this enabled bidirectional operation which makes switching independent of the input polarization. This strategy was chosen to avoid higher loss associated to polarization maintaining fibre and the need for active polarization stabilization. After switching, the idler photon was incident upon a variable transmission element comprised of a half waveplate (HWP) and a PBS, to mimic a variable transmission sample. Since the polarization of the idler photon was mixed after the optical fibre delay, both the horizontal and vertical polarization components of the idler photon needed to experience the same value of η—we achieved this by using a calcite beam displacer (BD) and a half waveplate to convert the two polarization components into two path modes with the same polarization. The loss introduced by these two components was 1.4% and was included in the overall system loss. Both modes then pass through the transmission element and are subsequently focused together onto a free-space APD for detection. Before any measurements of transmission, we first characterized the performance of the setup. The efficiencies of the source without the switch were $\eta_S = 41\%$ and $\eta_I = 44\%$ for the signal and idler channels respectively, corrected for dark counts but including η_{source} and $\eta_{\text{det}} \sim 65\%$. After introducing the switch, the efficiency of the idler photon's path (without a sample) was reduced to $\eta_{\text{source}}.\eta_{\text{det}} = 38\%$, this meant there was a loss of approximately 15% in the Sagnac loop and the delay line. The Klyshko efficiency of the signal channel increased to $\eta_S \sim 90\%$, which is less than the ideal $\eta_S = 100\%$ due to the ~ 0.75 μs width of the switching window that permits unheralded photons to be leaked through the switch. The pump power was adjusted to minimize this effect having a detection rate in the signal path of $\sim$36 k counts/s, $\sim$15.5 k counts/s in the idler channel and a coincidence rate of $\sim$14 k counts/s. In comparison, dark count rates in the

signal detector were low (∼0.6 k counts/s) and were accounted for when estimating η_I by subtracting their average number (characterized in the setup with signal and idler photon beams blocked) from the total number of detected counts recorded in our measurement. This means the contribution from dark counts which can lead to false heralding events is ∼1.5%

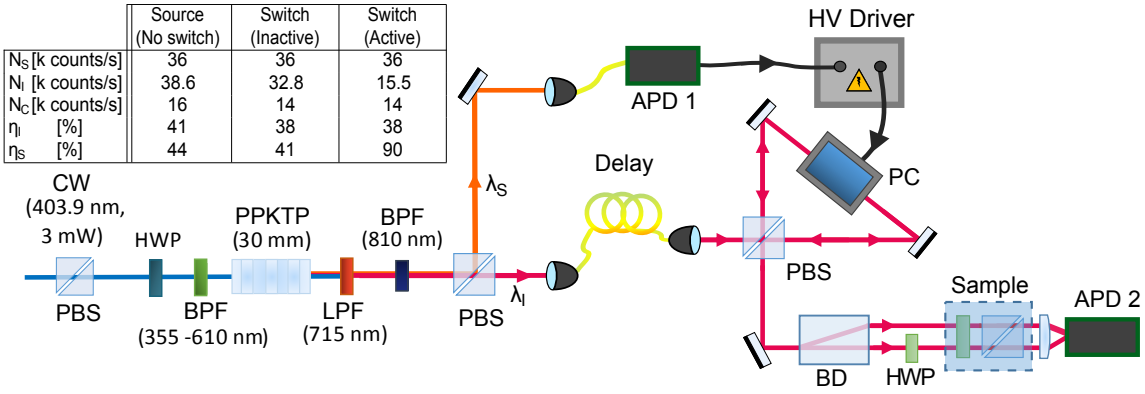

FIGURE 3.5: **Experimental setup.** Photon pairs are generated via type II collinear SPDC using a 30 mm PPKTP crystal pumped with a continuous wave (CW) 404 nm laser. While the idler photon goes through a delay line, the signal photon is detected and triggers an optical switch. The switch is a commercially available free-space Pockels cell type modulator consisting of two lithium niobate crystals inside a Sagnac loop. The source was mounted in a cage system to reduce vibrational noise. The inset table shows the approximate mean photon count rates (N_S, N_I, N_C) and the efficiencies ($\eta_I = N_C/N_S$ and $\eta_S = N_C/N_I$) for the experiment in the configurations of (i) just the photon source, (ii) addition of the switch optical components but left inactive and (iii) addition of the switch components when activated.

To verify that the source was heralding true single photons we measured the second order correlation function of the idler mode using the triple coincidence method reported in Ref. [70]. This was obtained by introducing a third detector in the reflected channel of the sample's PBS, setting the polarization of the signal photons to 45° and measuring the ratio between the triple coincidences and the product of the signal and idler coincidences of the reflected and transmitted channels.

$$g^{(2)}(0) = \frac{N_{SI_TI_R}}{N_{SI_T}N_{SI_R}} \tag{3.4}$$

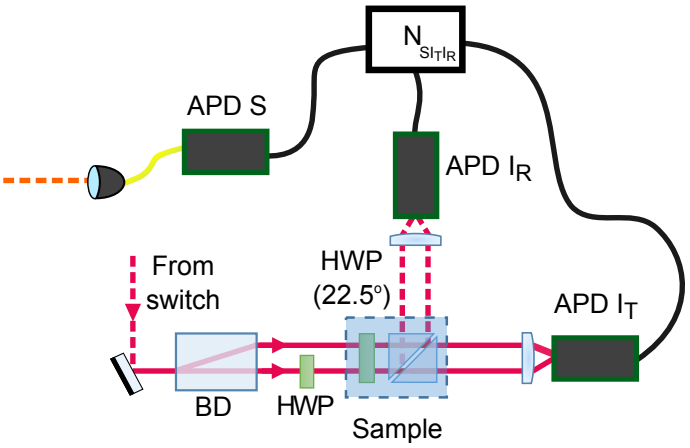

FIGURE 3.6: **Experimental arrangement for $g^{(2)}(0)$ measurement.**

A value of $g^{(2)}(0) = 0.031 \pm 0.002$ was obtained (it is worth noticing that a $g^{(2)}(0) = 0$ corresponds to perfect single photons and $g^{(2)}(0) = 1$ corresponds to Poisson distributed light). In comparison, solid state sources have reported values of $g^{(2)}(0) < 0.003$ [71], integrated sources based on four wave mixing $g^{(2)}(0) < 0.006$ [] and $g^{(2)}(0) < 0.01$ [] with SPDC sources, although it is important to notice that these values are dependent on the pump powers (lower pump powers reach lower values) and the dark counts of the specific detectors used in each experiment. We estimated the transmission of the sample η as the ratio between η_I measured at different sample transmission conditions and $\eta_{\text{source}}.\eta_{\text{det}}$, which we characterize by measuring η_I with sample transmission set to $\eta = 1$. The statistical precision of the transmission estimate per probe input to the sample is given by the inverse of

$$\Delta^2\eta = \text{Var}\left(\frac{\eta_{\text{I}}}{\eta_{\text{source}}}\right)\bar{N}_{\text{probe}}, \tag{3.5}$$

where $\bar{N}_{\text{probe}}$ is the average number of probe photons given by the number of detected idler photons (N_I) corrected for the percentage of idler photons that were successfully heralded (η_S), absorbed photons by the sample (η), average number of dark counts of the detector ($\bar{N}_D$) and detector efficiency (η_{det}):

$$\bar{N}_{\text{probe}} = \frac{\bar{N}_I}{\eta_{\text{det}}.\eta.\eta_S} - \bar{N}_D. \tag{3.6}$$

3.4 Results

In Fig. 3.7 we present the precision achievable with our feed-forward transmission measurement setup, with respect to the theoretical precision achievable with a coherent state scheme using the same detector efficiency [72]. We make this comparison by computing the ratio of precision of the two schemes, as for Fig. 3.2 and we observe a factor of improvement of up to 1.27±.08 for $\eta = 0.97$ and a quantum advantage is observable down to sample transmission of $\eta = 0.65$. When we turn off the optical switch, the performance of the setup is far below that of the coherent state strategy.

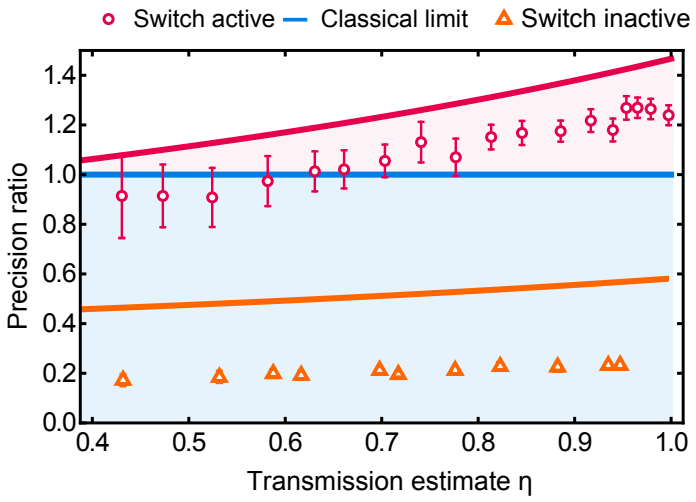

FIGURE 3.7: **Experimental Results.** The pink circles correspond to the estimated experimental advantage compared to a coherent state having the same detector efficiency. Each point corresponds to 3000 repetition of measurements taken with an integration time of 0.2 s and a coincidence window of 30 ns. The orange triangles correspond to the performance of the scheme when the switch is not active (error bars are too small to be seen). The pink solid line corresponds to the expected trend for mixed states with setup efficiency $\eta_{\text{source}}.\eta_{\text{det}} = 38\%$ and $1 - \eta_S = 10\%$ leakage. The orange line corresponds to a mixed state with the same setup efficiency but with $1 - \eta_S = 62\%$ leaked or unheralded photons. The discrepancy between the solid lines and the experimental points are attributed to various sources of noise including vibrational motion of the fiber couplers, temperature fluctuations of the crystal and electrical noise from detectors. Error bars were obtained by calculating the variance of binned sets of data points.

3.5 Conclusions

Using feed-forward for measurement is advantageous when it is desired to probe an object with a controlled number of photons [64, 73, 74]. Solid state sources of photons, such as quantum dots, could also be used for such purposes. They can operate with MHz emission rates [75], they can be used with high heralding efficiency [76] and they can emit higher energy photons [77] than those demonstrated in this letter — however, the higher specification solid state photon sources currently require additional resources, in particular cryogenic cooling and narrow-band filtering from photonic structure engineering, that can limit practicality and add cost to development. Practical application of using feed-forward with spontaneous sources for measurement will be aided by improvements in the brightness of the source [55] and the switching speed. Increasing the precision obtainable per unit intensity will come with improvements in the loss budget of the setup and increasing detector efficiency. State of the art SPDC sources using superconducting detectors have reported Klyshko efficiencies of 83% (Ref. [78]) — such an efficiency would already translate into a $\sim$ 5-fold advantage in precision in our setup. This could be illustrated in Fig. 3.8 where we have taken measurements in post-selection of the idler channel's Klyshko efficiency which reaches up to 90% showing the trend of an ideal Fock state which reaches an improvement factor in precision of up to ten-fold.

To conclude we most highlight that the wavelength tunability available in SPDC sources can enable sub shot noise measurement of spectral response [68]. Also that the polarization independent switch used in our experiment could also be useful as the feed-forward mechanism to engineer quantum states that are more complex and have more utility than single photons [54, 55].

3.6 Appendix

In this appendix we will describe two upgrades on the experimental setup. This upgrades were implemented once the experiment was finish and no data was acquired after they

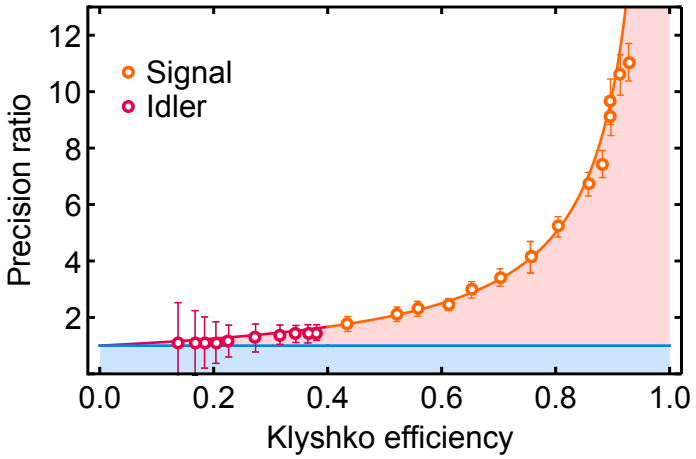

FIGURE 3.8: **Post-selected Klyshko efficiency.** We scan the signal's Klyshko efficiency by varying the bias voltage of the Pockels cell and hence the switching efficiency. In this way we can control the level of leakage through the switch.

were implemented.

One of the most challenging aspects of this experiment is the alignment of the electro optical modulator. Good contrast in switching can only be achieved with a very precise alignment of the beam with respect to the principal axis of the crystals in the Pockels cell. The alignment procedure is described in [79]. A card is placed a few centimeters away from the output of the modulator, registering the position where the beam strikes the card. A polarizer is placed between the modulator and the card. Then the input aperture is covered using a transparent and diffusive material for example a piece of frosted adhesive tape. This will project an isogyre pattern on the viewing card as the one shown in figure 3.9 a). To ensure good alignment it is necessary to adjust the modulator angle of incidence until the center of the geometric pattern is coincident with the mark previously made on the card indicating the beam location. By rotating the polarizer by 90° we obtain figure 3.9 b), to make fine adjustments the incidence angle could be adjusted until the contrast between the two isogyre patterns is maximum.

This procedure is very tedious and laborious specially using the Sagnac configuration of the optical switch which also requires a good overlap between the two input beams. A way to guarantee near optimal alignment is by 3D printing a mount for all the optical components. In this way only small adjustments have to be done on the mirrors and the

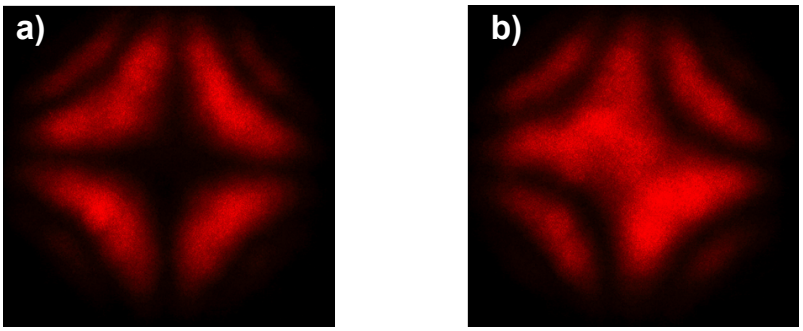

FIGURE 3.9: **Isogyre patterns.**The image in a) shows the isogyre pattern with the polarizer parallel to the input polarization, b) shows the isogyre pattern when polarizer is perpendicular to the input polarization.

polarizing beam splitter, the alignment with respect to the principal axis of the crystal is almost given. This simplifies the alignment significantly and makes the switch more robust and portable. The schematics for the model are shown if figure3.10.

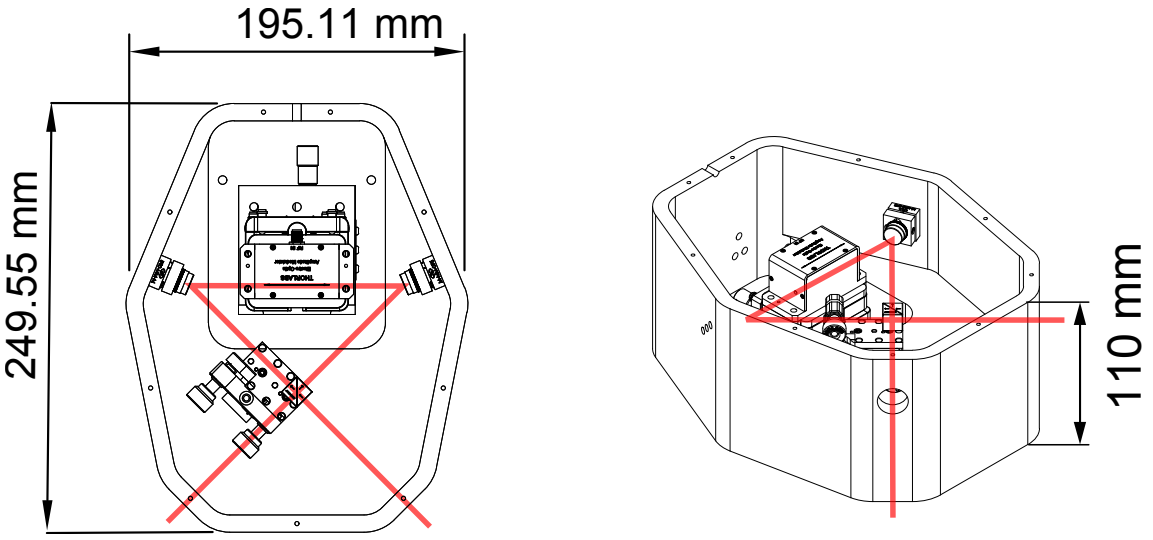

FIGURE 3.10: **3D printed Switch diagrams.**The figure shows the technical diagram of the 3D printed switch with all components mounted.

The efficiency of the switch is determined by multiple parameters, the extinction ratio of the PBS, the alignment of the crystals and the switching speed of the EOM. The speed of the EOM refers to two different aspects, the rise time of the switching window and it's width. These last two parameters are determined by the slew rate of the high voltage amplifier that drives the Pockels cell, this is how quickly can the driver deliver and withdraw voltage into the crystal. For the Pockels cell used in this experiment the

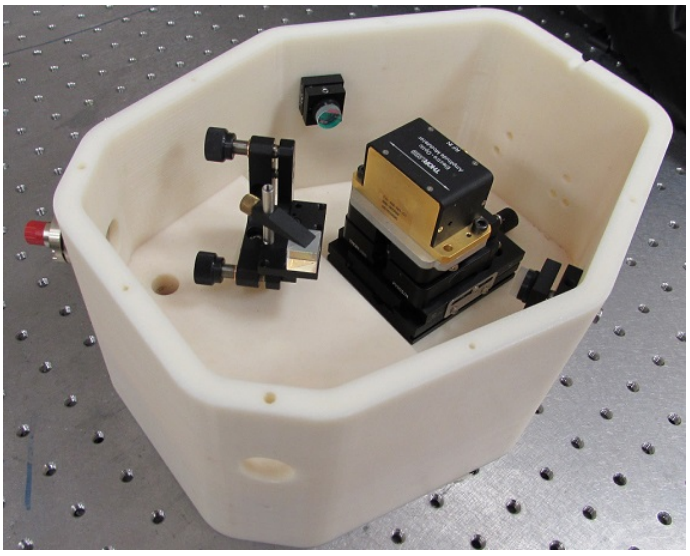

FIGURE 3.11: **3D printed Switch.**The figure showas the end result of the 3D printed switch.

half wave voltage is 200 V, delivering such a high voltage in the nanosecond regime is challenging and requires high performance electronics.

When we started to build the switch we first used the driver provided by the same supplier as the Pockels cell (Thorlabs). This driver was extremely slow and it would require a delay line of approximately 1 km for the signal photon. This amount of delay would translate into a loss of approximately 3 dB in the signal channel making it impossible to achieve a quantum advantage with the biphoton scheme. For the experiment we used a voltage amplifier with a higher slew rate, reducing the delay time to 500 ns allowing us to achieve a switching efficiency of 90%. This value is below the extinction ratio of the PBS (1000:1) due to the width of the switching window allowing unheralded photons to leak. This leakage limits the brightness of the source since higher rates of photons would reduce the switching performance. We improved this value using a driver with an even higher slew rate allowing us to achieve a rise time of 120 ns and a switching efficiency of 95%. The driver was characterized using the same delay as the one used during the experiment (100 m) but if the delay fibre was substituted with a 150 ns delay line the loss budget in the signal channel would reduce form 15% to 12% improving the overall quantum advantage of the scheme. The performance of all drivers are presented in table 3.1.

TABLE 3.1: **High Voltage amplifiers performance.** The switching efficiency is understood as the Klyshko efficiency of the signal channel as explained in chapter 3.

	ThorLabss	A.A. lab systems	Qioptiq
Rise time	5 μs	500 ns	300 ns
Switching window	8 μs	150 ns	120 ns
Slew rate	400 V/μs	1000 V/μs	1600 V/μs
Switching efficiency	44%	90%	95%

From the table we found that the performance of switch improves considerably with faster electronics. We expect that custom made electronics in combination with a longer crystal that would require a smaller half wave voltage would allow us to reach switching efficiencies closer to 100%.

Chapter 4

Twin beam sub-shot-noise raster-scanning microscope with a hybrid detection scheme

Statement of Work: I together with Jonathan Matthews, John Rarity, Paul-Antoine Moreau and Alex McMillan designed and conceived the experiment. I together with Alex McMillan carried out the experiment. Siddarth Joshi and Rebecca Whittaker built the source which I then aligned and optimized. The software for data acquisition was written by Paul-Antoine Moreau and Alex McMillan. Mateusz Piekarek and I performed the detector characterization. I performed the data analysis. This work was performed under the supervision John Rarity and Jonathan C. F. Matthews.

4.1 Introduction

Traditional imaging techniques relying on classical optics, particularly microscopy, have a long history of development and are now standard tools across a broad range of scientific

disciplines. For biomedical research in particular, high resolution images of structures such as cells continue to be invaluable. In recent years, there has been increasing awareness of the advantages of incorporating quantum states of light in imaging systems. Some well-known examples of beneficial quantum imaging effects include ghost imaging [80], super resolution [2], imaging without detection [81] and sub-shot-noise (SSN) spectroscopy and phase estimation [68, 82]. In particular sub-shot-noise imaging [28] is of interest when dealing with delicate photosensitive samples where increasing the probe intensity may improve the signal-to-noise ratio and imaging quality, but it could also damage the sample. In any case, the precision with which optical parameters of a sample, such as transmission, can be measured is limited by the stability of the light source used as the probe, and even the most stable classical source (an ideal laser) suffers from unavoidable shot-noise [47].

Twin beams from a spontaneous parametric sources can suppress noise beyond the shot-noise limit [65] improving the precision per photon exposure when used as a probe for transmission estimation. Sub-shot noise absorption imaging has been previously demonstrated in post selection [28]. Post-selection in the sense that loss due to inefficient detection has not been accounted so that the comparison of the results is to a coherent illumination scheme with non-unitary detection efficiency. More recently there has also been a demonstration of twin beam imaging applied to wide field microscopy [83]. Further work has led to an absolute demonstration of sub-shot-noise performance in absorption estimation using an optimized estimator as discussed in Appendix A and in Ref. [84]. This was then followed by a publication showing even higher performance using a higher efficiency source and CCD camera with 95% quantum efficiency [85]. The aforementioned strategies prefer use of high efficient CCD cameras over APDs to reduce detection-based loss which hinders the advantage in noise reduction. Here we construct a raster-scanning microscope where illumination is provided by a correlated twin-beam source but we incorporate feed-forward and the use of a hybrid detection scheme combining an APD and a CCD camera feed-forward allows us to reject uncorrelated photons and the CCD camera provides high detection efficiency.

4.2 Theory

Depending on the detection scheme, there are two approaches to estimate transmission using correlated twin beams. If the detector is able to obtain time of arrival information from the photons, a coincidence based measurement can be realized [53]. In this case the transmission of a sample, η_S, can be measured as the ratio of the Klyshko efficiency of the probe channel (η_P) with and without the sample $\eta_S = \eta_{P'}/\eta_P$. The Klyshko efficiency of the probe channel being defined as:

$$\eta_P = \frac{\langle N_C \rangle}{\langle N_R \rangle}, \tag{4.1}$$

where N_C is the number of coincidence counts between the reference and probe beam and N_R is the number of single counts of the reference beam. Experimentally we can compare the performance of a twin beam scheme for measuring transmission to that of a coherent state scheme by estimating the ratio, Γ, between the precision that can be attained with each. In an ideal scenario the estimator of transmission using a coherent state scheme will follow a Poissonian distribution and the estimator using a twin beam scheme, should ideally be a binomial [11]. Alternatively we can predict the value of Γ if the transmission of the sample and the Klyshko efficiency of both the probe and reference channel, η_R, are given. Following the derivation in [53], the expression to predict Γ is given by:

$$\Gamma = \frac{\eta_R}{1 - \eta_S \eta_P}. \tag{4.2}$$

This expressions tells us that whenever $\Gamma > 1$ we obtain SSN performance and for this to happen the sum of the probe and reference beam (or signal and idler) Klyshko efficiencies needs to be greater than one[1]

[1]This is not accounting for the sample transmission and without using the single photon count contributions.

$$1 < \eta_P + \eta_R. \tag{4.3}$$

When the detector is unable to obtain time of arrival information from the photons, which is the case for a CCD, an estimator could then be expressed as:

$$\eta_S = \gamma \frac{\langle N_{P'} \rangle}{\langle N_R \rangle}, \tag{4.4}$$

where γ is a pre-calibration factor defined as $\langle N_R \rangle / \langle N_P \rangle$. When using this approach, a way of quantifying the degree of correlation is by estimating the noise-reduction-factor [83] (NRF) σ, defined as:

$$\sigma = \frac{\Delta^2 (N_R - N_P)}{\langle N_R \rangle + \langle N_P \rangle}. \tag{4.5}$$

To obtain a quantum advantage in estimating transmission, the NRF should satisfy the following condition from [28], $\sigma < 0.5$ (true when using the estimator given in Ref. [28], for other estimators the condition may be $\sigma < 1$). From Eq.4.5, we can notice that when the beams are perfectly correlated ($N_P = N_R$) then $\sigma = 0$, so that the smaller the value of σ, the higher the correlation and the advantage that can be achieved using a twin beam scheme. The NRF can be related to the transmission efficiency of the twin beam channels or the Klyshko efficiencies by $\sigma = 1 - \eta$ (considering balanced losses $\eta = \eta_P = \eta_R$), from this expression we can appreciate that improving the transmission efficiency decreases the NRF and hence improves the advantage, so that reducing the optical losses is paramount for a twin beam scheme. High efficiency CCD cameras can considerably reduce detection-based loss and have been commonly used for demonstrations of sub-shot-noise performance [28, 83, 84].

Here we demonstrate a twin beam noise reduction scheme combining feed-forward and the use of a high efficiency CCD camera for detection. By implementing feed-forward, it

is in principle possible to virtually reduce the reference (heralding) beam channel-loss to zero, limitted by the efficiency of the switch itself [53]. This in turn increases the Klyshko efficiency of the reference beam closer to unity which facilitates satisfying the condition for SSN performance set in inequality 4.3. Here, instead of using a second APD for the probe (heralded) beam and detecting coincidences, we use a high efficiency CCD camera which reduces detection-based loss of the probe beam but measures only the total number of photons detected in a given interval and cannot resolve timing information. However since the switch forces the probe photons to be correlated to the reference beam we can still treat the detected photons by the camera as coincidences and use the Klyshko efficiency approach to estimate transmission. This is the first time to our knowledge that a hybrid system of detection has been implemented, having the ability to gate photons and detect them with high detection efficiency

Feed-forward unavoidably introduces loss to the probe channel. Therefore, to obtain a higher precision ratio there is a trade-off between increasing the Klyshko efficiency of the reference channel and decreasing the efficiency of the probe channel. In figure 4.1 we plot the precision ratio that can be obtained by implementing feed-forward to sources with different levels of Klyshko efficiency, assuming the loss on the probe beam due to the feed-forward optics is the same as in our setup (15%).

We can observe from figure 4.1 that one of the advantages of using feed-forward is that the crossover point to obtain SSN performance happens at lower transmissivities than without feed-forward. We can also observe that for Klyshko efficiencies below 70% feed-forward reaches a higher precision ratio than directly using twin beams.

4.3 Experimental Setup

The experimental setup used in this experiment is presented in figure 4.2. The sub-shot-noise light source and switch used here are the same as the ones reported in Chapter 3. Type II collinear SPDC is generated using a 30 mm periodically poled potassium titanyl

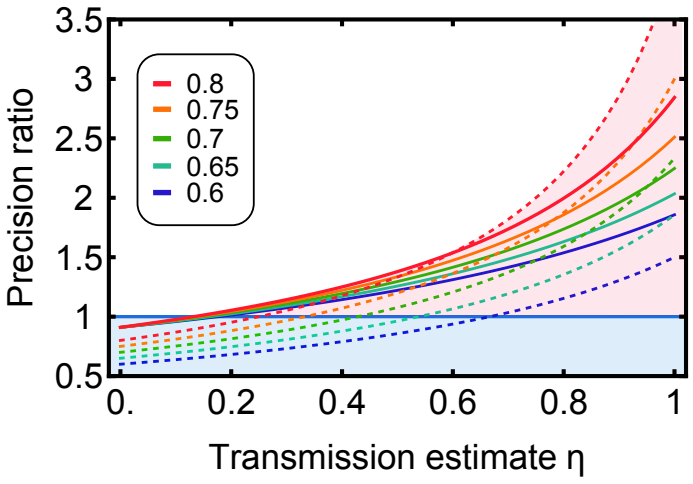

FIGURE 4.1: **Simulation of precision ratio using twin beams and feed-forward.** The plot shows the precision ratio compared to a coherent state (marked by the horizontal blue line at ratio of 1), of transmission estimation with twin beam strategies, under different efficiency conditions. The inset indicates different values of source Klyshko efficiencyiy. The Klyshko efficiencies are symmetric for direct twin beam exposure (dotted lines) and asymmetric for feed-forward (solid lines). For the asymmetric efficiencies a 90% efficient optical switch introducing 15% loss is considered in the model.

phosphate crystal (PPKTP) pumped with a continuous wave (CW) 404 nm laser. The wavelength of the down converted photons is tuned by controlling the temperature of the oven emitting photons at 798 nm (signal) and 818 nm (idler). Generated photon pairs are filtered using a long pass and a band pass filter and then deterministically separated using a polarizing beam splitter (PBS). After being separated, the photons are each coupled into two single mode fibers. The signal photon is then detected with an APD, heralding the presence of its companion and triggering an optical switch. The switch is a free-space Pockels cell type modulator consisting of two lithium niobate crystals inside a Sagnac loop. After switching, the idler photons are focused onto a sample and then recollimated using a pair of microscope objectives. Once the idler beam has traversed the sample and has been collimated it is then focused onto the sensor of a Andor iDus 416 CCD camera for detection. The sample is raster scanned in the plane perpendicular to the path of the beam. As the intensity of the light passing through the sample is measured, we buildup an image on a point by point basis.

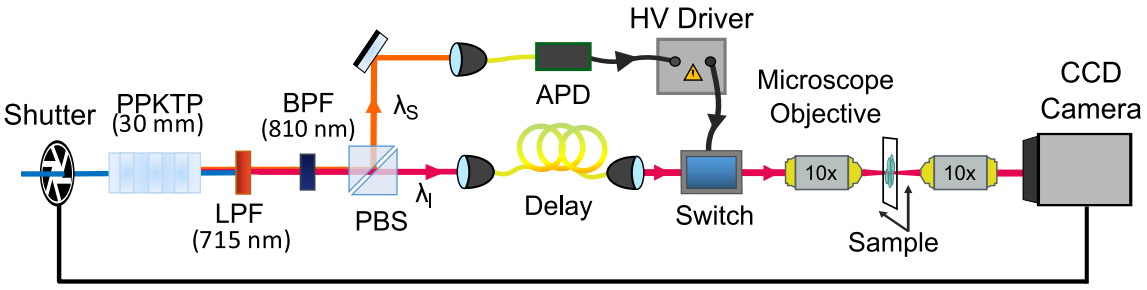

FIGURE 4.2: **Experimental setup.** Photon-pairs are generated and feed-forward is implemented using the same setup as in chapter 3. Heralded photons are focused onto a sample using a 10x microscope objective, then collimated using a second microscope objective with the same characteristics and finally refocused onto a CCD camera. The sample is raster scanned in two dimensions, reconstructing an image. A mechanical shutter is placed before the crystal and it is triggered by activation of the camera sensor, initializing the experiment and allowing the pump beam to impinge on the crystal. The shutter prevents undesired exposure on the sample during the camera's dead time. The acquisition time of the APD is synchronized to the CCD using a software interface that communicates with a time tagging electronics system that only records counts during the acquisition time of the camera.

The sample, shown in figure 4.3, is a 3 mm thick AR coated N-BK7 window where features have been engraved using reactive-ion etching, where we selectively thinned the anti-reflection coating of the window to create a low contrast transmission image. In other sections of the sample we instead used platinum deposition to create higher contrast images. The ion-etched figures have high transmittance (∼95%) and low contrast (∼2%) which make them ideal to show the practicality of the twin beam imaging scheme.

4.4 Experimental setup characterization

To start with, we first characterized the efficiency of the optical switch in terms of the leakage of unheralded photons. This was done by measuring the Klyshko efficiency of the reference beam (the signal channel in Fig4.2) using APDs in both the reference and probe beam. We obtained a value of $\eta_R = N_C/N_P = 90\%$, this value tells us how many probe photons have been successfully heralded, in other words what percentage of the photons detected on the camera can be treated as coincidences.

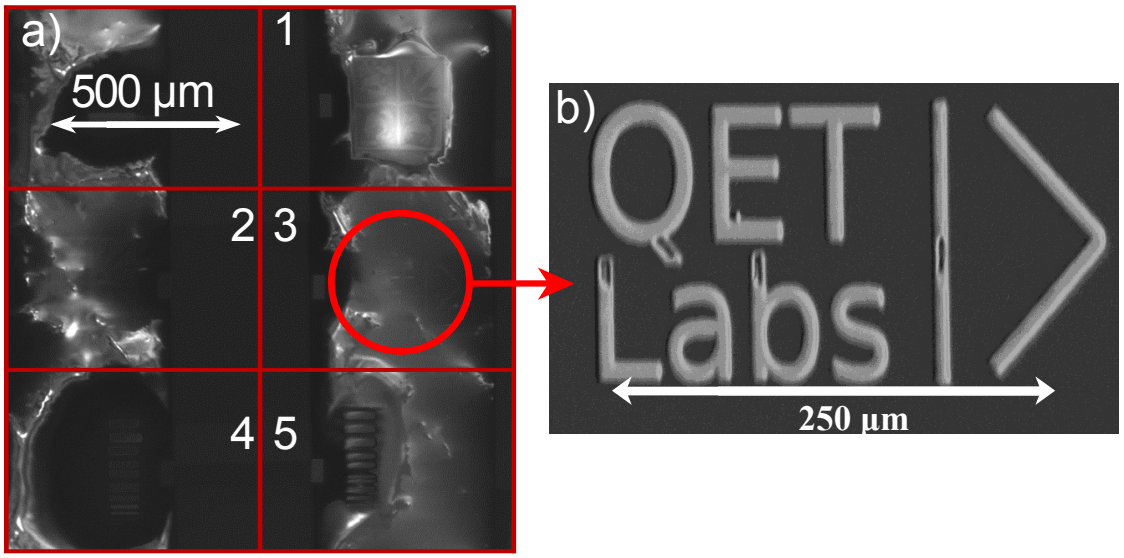

FIGURE 4.3: **Electron microscope image of the sample tested.**a) Section 1 and 2 are university of Bristol logos. Section 3 is a QET labs logo. Sections 4 and 5 are resolution targets consisting of periodically separated lines with different widths. Sections 1, 3 and 5 are ion-etched. Sections 2 and 4 are platinum depositions. b) Magnified image of section 3, ion-etched QET labs logo.

We then characterized the system's performance by using a variable neutral-density (ND) filter as a sample and estimated the transmittance for different values of attenuation, and evaluated the precision of our measurements compared them to the performance of an ideal coherent state scheme measured with a 100% efficient detector. The comparison is obtained by estimating the ratio between the known precision of an ideal coherent illumination scheme, $\Delta^2\eta_{\text{coh}}$, and the precision of the experimental results of our estimate, $\Delta^2\eta_{\text{exp}}$, normalized by the mean number of probe photons, $\langle N_{P_{\text{IN}}}\rangle$,

$$\Gamma = \frac{\Delta^2\eta_{\text{coh}}}{(\Delta^2\eta_{\text{exp}})\langle N_{P_{\text{IN}}}\rangle}, \tag{4.6}$$

where the number of probe photons is given by the mean number of detected probe photons, $\langle N_{P_{\text{Det}}}\rangle$, corrected by the efficiency of the camera, η_{Det}, the transmissivity of the optics after the sample, η_{opt}, and the transmissivity of the sample, η,

$$\langle N_{P_{\text{IN}}}\rangle = \frac{\langle N_{P_{\text{Det}}}\rangle}{\eta_{\text{Det}}\eta_{\text{opt}}\eta}. \tag{4.7}$$

The results of the system performance characterization are shown in figure 4.4.

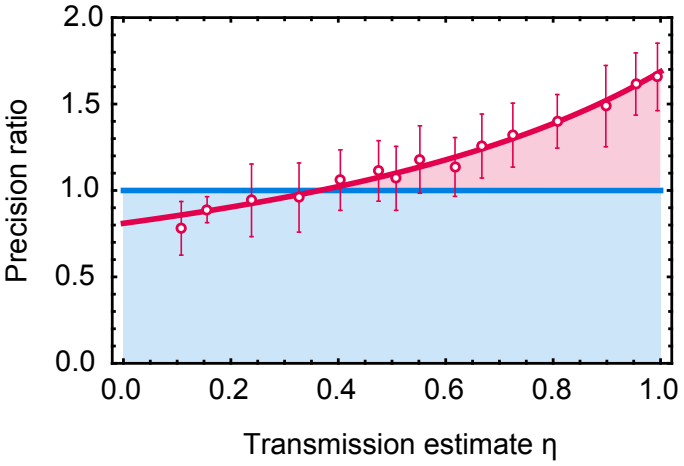

FIGURE 4.4: **System performance.** The plot shows the precision ratio of transmission estimation between our setup and an ideal coherent state measured with a 100% efficient detector, this represented by the horizontal blue line at ratio of 1 (this is the shot-noise limit). For each point we perform 13 series of 40 measurements, each with an exposure time of 0.5 seconds. The mean rate of signal photons detected was 40 x 10^{-3} per second.

The maximum precision ratio obtained with our setup was Γ =1.66 ±0.2. When compared to a classical scheme using the same detector efficiency (90%) the precision ratio increases to 1.88 ± 0.2. and 2.32 ±0.2 when compared to an ideal classical differential scheme. The system achieves sub-shot-noise performance for transmissivities higher than 0.4. This demonstrates that sub-shot noise transmission measurement is not confined to weakly absorbing materials.

After characterizing the noise reduction performance of our setup we then characterized the resolution of our imaging system. For this we used the resolution target in the sample shown in figure 4.5 a). The target consists of a series of pairs of lines with different widths ranging from 5 μm to 1 μm. As shown in figure 4.5 b), we were able to resolve features with a width of 3 μm.

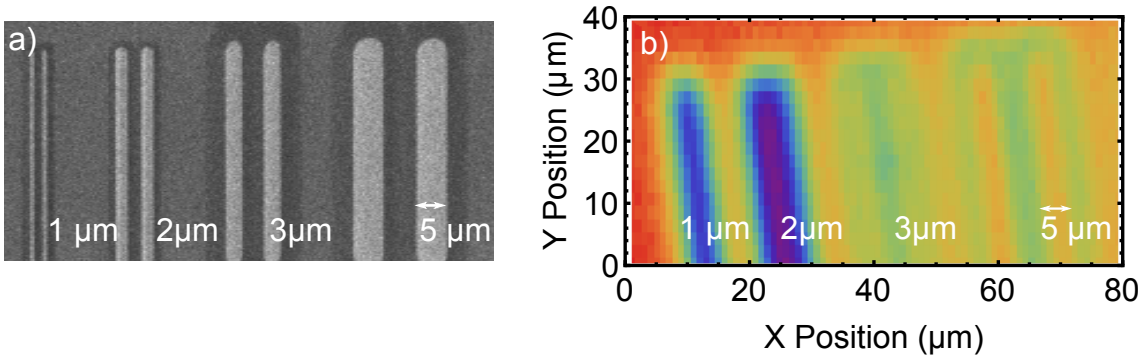

FIGURE 4.5: **Resolution of the setup.** a) Electron microscope image of the resolution target. b) Resolution target captured with twin beam imaging system.

4.5 Results

In order to demonstrate the advantage of noise reduction with our source we compare the results obtained with our imaging system to a direct and differential classical imaging schemes. For the differential measurements we used a laser attenuated to the same level of intensity as the down-converted photons. We then introduced a beam splitter after the switch and used the reflected beam as the reference beam for the differential measurement. This is illustrated in figure 4.6.

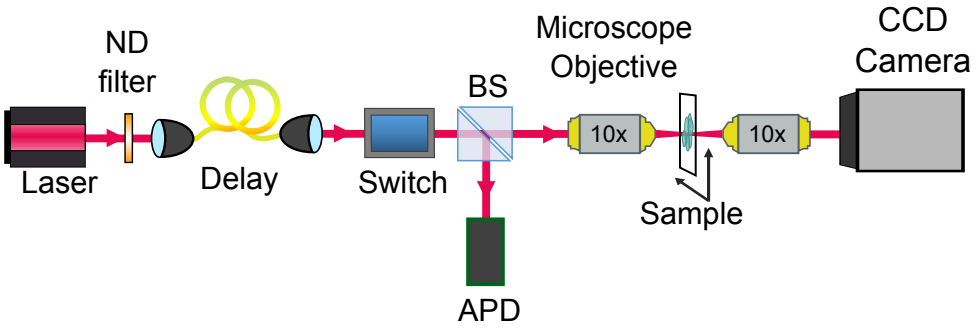

FIGURE 4.6: **Differential measurement setup.** We introduce a beam splitter after the switch and measure the refrence beam using an APD.

The images presented in figure 4.7 show qualitatively the advantage of our imaging system. We can clearly observe how the twin beam image presents features that are almost invisible with the other schemes. It is also apparent from the direct and differential illumination images, figure 4.7 b) and c), that drift in the brightness of the illumination source is degrading the quality of the images (this is observed as variations in the values of regions

where the transmissivity should remain constant) but the twin beam image is unaffected by this effect. Drift affects the accuracy of our measurements, it is of relevance for image processing where if it was desired to highlight features of an image by increasing the contrast (for example when pixels are turned into binary values), drift would prevent us from doing so[2]. This is exemplified in figure 4.8, where in order to highlight the features we have set different thresholds of transmission so that pixels obtain a binary value, when they are below the threshold they become white and when the are above the threshold they become blue. From figure 4.8 we can observe how drift in brightness changes the background values for the differential scheme hiding the feature of interest in the image.

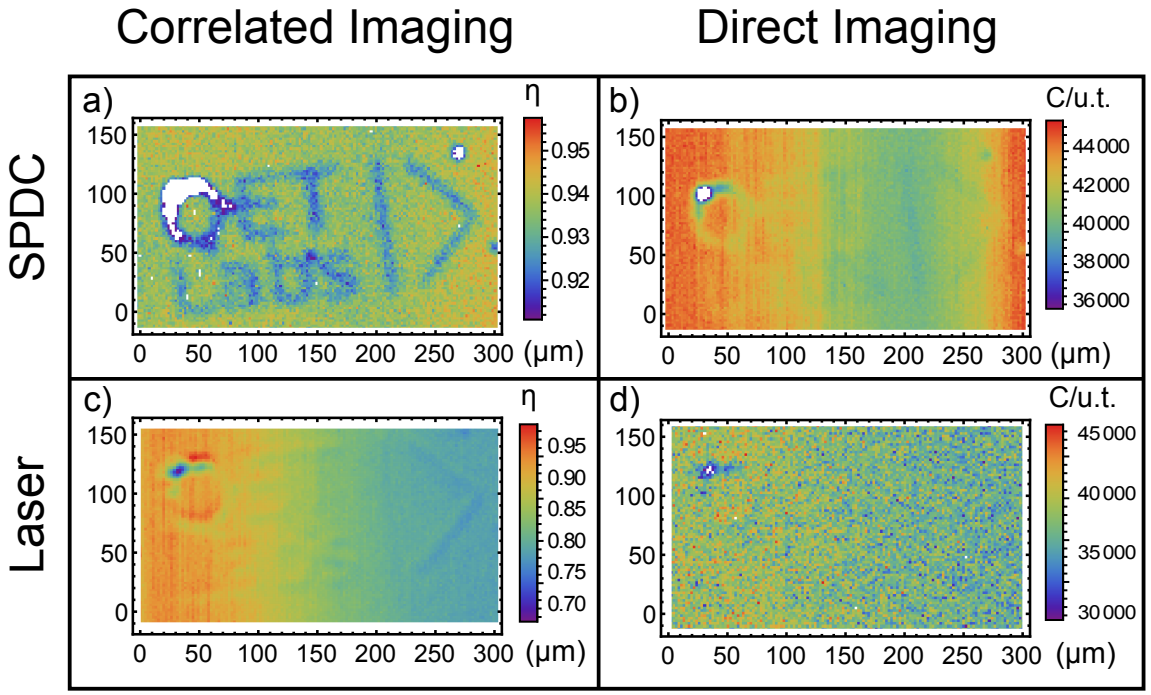

FIGURE 4.7: **Experimental Results.** a) Noise-reduced image reconstructed with twin beams. b) Single-photon direct image without correlation using only the CCD camera measurements and ignoring the measurements in the reference channel. c) Differential imaging using an attenuated laser. d) Direct imaging using an attenuated laser. Each image is 150 by 75 pixels. The step size of each pixel is 0.2 μm. the integration time per pixel is 0.5 s.

We have so far shown qualitatively the performance of our scheme but in order to demonstrate sub-shot-noise behaviour we need to acquire multiple images and then analyze the statistics pixel by pixel. Since our imaging system is slow ($\sim$ 0.5 s per pixel), it would

[2]There are frequency modulation techniques that can alleviate the adverse effects of drift but those

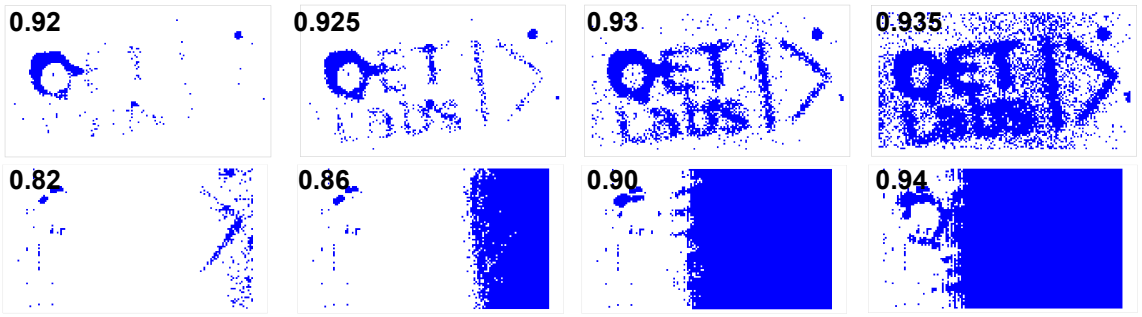

FIGURE 4.8: **Binarized images.** The images on the top side are binarized versions of figure 4.7 a) which was taken using the twin beam scheme. The images on bottom are binarized versions of figure 4.7 b) with a differential imaging scheme. The transmissivity threshold is shown on the upper left corner of each image.

take too long to build up enough statistics for an image with the size as the one presented in figure 4.7 a) (150 x 75 pixels). Because of this, we constrained our demonstration to a subsection of the sample and took 80 images to perform the statistical analysis. For this we need to demonstrate that the precision ratio, Γ, is greater than one.

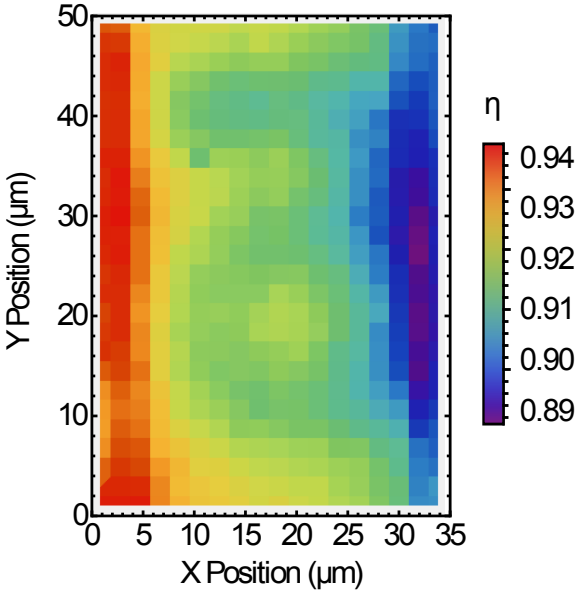

FIGURE 4.9: **Multiple scan image.** The image shows a subsection of the image presented in figure 4.7 a) corresponding to the later "a" . The image is 18 by 26 pixel with a step size between pixels of 2 μm. Each pixel has been recorded 80 times with an integration time of 0.5 s. The gradient between the left and right side is due to slow drift in the source brightness.

In figure 4.9 we show an image constructed with the mean transmissivity of the eighty measurements. The mean precision ratio of the image shown in figure 4.9 is 1.56 ±0.2, this

value is comparable to the expected precision ratio of 1.54 calculated from the calibration curve in figure 4.4. The precision ratio is obtained by comparing our results to those that would be obtained with a noiseless coherent source of illumination measured with 100% efficient detector. If compared to a coherent source measured with the same efficiency as our detector (90%), the precision ratio would increase to 1.76 ±0.2.

As the sample transmission is not homogeneous across the sample, the expected advantage in precision varies across the different regions of the image. In figure 4.10 we construct a histogram of the transmissivity of figure 4.9 which could be use to translate transmission into the expected precision ratio using the calibration curve in figure 4.4.

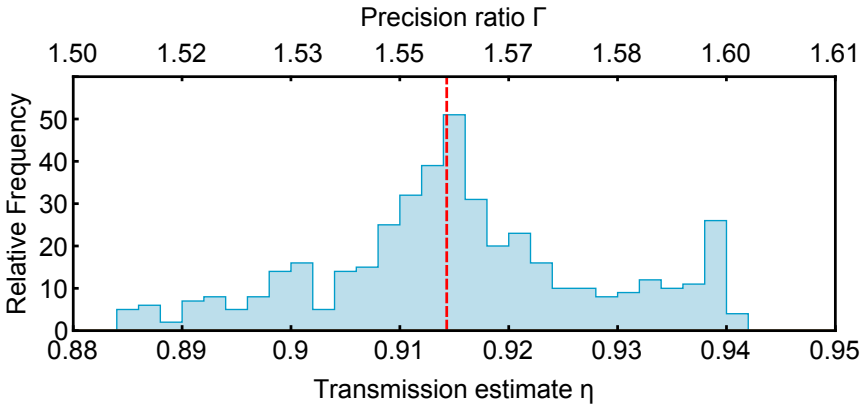

FIGURE 4.10: **Histogram of transmissivity for figure 4.9.** The figure shows a histogram of the transmissivity of the image in figure 4.9 which can be related to the expected precision ration calculated by the plot in figure 4.4. The mean transmissivity, shown as the red vertical line, is η =0.914 with an expected mean precision ratio of 1.54 which is comparable to the measured mean precision ratio of 1.56 ±0.2

Due to the agreement between the experimental and expected values of the precision ratio we expect that the system performs according to calibration so we can then estimate the expected precision ratio for the full image shown in figure 4.7 a) using the curve in figure 4.4, obtaining a value for Γ of 1.57.

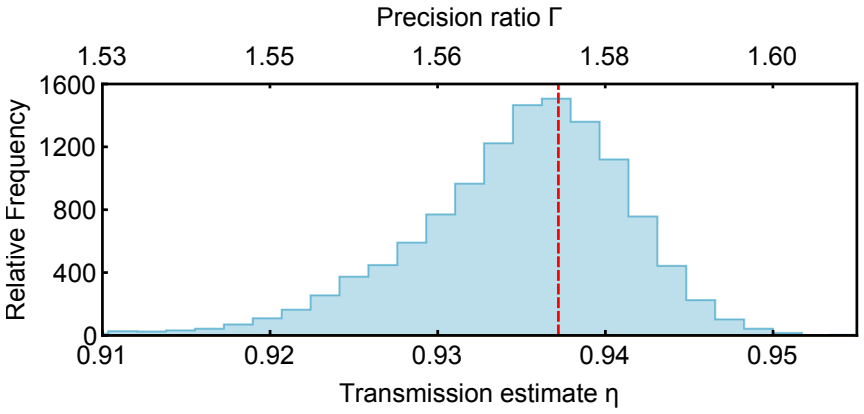

FIGURE 4.11: **Histogram of transmissivity for figure 4.7 a).** The mean transmissivity of figure 4.7 a) is η =0.93, represented by the red vertical line, this translates into an expected precision ratio of 1.57.

4.6 Conclusions

To summarize, we have implemented a sub-shot-noise imaging scheme using twin beams, feed-forward and a hybrid detection scheme.

We have recorded an image and performed an analysis that evidences absolute sub-shot-noise performance. We have obtained a precision ratio of 1.56 $\pm$0.2 when comparing our results to an ideal coherent direct imaging scheme, and 1.76 $\pm$0.2 when compared to a coherent scheme measured with the same detector efficiency as in our setup. The resolution of our imaging system can resolve features of up to 3 μm. In comparison with the wide field microscope presented in [83] our imaging system is slow due to the need to raster scan the sample. However, we can achieve higher resolution whilst maintaining a high quantum advantage. Also our probe beam is emitted from a single mode fibre making the resolution of our imaging system close to diffraction limited. As well, our system could be compatible with confocal microscopy which also requires raster scanning. Nevertheless, a way to increase the speed of the imaging acquisition but at the cost of reducing the resolution is by implementing a compressed sensing algorithm [86]. These type of algorithms are able to reconstruct an image from a reduced set of measurement and are advantageous for application that require classification of an image rather than their precise reconstruction.

As discussed previously loss is one of the major drawbacks for twin beam noise reduction schemes. Our implementation of feed-forward and use of a high detection efficiency camera have minimized detection based loss. We expect that further improvements to these type of schemes can be made by optimizing the filtering and collection efficiency. Another problem that we expect to tackle in the future is the drift of the brightness of the source. We suggest introducing a PID loop that aims to control the number of photons on the reference beam by controlling the intensity of the pump beam. This will suppress low frequency noise.

To conclude, we believe that our scheme could be readily applied in scenarios where it is desired to image a sample with high resolution at the single photon level [64]. However, a common critique to noise reduction schemes using twin beams from spontaneous sources is their low intensity. In our setup the bandwidth of the switch and saturation of the detectors prevent us from operating with much higher intensities. Further work has to be done to reach intensity levels that would bleach a biomarker for imaging or to fully damage a biological sample. As long as the single photon flux of the source remains at the femtowat level it is not clear if the results presented here would have a wide range of applications. Nevertheless there are ad hoc samples that require illumination at the single photon level. For instance we could spatially characterize the efficiency profile of a single photon detector using our heralded photon source. This is a sample which is sensitive and prone to damage at low light fluxes. As a proof of principle we conducted an experiment replacing our sample with a couple of APDs. This of course reduces the attainable advantage due to their lower quantum eficiencies but it evidences a scenario where imaging at low photon levels is necessary. In fig. 4.12 we present our results of the spatial characterization of two APDs, an ID Quantique and an Excelitas. We compare their efficiencies by taking the nominal efficiency given by the data-sheet of the Excelitas detector at the wavelength of interest.

By using this technique we found that the ID Quantique detector has a $\sim$10% higher efficiency than the Excleitas detector. We also show that the ID Quantique detecor appears

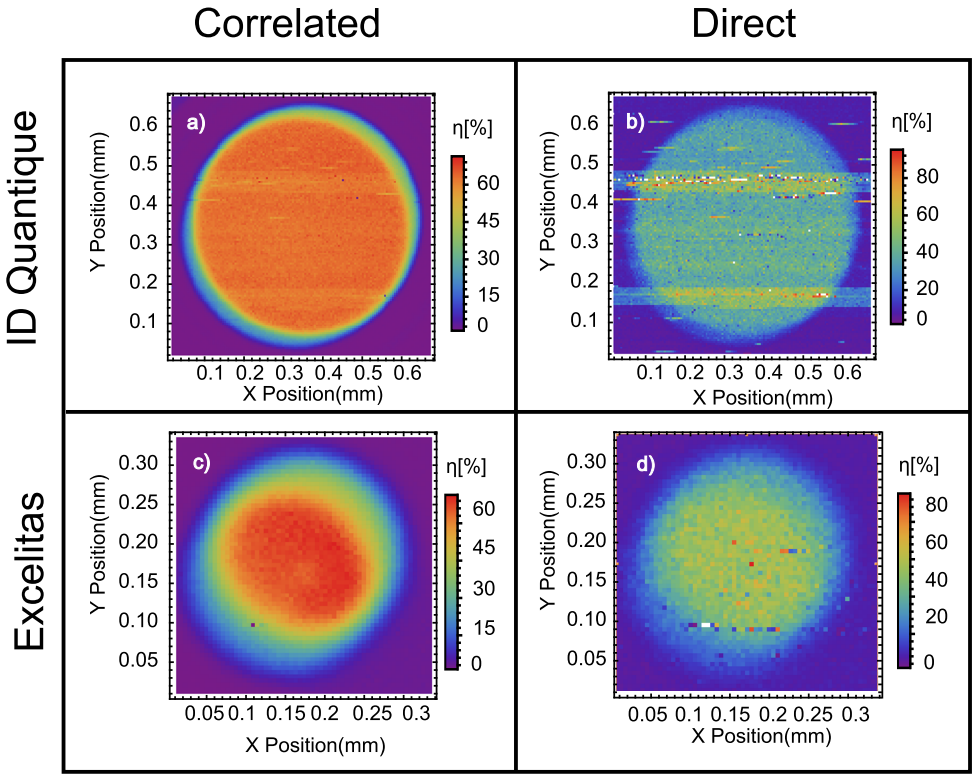

FIGURE 4.12: **Histogram of transmissivity for figure 4.7 a).** The mean transmissivity of figure 4.7 a) is η =0.93, represented by the red vertical line, this translates into an expected precision ratio of 1.57.

to have a more homogeneous active area than the excelitas al.

To conclude, we consider that to reach higher brightness and reach levels that could indeed damage biological samples we could adapt to our setup the scheme presented in [87], in this work noise from an SPDC source is suppressed in post-selection by selectively correlating beams within a narrow threshold of intensity. It is possible to substitue our single photon feed-forward scheme by a threshold based feed-forward scheme where instead of heralding single photons we could herald beams within a specific intensity threshold. This would enable us to increase the intensity on the sample whilst maintaining sub-shot-noise performance.

Chapter 5

Klyshko efficiency optimization using a genetic algorithm

Statement of Work:I conceived and designed the experiment with Paul-Antoine Moreau. I built the setup, performed the experiment and analyzed the data. The genetic algorithm was provided by Robert Fickler and adapted for this experiment by Paul-Antoine Moreau and Alex McMillan. This work was performed under the supervision of John Rarity and Jonathan C. F. Matthews.

5.1 Introduction

Single photon sources (SPS) lie at the heart of many quantum technologies. They are essential building blocks for quantum cryptography [88], optical quantum computing [89] and optical quantum metrology [90]. To successfully harness the advantages promised by all of these applications, it is necessary to efficiently supply and detect the majority of the photons that go through the underlying protocols. Advances in single photon detection technology have shown that near unit efficiency is at hand [91, 92]. Hence the attention has shifted towards optimizing the extraction efficiency of SPS [93–95] State

of the art, spontaneous parametric down-conversion (SPDC) sources have shown higher performance [78] as compared to the highest reported extraction efficiency of solid state emitters [96]. Improvements on the quality of SPDC sources have enabled loophole-free Bell tests [97, 98] and absolute sub- noise measurements [82, 84] but these improvements are insufficient to satisfy the stringent requirements that would exploit the advantages posed by more complex quantum protocols as photonic quantum computing [99]. Loss of the down-converted photons due to inefficient coupling into optical fibers is a major roadblock and is one of the most common sources of loss in practice. Optimizing the collection efficiency has been the focus of extensive theoretical and experimental analysis [20, 95, 100–102]. Here we attempt to alleviate inefficient coupling by implementing a genetic algorithm GA that manipulates the spatial profile of down-converted photons by manipulating the spatial profile of the pump beam. By this means we obtain an improvment of $\sim$6% in coupling efficiency.

5.2 Motivation

Parametric down conversion is a nonlinear process in which a bright pump field interacts with the nonlinear medium, in the process a photon from the pump beam is absorbed giving rise to the emission of a pair of photons that satisfy conservation of energy and momentum. We usually refer to these photons as signal and idler. In an ideal scenario when we detect an idler (signal) photon we can then herald the presence of its conjugate with unit probability, however, inefficient detection and transmission losses prevent us from doing so. This happens when a photon is detected in the signal path, for example, but the correlated photon is not present in the idler arm. Experimentally, we can estimate this probability by measuring the ratio between the number of coincidence counts across the signal and idler channel, N_{IS}, and the number of single counts on the signal (idler) arm, $N_{S(I)}$,

$$\eta_{I(S)} = \frac{N_{IS}}{N_{S(I)}}. \tag{5.1}$$

As we did in throughout the previous chapters, we refer to $\eta_{I(S)}$ as the Klyshko or heralding efficiency [1] idler (signal) channel.

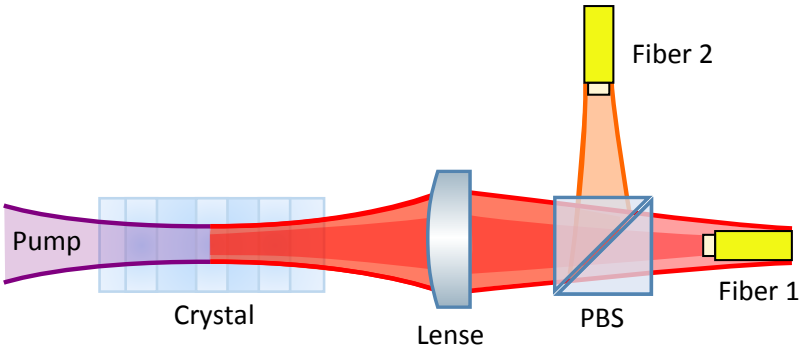

FIGURE 5.1: **Illustration of beam propagation for a collinear down-conversion source.** The figure depicts a scenario where channel 2 is efficently coupling all of the down-converted light but channel 1 is only coupling a fraction of it, the darker red region. This means that if channel 2 was heralding the presence of a photon in channel 1 it would do it with a non-unitary probability, $\eta_1 < 1$ even though fibre 2 is collecting all the light.

There are different examples of quantum application which require a minimum value of η to operate. For example, one-sided device-independent QKD requires $\eta > 66\%$ [103], sub-shot-noise transmission estimation requires that the sum of the efficiencies $\eta_I + \eta_S > 1$ [53]. A table showing efficiency requirements for other applications can be found in Ref. [93].

In many instances it is desired to couple the down-converted photons into optical fibers, this makes the source more versatile and it could also enhance the Klyshko efficiencies due to the mode selectivity of the fibers. In the case of a fiber coupled source, the overlap between the fiber collection modes and the mode of the down-converted photons (which in turn is defined by the mode of the pump beam) will be one of the factors that determine the final value of η. There has been an extensive analysis devoted to the study of the experimental conditions that lead to an optimal coupling. The work of Ljunggren *et*

[1] We prefer the term Klyshko efficiency over heralding because when implementing feed forward the term heralding efficiency only applies for one channel.

al [102] and Bennink *et al* [95] suggest that with the right focusing conditions it is possible to obtain values of η >95%. However, when accounting for transmission loss and detector efficiencies, experimental demonstrations have not reached the suggested optimal values. To our knowledge the highest efficiency reported to date has been obtained by Kaneda *et al* [104] with a value of η =91%. In table 5.1 we present a list of some of the sources with the highest reported values.

TABLE 5.1: **Comparison between different SPDC sources with high Klyshko efficiencies.** The table is adapted from Ref. [105].

Reference	Material	λ (nm)	Detector	η^{corr}(%)	η(%)
Pereira *et al.* [106]	PPKTP/bulk	810	APD	84	42
U'Ren *et al.* [107]	PPKTP/WG	800	APD	85	51
Weston *et al.* [108]	PPKTP/bulk	1570	SNSPD	80	64
Slussarenko *et al.* [82]	PPLN/bulk	1550	SNSPD	84	80
Kaneda*et al.* [104]	PPKTP/bulk	775 (1590)	SNSPD (INGAS)	90 (91)	39 (6)
Shalm *et al.* [98]	PPKTP/bulk	1550	TES	83	75
Giustina *et al.* [97]	PPKTP/bulk	810	TES	82	78
Ramelow *et al.* [78]	PPKTP/bulk	810	TES	86	82
Montaut *et al.* [105]	PPLN/WG	1560	SNSPD	54	46
Moreau *et al.* [84]	PPKTP/bulk	818	CCD	72	65

One of the reasons for not reaching the optimal values could be due to experimental imperfections that modify the parameters suggested by the theoretical models. For example, the distances between lenses and the crystal may not be measured to high accuracy or a beam traveling off the axis of an optical components could lead to aberrations. It is known that spatial mode of the down-converted beams inherit properties from the spatial profile of the pump [109]. Inspired by the work of Fickler *et al.* [110] where a GA algorithm is used to demultiplex transverse optical modes into spatial modes, here, we attempt to improve the coupling efficiency of the down-converted twin beams of a SPDC source by actively modifying the spatial profile of the pump beam. To this end we use a SLM that reflects the pump beam and is controlled by a GA in order to manipulate the spatial mode profile of the pump beam. The figure of merit of the algorithm is Klyshko efficiency. The algorithm can also be implemented on the down converted beams but SLM's are lossy components so it is more convenient to manipulate the pump beam. Also, by manipulating the pump we can optimize other parameters of the source. It is known that there is a trade-off between

brightness and Klyshko efficiency [95]. Using the SLM and the GA it would be possible to change the parameter depending on the desired applications.

5.3 Experimental Setup and Procedure

Before building the setup we first estimated numerically the Klyshko efficiency that can be attained given the characteristics of our pump laser (CW 404 nm) and crystal, a 30 mm PPKTP crystal phase-matched for type-II down conversion around 808 nm. A detailed explanation on how to perform this estimation is given in Refs. [95, 104]. Here we used an online calculation tool called SPDCalc to perform this calculations Ref. [111] and obtained a plot showing the pump and down-converted waists versus η in Fig. 5.2.

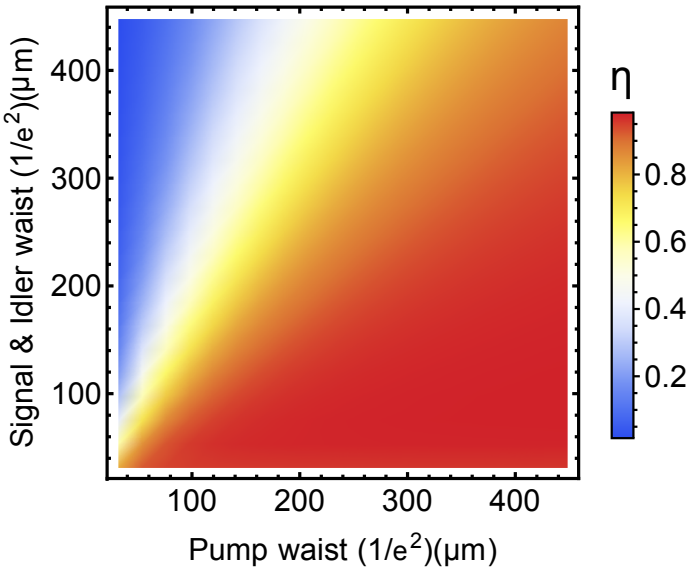

FIGURE 5.2: **Numerical prediction of Klyshko efficiency.** The plot presents a maximum efficiency of 98.4% at the lower right corner, this is for the largest pump waist of 400 μm and signal and idler waist of 20 μm

The first step was to align the down conversion source using a fiber coupled laser following the parameters given by our numerical predictions. The waist of the beams were measured with a beam profiler. We obtained a spot size of $\sim$300 μm for the pump beam. This value was chosen as an initial trade off between the optimal waist as suggested by Fig. 5.2 and the clipping of the Gaussian mode due to the $<$ 1 mm aperture of the crystal. The waist of

the signal and idler beams was measured outputting an alignment laser from the collection fibers obtaining values of ∼100 μm. Once these values were measured, we overlapped the beams and positioned the crystal so that the focal spot of the three beams was placed at the center of the crystal. After the initial alignment with bright lasers we then introduced filters and polarization components and carried on with the alignment of the source with down-converted light. During this process we vaired the initial beam-waist values and iterated them until we obtained a maximum symmetric Klyshko efficiency of 35%. To further increase the efficiency and to reduce the loss due to misalignment we replaced the idler channel fiber with a multimode fiber. By doing this, we allow stray light to be coupled into this fiber, this increased the number of single counts by an order of magnitude and decreased the Klyshko efficiency of the signal channel to ∼1% but this increased the Klyshko efficiency of the idler channel to 39%. For the rest of this chapter we will only focus on the efficiency of the idler channel.

To obtain an estimate of the coupling efficiency it is necessary to determine the loss budget of the system. In table 5.2 we present the detector efficiency and the transmittance of the optical components after the crystal. From the table we estimate that the source has a ∼50% loss budget this means that the Klyshko efficiency should reach the same value, however the experimental measurement yield a value of 39%. This difference suggests that the coupling efficiency of the source was ∼78%.

TABLE 5.2: **Loss budget.** Each component's values were obtained from their respective datasheets.

Component	Transmission (%)
PPKTP	99
LPF	98
BPF	98
PBS	98
AR coated (one end only) fiber	96
Detector window	99
Detector efficiency	58
Theoretical coupling efficiency	98.4
Overall transmission	50

Once the source was aligned and no further improvements on the Klyshko efficiency were achieved we switched the pump to a beam that was spatially modulated by the SLM as

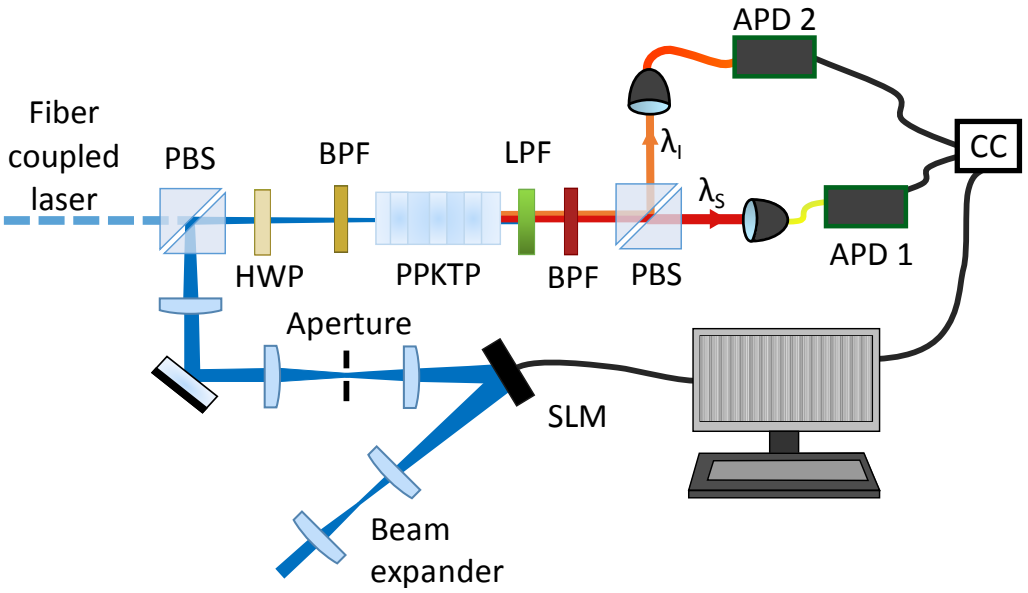

FIGURE 5.3: **Experimental setup.** The polarization of the pump was controlled using a HWP and a PBS. Before the crystal we filtered out the pump beam with a band-pass filter that transmits from 355 to 610 nm. We used a long-pass filter (LPF) with a cut-off wavelength at 715 nm and a 20 nm band-pass filter (BPF) centered at 810 nm to remove the residual pump after the crystal. Once the pump was filtered the signal and idler beams were separated using a polarizing beam splitter (PBS) and coupled into a single mode (signal) and a multimode fiber (idler). The spatial mode of the pump beam was modified using an SLM running a GA set to optimize the Klyshko efficiency of the source. Photon pairs are separated using a PBS and collected using a single mode fiber and a multimode fiber.

seen in Fig. 5.3. For this we first applied a blazed grating on the SLM and filtered out the first order of diffraction using a pinhole. This guarantees that this beam was entirely modulated by the SLM. After that we introduced a lense with a 20 cm focal length to focus the pump inside the crystal. We then overlaped the path of the diffracted beam onto the the path of the fiber-coupled laser pump. Once both beams were overlaped, the GA was set to start from a mask consisting of 512 x 512 pixels which corresponds to the spot size of the beam on the SLM ($\sim$3 mm). On the first stage of the algorithm we overlay the blazed grating with a set of 4 different squares and then ran the GA with a population of 40 masks that vary the gray-scale of each square. Each value of the gray scale can be mapped into a phase shift from 0 to 2π. The algorithm runs until it found that no population improved the figure of merit. When this happened it then subdivides the squares, inheriting the "genes" or the properties of the previous population and ran

the algorithm again. This subdivision carries on until it reaches the maximal resolution of the SLM. The algorithm ran at a rate of 2 masks per second. A diagram depicting the evolution of the algorithm is shown in Fig. 5.4.

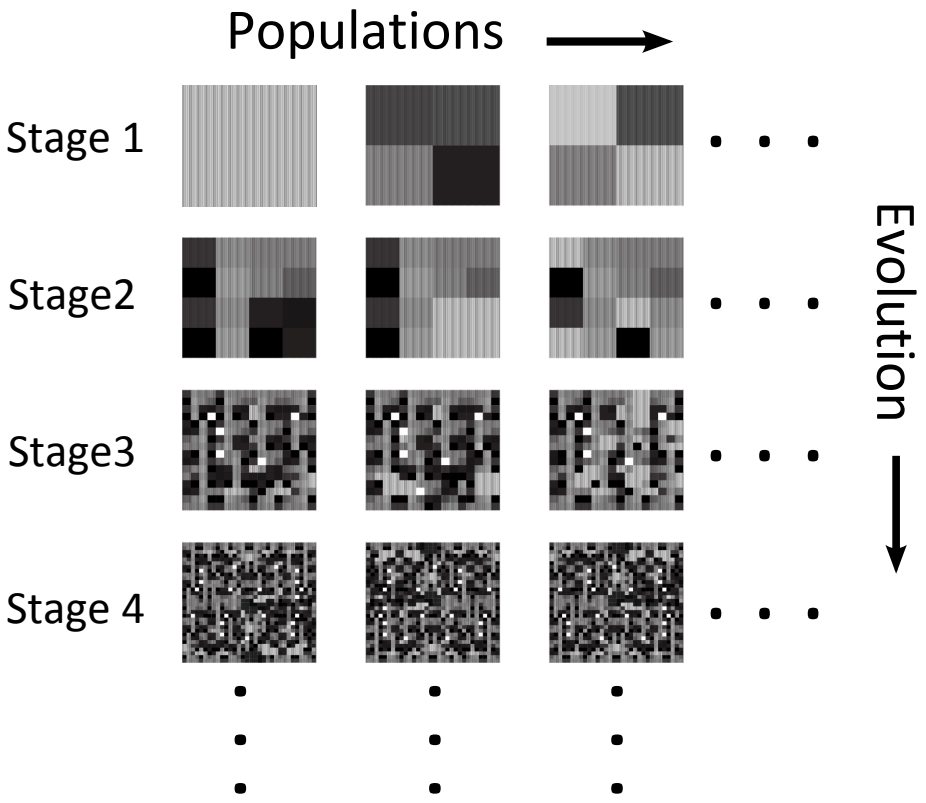

FIGURE 5.4: **Mask refinement of the GA.** The algorithm starts from a blazed grating. On the first stage of the algorithm, the initial mask is divided into four sections. Then the algorithm generates a population of 40 masks, randomly varying the gray scale value of each square. The GA searches for a mask that improves the figure of merit until it reaches 10 populations that do not improve the figure of merit. When this happens it further divides each square into four subsections and runs the algorithm again. This carries on until reaching the maximum resolution of the SLM, one square per pixel.

We have chosen a genetic algorithm as an approach to optimize the efficiency of the source due to two characteristics of the problem at hand. One is that the it is a problem where it is easy to evaluate the fitness function. Second the fact that the dimensionality of the search space is extremely big, this is a scenario where a GA is generally used. If the search space was constrained, for example by only searching with in a particular set of masks from the SLM like the Fresnel zone plates then perhaps other approaches could be more convenient.

5.4 Results

The results of the GA are shown in Fig. 5.5 a). The system started with a Klyshko efficiency of 24% and reached a maximum Klyshko efficiency of 42%, which is beyond what we were able to achieve aligning by hand. This translates into an improvement from an estimated 78% coupling efficiency to 84%. It took the algorithm 58 minutes to reach this value, which is 175 generations and ∼7000 trials. From Fig. 5.5 b), we can appreciate how the rate of coincidences decreases from its starting value (3000/0.5 sec) and oscillates until it plateaus around 2000. It is known that there is a trade-off between the focusing conditions that yield the optimal Klyshko efficiency and highest coincidence-count rate of an SPDC source [95]. It is important to be aware of this trade-off when aligning the source, because aligning to the highest coincidence-count could be misleading if the objective is to improve the Klyshko efficiency. It is an attribute of the algorithm to directly improve the Klyshko efficiency regardless of the coincidence-count rate.

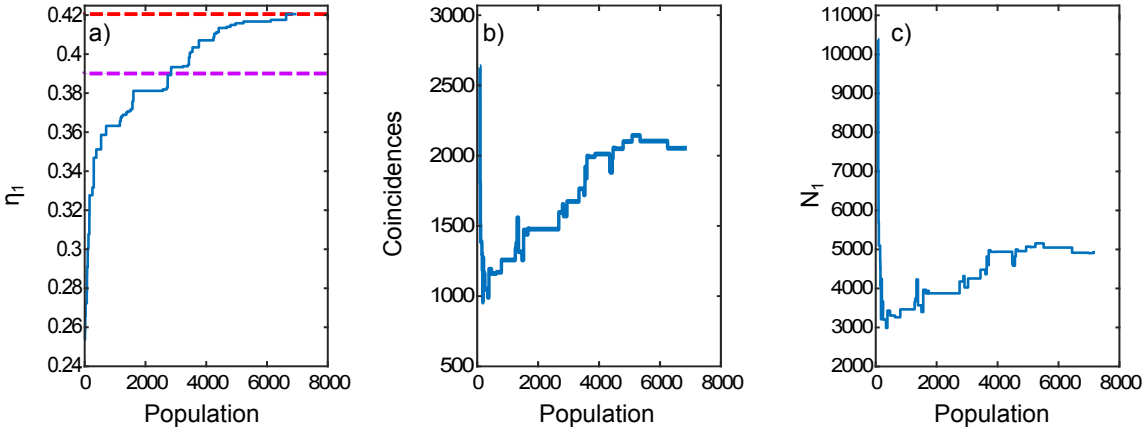

FIGURE 5.5: **Klyshko efficiency optimization.** In the plots shown here the algorithm is set to optimize the Klyshko efficiency. a) In this plot we show the evolution of the highest Klyshko efficiency vs the population size. The purple dotted line shows the best efficiency obtained by hand with the discussed setup, the red dotted line shows the best efficiency obtained with the GA. b) In this plot we show the evolution of the rate of coincidences vs the population size c) In this plot we show the evolution of the rate of single counts vs the population size.

We can also substitute the figure of merit of the GA to optimize different parameters, for example, in Fig.5.6 we set the algorithm to optimize the number of coincidences. We

started the algorithm from the mask that returned the best Klyshko efficiency. In this case we can observe how the coincidences increase as the the Klyshko efficiency decrease. We observed a nearly two-fold increment in the number of coincidence counts (from 1800 to 3400 per 0.5 seconds) with out increasing the pump power.

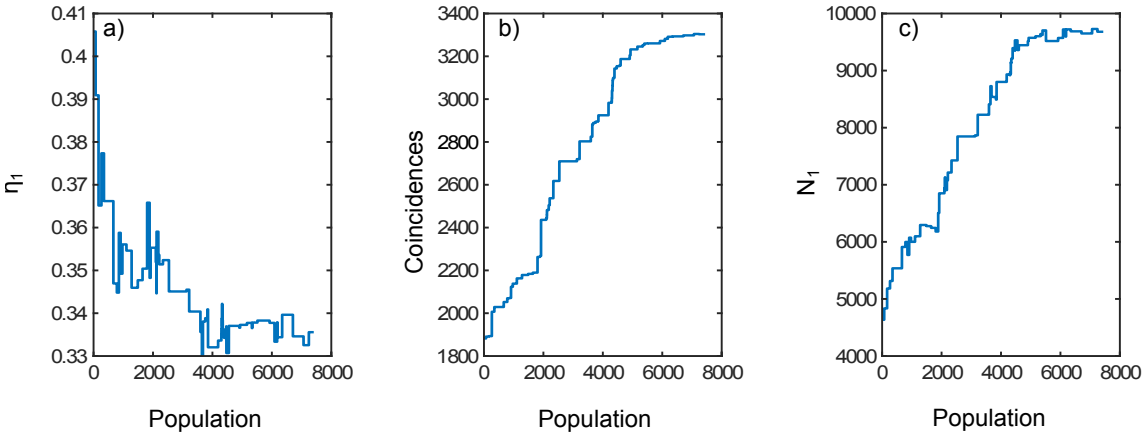

FIGURE 5.6: **Brightness optimization.** In the plots shown here the algorithm is set to optimize the brightness (the coincidence rate). a) In this plot we show Klyshko efficiency vs the population size. b) In this plot we show the evolution of the rate of coincidence counts vs the population size. c) In this plot we show the evolution of the rate of single counts vs the population size.

To further understand how the algorithm is operating we analyzed the pump-beam's spatial profile using a profileometer at the transmission port of the PBS that reflects the pump into the crystal. In Fig.5.7 we show five masks and their corresponding beam profiles. Each one of them corresponds to a step with the highest increment of the figure of merit of a run of the algorithm (in this case it was the brightness of the source). As seen in the figure we start with a Fresnel lens superimposed to a diffraction grating. Since the changes on the spatial structure are hard to perceive by eye in Fig.5.8 we plot the behaviour of the beam's diameter and its centroid. In Fig.5.8 a) we see that the algorithm is reducing the beam's diameter, this is as expected since a highly focused pump beam is necessary to increase the brightness, We can also see from Fig.5.8 b) that the general trend was to shift the pump to the left. From this results we see that the GA is both shifting the beam around to obtain a better alignment with the collection fiber and at the same time is changing the focusing conditions to satisfy the conditions set by the figure of merit. This

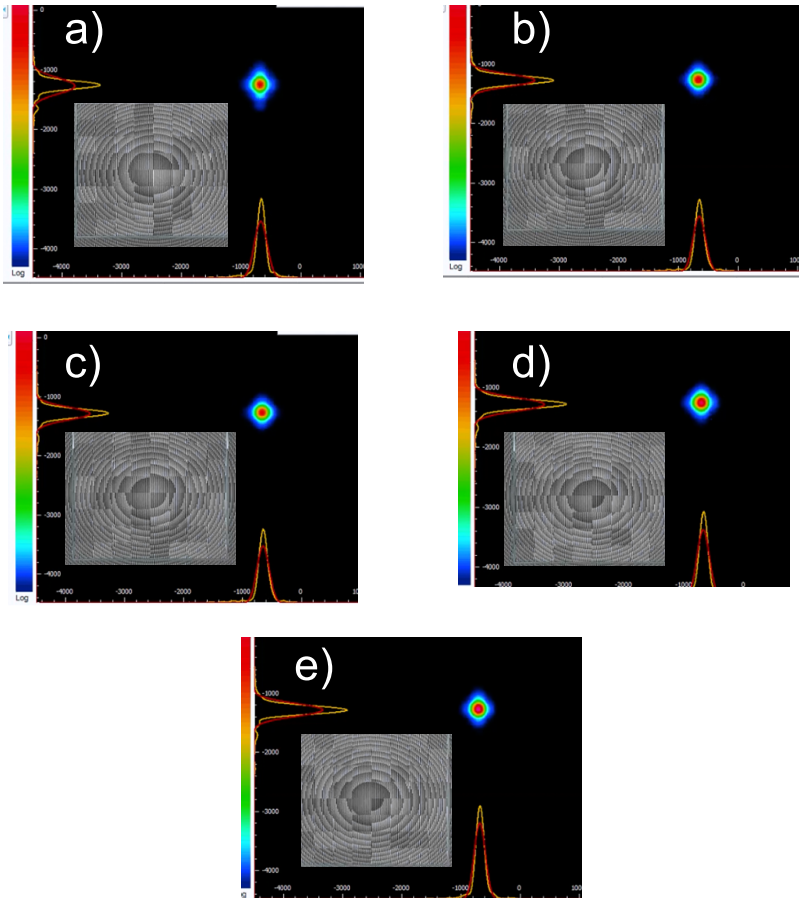

FIGURE 5.7: **Beam profiles and masks for brightness GA.** The figure shows the progression of the algorithm in alphabetical order; a) being the starting point and e) the final point, i.e, the one with the highest count rate .

can also be perceived in Fig.5.9 and Fig.5.10 where the the beam is also being shifted to the left but in this case the beam's diameter in not focused so tightly as it is desired for a high efficiency source.

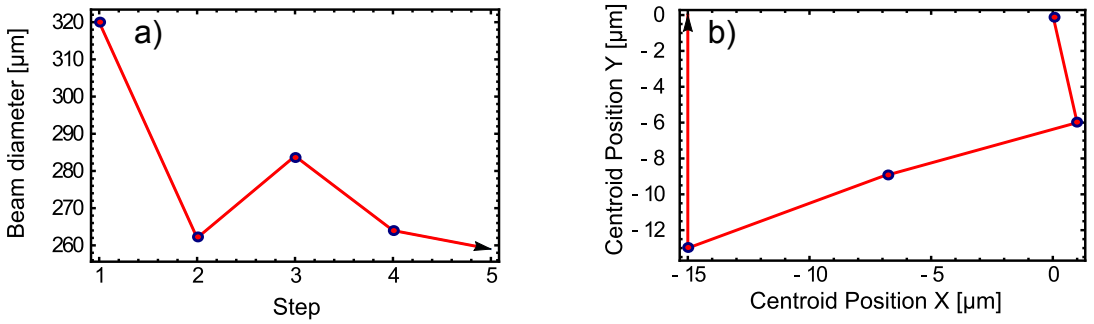

FIGURE 5.8: **Centroid and Beam diameter for the GA improving brightness.** On the left hand side we have the mean diameter of the pump and on the right hand side a plot with the coordinates of the pump's centroid.

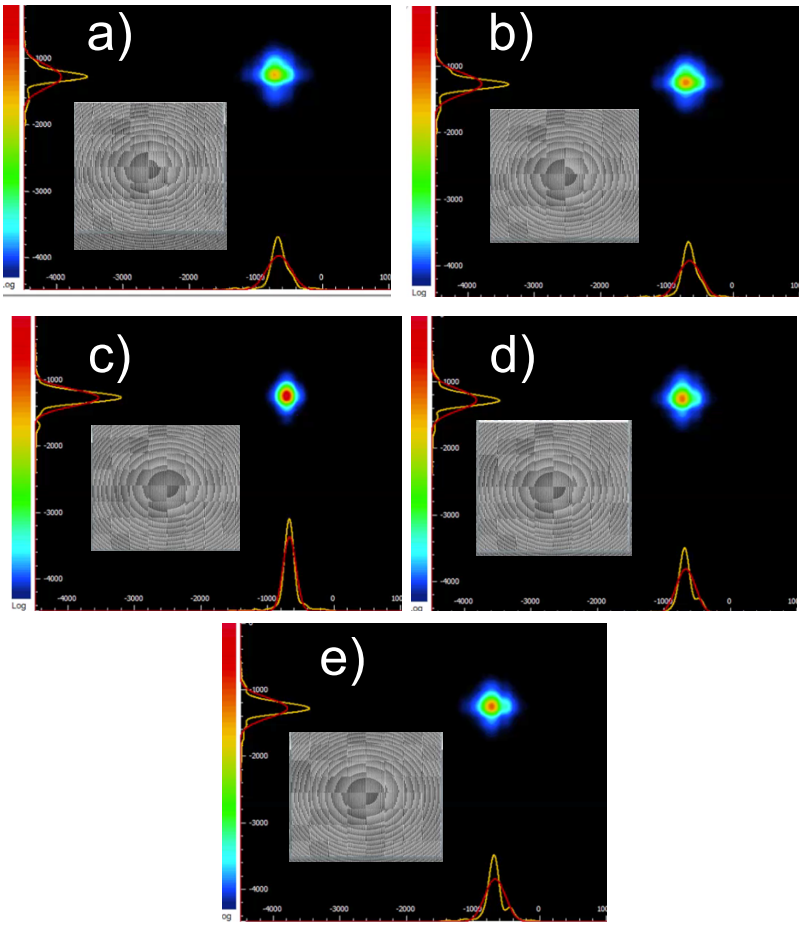

FIGURE 5.9: **Beam profiles and masks for brightness GA.** The figure shows the progression of the algorithm in alphabetical order; a) being the starting point and e) the final point, i.e, the one with the highest mean efficiency.

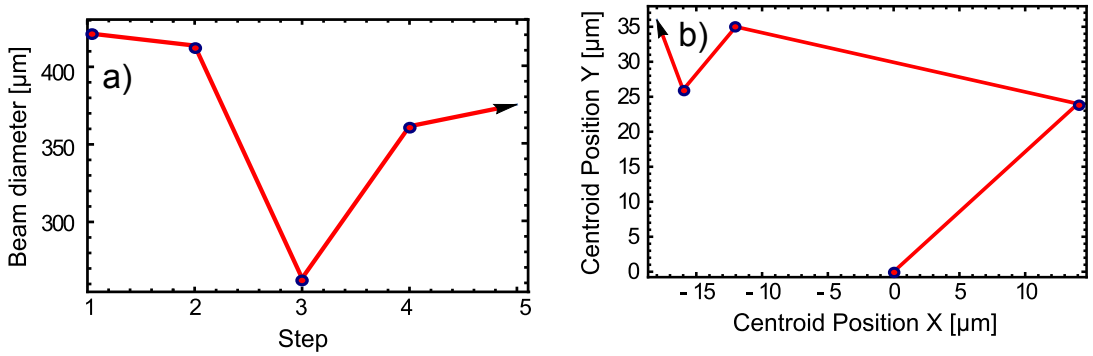

FIGURE 5.10: **Centroid and Beam diameter for the GA improving efficiency.** On the left hand side we have the mean diameter of the pump and on the right hand side a plot with the coordinates of the pump's centroid.

5.5 Conclusions

In this chapter we have made use of a GA and an SLM that spatially modulates the pump beam of a SPDC source to improve its Klyshko efficiency and its brightness. By manipulating the pump, we have obtained an improvement in coupling efficiency of 6% and we have almost doubled the number of coincidences. Even though the results presented here are positive they are still in a preliminary phase. First we could experimentally characterize the transmission of each component independently to confirm the loss budget in table 5.2 which is currently based on vendor data sheets. It would also be of interest to run the algorithm multiple times and observe if it always converges to the same value so that we can understand if the algorithm is reaching a local or a global maximum.

We should clarify that the motivation for this experiment was to improve the coupling efficiency so that we could obtain a higher advantage in our quantum-enhanced transmission estimates discussed in previous chapters. Even-though the source presented in this chapter has the same design and used the same components as the one presented in Chapters 3, 4 and 5 we were unable to reach the same value of Klyshko efficiency as the one reported in previous chapters[2]. In the future we expect to use the scheme presented here with the higher efficiency source (used in chapters 3, 4 and 5) and observe if we can improve that source's coupling efficiency and if the SLM is stable enough to show sub-shot-noise behaviour.

5.6 Outlook

We believe that the use of a GA in combination with an SLM to optimize different parameters of an SPDC source is a tool that has not been exploited thoroughly. For example the GA can be set to control spectral properties of the pump beam as in Ref. [112], this could

[2]There could be variety of reasons for not reaching the same level of efficiency. For example human error in the alignment. Spectral properties of this source have not been characterized. This means that the filters and coupling condition might no be equal. Also detectors might have completely different efficiencies and dark counts.

be useful when it is necessary to tailor the temporal properties of the down converted photons so that they can increase the probability of the excitation of atoms in quantum memories [113, 114]. It can also be used in combination with crystals that have a fan-out [115] poling period, to control the spectral properties of the down-converted photons. The scheme presented here can also be used if a source requires remote alignment, for example could be for SPDC sources used in satellites [116]. Furthermore shaping the pump pulse with the GA can also be useful in the context of other single photon sources. In the case of photon-pair sources using four-wave mixing in optical fibers the phase matching condition can be satisfied via modal dispersion [117]. Furthermore, a similar approach can be used to improve the mode matching between the pump laser and a micropillar resonator to improve the generation opf single photons in quantum dots [118].

Chapter 6

Beating the Shot-Noise Limit with Sources of Partially-Distinguishable Photons

This chapter is based on the manuscript: *Beating the shot-noise limit with sources of partially-distinguishable photons* by Patrick M. Birchall, Javier Sabines-Chesterking, Jeremy L. O'Brien, Hugo Cable, Jonathan C. F. Matthews arXiv:1603.00686 (2016)[119].

Statement of Work: Patrick Birchall designed the experiment presented in this chapter. I performed the experiment and co-analyzed the data with Patrick Birchall. This work was performed under the supervision of Jeremy L. O'Brien, Hugo Cable and Jonathan C. F. Matthews.

6.1 Introduction

The precision of an optical phase measurement using a coherent state of light is fundamentally limited by the distribution of random photon numbers generated. The photon-number distribution of a coherent state follows a Poissonian distribution and therefore an intensity measurement is shot noise limited, this means that the precision scales as $\Delta\theta \propto 1/\sqrt{N}$ [47]. Non classical states of light offer the possibility of measuring an optical phase with higher precision than that of a coherent state [120]. In the ideal scenario quantum strategies can reach a precision which scales as the inverse of the mean total number of probe photons $\Delta\theta \propto 1/N$, this is known as the Heisenberg limit [120]. In practice it is challenging to reach this level of precision. Experimentally there are many hurdles that have to be overcome to achieve Heisenberg scaling. For example precision degrades with optical loss and decoherence. These effects have been extensively studied [49, 121, 122], but little attention has been paid to the role of photon distinguishability in optical quantum metrology which is the focus of this chapter.

Typically optical quantum information and metrological protocols exploit quantum interference of photons which are considered to be indistinguishable [123]. Experimental demonstrations of such strategies have been shown using spontaneous single photon sources (SPS) [124] which require stringent spectral filtering that leads to a higher optical loss budget hindering the advantage of such strategies. On the other hand solid state SPS only achieve high distinguishability through temporal demultiplexing [125] of a single emitter, another source of loss; whereas distinct emitters have so far shown poor distinguishability [126, 127]. When scaled to large photon numbers, state of the art single photon sources are still yet to achieve the distintguishability thresholds required for photonic universal quantum computers but could still be useful for some metrological schemes. Here we study the performance of a quantum probe state containing photons with partial-distinguishability and compare it to a shot-noise limited probe state.

The canonical way of measuring distinguishability in quantum optics is via Hong-Ou-Mandel (HOM) interference [128]. HOM interference is a photonic interferometric effect

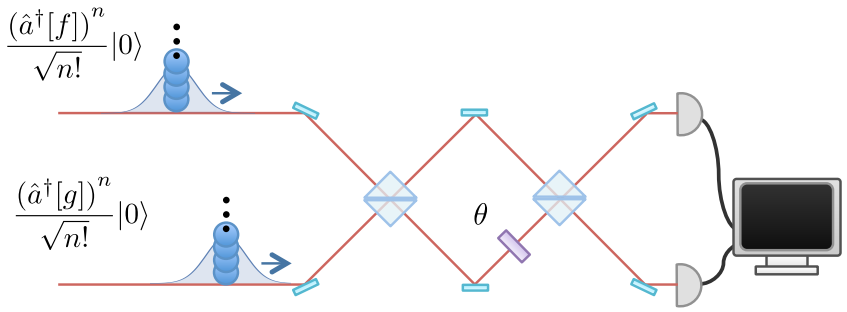

FIGURE 6.1: **Experimental scheme.** Temporal mode-mismatch introducing particle distinguishability before state enters MZI.

in which photons entering a beam splitter bunch into a single spatial mode exiting the beam splitter together in either one of the output ports. The experimental signature of this effect is a dip in the coincidence event count between two distinct exit ports of a beam splitter as a function of the arrival time between input photons. The dip is a resource that contains spectral and temporal information about the photons but it's also a measure of their distinguishability [129]. A dip that reaches zero coincidences corresponds to the case where photons are perfectly indistinguishable. In this report we perform interferometric measurements in a Mach-Zehnder-like interferometer inputting quantum states composed of two and four photons with different degrees of distinguishability. We observe the prevalence of supra-classical phase sensitivity despite a high degree of distinguishability.

6.2 Theory

In this section we will first introduce a theoretical model to establish a measure of distinguishability. After that we will define a gauge for the sensitivity that can be attained by an interferometer using Fisher information.

The experimental scheme proposed in this report is shown in figure 6.1. A 2n-photon dual-Fock state,$|n\rangle_{f,1}|n\rangle_{g,2}$, is used as a probe beam. This state can be expressed in terms of the creation operators $\hat{a}_1^\dagger[f] = \int d\omega f(\omega) a_1^\dagger(\omega)$ and $\hat{a}_2^\dagger[g] = \int d\omega g(\omega) a_2^\dagger(\omega)$ acting on a vacuum state $\left(\hat{a}_1^\dagger[f]\hat{a}_2^\dagger[g]\right)^n / n!|\mathbf{0}\rangle = |n\rangle_{f,1}|n\rangle_{g,2}$ where f and g label two temporal modes

in spatial modes 1 and 2 respectively. When $f = g$ the photons are indistinguishable and perfect quantum interference occurs.

To quantify distinguishability we will use the formalism found in [130]. First we will re-express g as a linear combination of f and an orthogonal temporal mode $f_\perp$. This means that photons in mode g are expressed as a superposition of distinguishable (orthogonal) and indistinguishable (parallel) components of mode f, $\hat{a}_2^\dagger[g] = \sqrt{\mathcal{I}}\hat{a}_2^\dagger[f] + \sqrt{1-\mathcal{I}}\hat{a}_2^\dagger[f_\perp]$. Where $\mathcal{I} = |\langle f, g\rangle|^2$ quantifies the distinguishability, two photons are fully distinguishable if $\mathcal{I} = 0$ and perfectly indistinguishable $\mathcal{I} = 1$. In this way we can re-write the input state as

$$|n\rangle_{f,1}|n\rangle_{g,2} = |n\rangle_{f,1}\sum_{k=0}^{n}\sqrt{\binom{n}{n-k}\mathcal{I}^{n-k}(1-\mathcal{I})^k}|n-k\rangle_{f,2}|k\rangle_{f_\perp,2}. \tag{6.1}$$

It is important to notice that type-I SPDC produces spectrally entangled photons. For the two-photon case $|\psi_2\rangle = \iint d\omega_1 d\omega_2 \Phi(\omega_1,\omega_2)a_1^\dagger(\omega_1)a_2^\dagger(\omega_2)|\mathbf{0}\rangle$. In this case we need to use a generalized measure of indistinguishability, $\mathcal{I}' = \iint d\omega_1 d\omega_2 \Phi(\omega_1,\omega_2)\overline{\Phi(\omega_2,\omega_1)}$ which reduces to $|\langle f, g\rangle|^2$ for unentangled photons i.e. $\Phi(\omega_1,\omega_2) = f(\omega_1)g(\omega_2)$ [131]. However the Fisher information of the four-photon case is not determined by a single parameter $\mathcal{I}'$. A more detailed explanation of the 4 photon case and the role of entanglement can be found on the preprint version of this work [119].

After defining the states we can then apply the operation of the interferometer acting on both temporal modes, which performs the following operation $e^{i\hat{H}\theta} = \mathbb{1} + i\theta\hat{H} + \frac{(i\theta\hat{H})^2}{2} + \mathcal{O}(\theta^4)$ with $\hat{H} = i\hat{f}_1^\dagger\hat{f}_2 + i\hat{f}_{\perp 1}^\dagger\hat{f}_{\perp 2} + \text{h.c.}$ and $\mathcal{O}$ corresponds to the higher order terms of the expansion (odd powers will cancel out). In this case the probabilities for the different detection outcomes after the interferometer are given by

$$
\begin{aligned}
P\left(n,n|\theta\right) &= 1-\frac{n+\mathcal{I}\,n^2}{2}\theta^2+\mathcal{O}(\theta^4),\\
P\left(n\pm1,n\mp1|\theta\right) &= \frac{n+\mathcal{I}\,n^2}{2}\theta^2+\mathcal{O}(\theta^4).
\end{aligned}
\tag{6.2}
$$

From the output probabilities it is possible to quantify the sensitivity of the interferometer using the boundary in precision imposed by the Cramer-Rao bound and the Fisher information F as:

$$
\begin{aligned}
F &= \sum_r \left(\frac{\partial P(r|\theta)}{\partial\theta}\right)^2 \frac{1}{P(r|\theta)}\\
&= 2(n+\mathcal{I}\,n^2)+\mathcal{O}(\theta^2),
\end{aligned}
\tag{6.3}
$$

which is the sum over terms indexed by each photon detection pattern r. From 6.3 we can compare the performance of such a state to that of a classical state which is Shot-noise-limited. A coherent's state Fisher information for a MZ interferometer is equal to $F = 2n$. So that for $\mathcal{I} \neq 0$, the sensitivity of the quantum state surpasses the Shot-noise-limit around $\theta = 0$, at this point we have highest information since there is less ambiguity of the detection outcomes. Although it has been shown that a scheme that uses Bayesian analysis and optimized adaptive feedback could compensate for non-zero θ regaining the sensitivity at $\theta = 0$ [132].

6.3 Experiment

In order to demonstrate experimentally the usefulness of states with partial distinguishability we have performed an experiment based on the scheme presented in figure 6.1. The idea is to generate the state describe by Eq. 6.1 to which we'll introduce distinguishability by temporally delaying one mode respect to the other. The experimental setup is shown in figure 6.2. We generate the state for photon pairs ($n = 1$) and bi-photon pairs

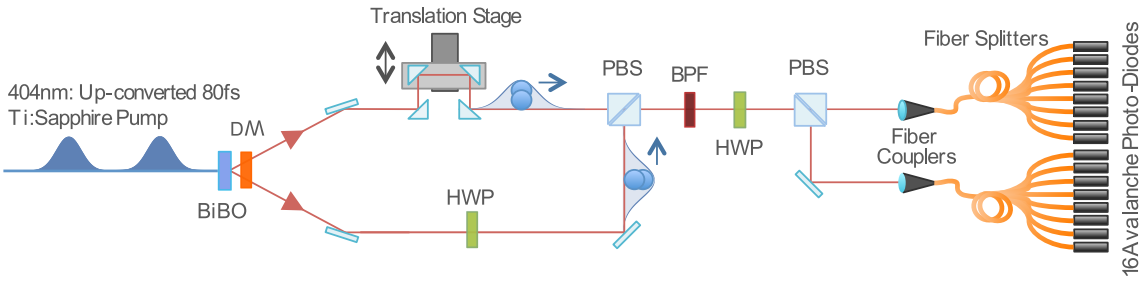

FIGURE 6.2: **Experimental Setup.** Degenerate photon pairs and bi-photon pairs are generated via non-collinear type-I (SPDC). The source is a BiBO crystal pumped with a 404 nm beam up-converted from a 85 fs titanium sapphire laser with a repetition rate of 80 mHz. Distinguishability is introduced using a linear stage that delays one spatial mode respect to the other. Photons are recombined into a single spatial mode using a half-waveplate that rotates the polarization of one mode by 90 ° and a PBS that recombines both modes. After this interference occurs in a polarization based Mach-Zehnder-like interferometer. Photons are finally detected using a spatially multiplexed pseudo-number-resolving arrangement of 16 avalanche photo-diodes as the one used in [133].

($n = 2$) via spontaneous parametric down-conversion (SPDC). To start we up-convert a titanium sapphire pulsed laser from 810 nm to 405 using a 2 mm thick bismuth borate (BiBO) crystal. The temporal width of the laser pulses are estimated to be < 160 fs after second harmonic generation (SHG). The original pulse-width outputed from the laser is 85 fs and the repetition rate is 80 mHz. The power of the SHG beam is controlled by introducing a half waveplate (HWP) and a polarizing beam splitter before up-conversion. The up-conversion efficiency is $\approx 20\%$ the attained power from this process is shown in figure 6.3.

After up-conversion we use the SHG beam to pump a second 2 mm BiBO crystal to generate photon and bi-photon pairs generated from a non-collinear type-I SPDC process. Photons are emitted into two spatial modes with horizontal polarization. One mode is delayed using a translation stage to control the temporal-mode distinguishability. The second mode is rotated to vertical polarization using a HWP set at 45 ° to then recombine both modes into a single spatial mode using a PBS. After the PBS, photons are spectrally filtered using a 3 nm bandpass filter, the spectrum of the pump and down converted photons are shown in figure 6.4. Subsequently the photons are sent into a polarization

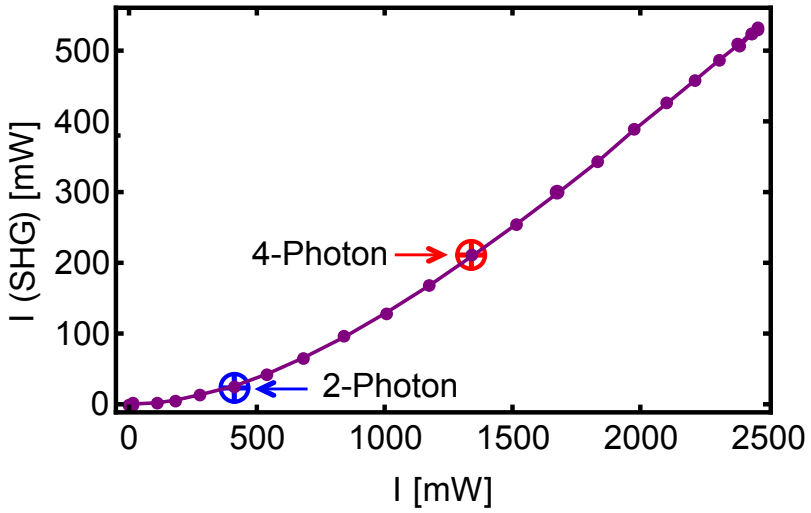

FIGURE 6.3: **Second harmonic intensity as a function of fundamental pump intensity.** The blue circle corresponds to the average power used for generating photons pairs (38 mW). The red circle correspond to the average power used to generate bi-photon pairs (200 mW). Experimental points are not fitted (the purple line is joining the points as a guide for the eye).

based Mach-Zehnder-like interferometer consisting of two PBSs and a HWP. Interference fringes are obtained by scanning the angle of the HWP.

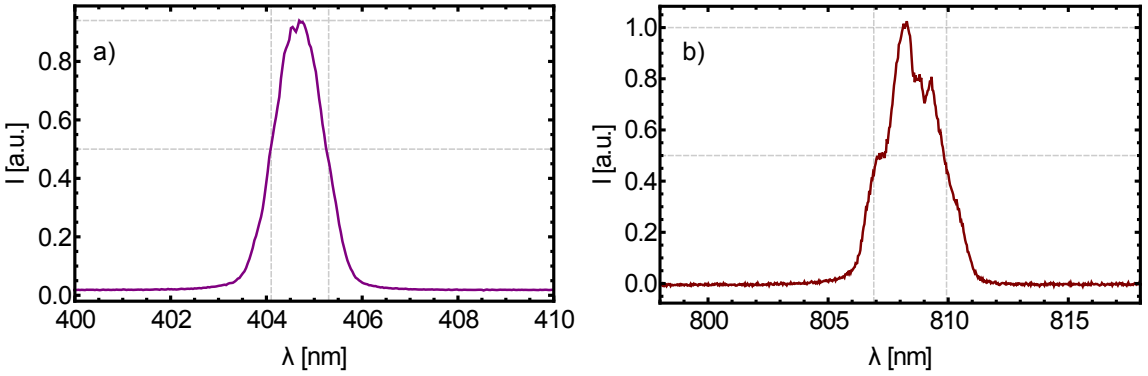

FIGURE 6.4: **Spectra.** a) Corresponds to the spectral profile of the SHG pump. b) Corresponds to the spectral profile of the down-converted photons.

The phase of the interferometer was scanned for nine different values of $\mathcal{I}'$ over the range $(0, 2\pi)$ obtaining interference fringes with different levels of visibility. In figure 6.5 we show the HOM dip as a function of the position of the translation stage and the points whithin the dip where the interference fringes were scanned. To obtain the dip we set the HWP of the interferometer to 22.5° such that the transfer matrix of the PBS acted as the one of a 50/50 beamsplitter [134]. Measurements were done using two arrays of 8 spatially

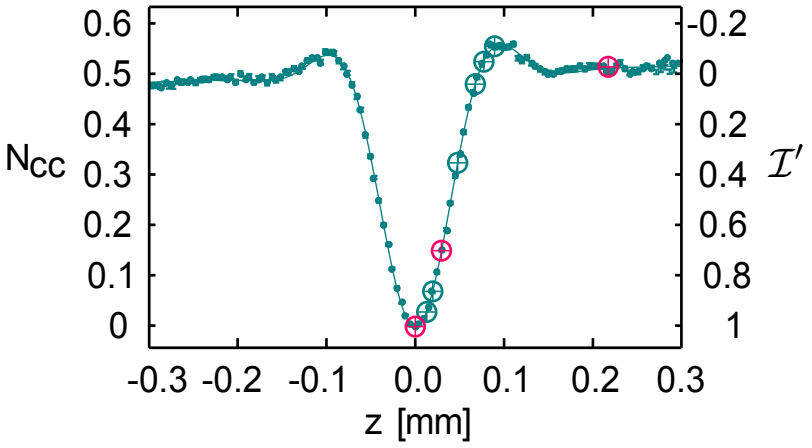

FIGURE 6.5: **Two-photon Hong-Ou-Mandel dip measured with experimental setup.** The plot shows the normalized coincidence counts between the two output ports of the interferometer as function of the position of the translation stage or alternatively described by the distinguishability parameter $\mathcal{I}'$. The circles correspond to the nine different levels of distinguishability where the experiment was performed. The three pink circles correspond to the positions for the interference fringes shown in figs. (6.6, 6.7). The dip has a visibility of ∼99%. The error bars assume that the data has a Poissonian distribution.

multiplexed APDs to perform pseudo-number resolving detection [133]. The count rates are shown in table 6.1. For the two photon case accidental coincidences had to be subtracted from the measurements. This was done by introducing random delays between the channels and recording the coincidence rate from uncorrelated photons. The contribution of accidental coincidence corresponds to 1% of the correlated photon measurements. For the four photon case the contribution of accidental corresponds to 3 % of the detected outcomes.

TABLE 6.1: **Count rates.**The label correspond to the detection outcomes: (01) is the case when there was no detection in the first channel and a single detection in the second, (11) corresponds coincidence between the two channels, (02) corresponds to a two photon coincidence in the second channel and so forth. Rates are reported in Hertz but for the two photon experiment integration time was 2 seconds and 10 seconds for the 4 photon case.

(01)	(11)	(02)	(22)	(13)	(04)
14500	1300	600	n/a	n/a	n/a
147000	2200	900	3.6	1.5	1

6.4 Results

The result shown in Figs. 6.6 and 6.7 are a post-selected from the detection events with the desired number of photons for respectively two and four photon input states. When expressing the unitary transformation of the BS in terms of sine and cosine functions we obtain the following probabilities for the two photon case:

$$\begin{aligned} p\left(|\Delta| = 1|\theta\right) &= \frac{1+\mathcal{I}'}{4}\left[1-\cos(2\theta)\right], \\ p\left(|\Delta| = 0|\theta\right) &= \frac{1}{4}\left[3-\mathcal{I}'+(1+\mathcal{I}')\cos(2\theta)\right], \end{aligned} \tag{6.4}$$

where $\Delta = n_1 - n_2$ is the difference between the number of photons detected at output modes 1 and 2.

These functions were fitted to our data by expressing them in terms of a Fourier series and letting the coefficient c to vary

$$p\left(|\Delta||\theta\right) = \sum_j c_j \cos(i\theta). \tag{6.5}$$

Before fitting we normalized the detection count rates and account for the detection inefficiencies due to the combinatoric loss of the multiplexed detection system [133] and also corrected for the background noise so that the ideal two-photon probabilities are modified to:

$$p_D\left(|\Delta||\theta\right) = p(|\Delta||\theta)(1-\chi) + \chi/2, \tag{6.6}$$

where $\chi = 1.19\%$ is the probability of observing an accidental coincidence. Using these probabilities we find that the Fisher information is maximal at a point different to $\theta = 0$. For the two-photon fringes the position with highest phase sensitivity is given by:

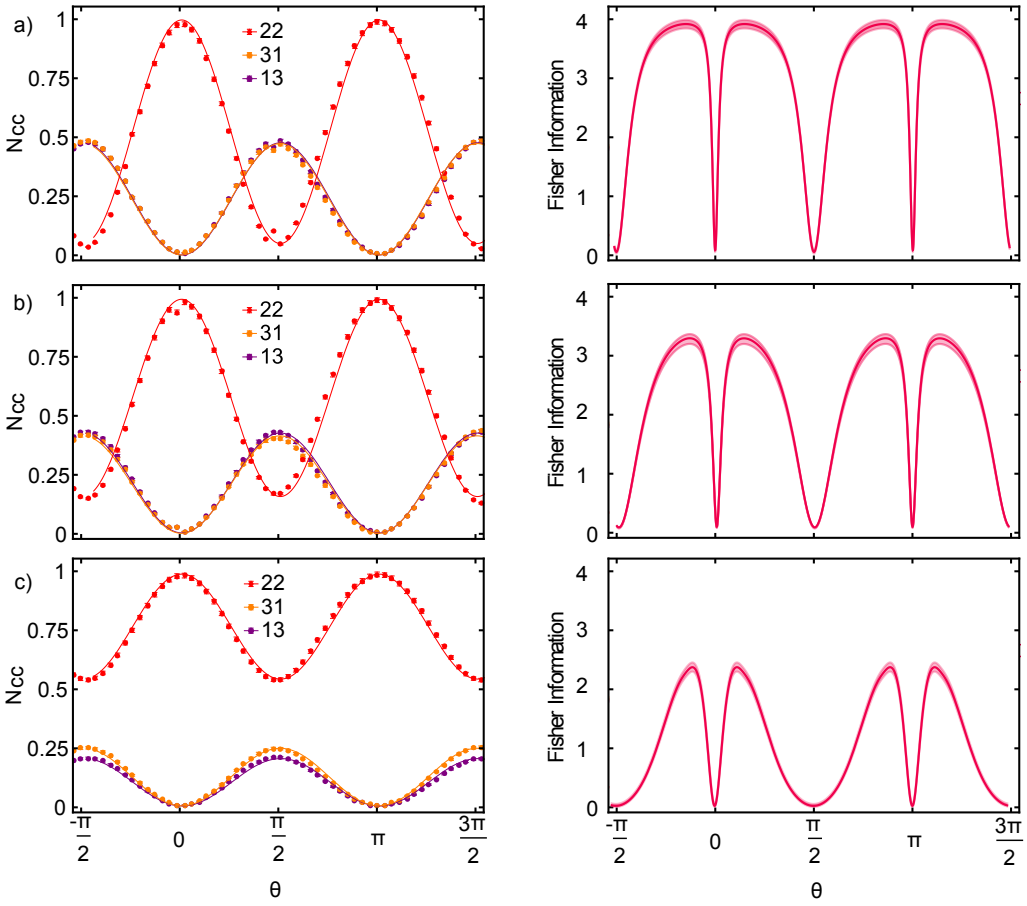

FIGURE 6.6: **Two-photon fringes and Fisher information.** The left hand side of a) b) and c) correspond to the two-photon normalized interference fringes obtained at three different points of the HOM dip (the points mentioned in 6.5) and the right hand side shows their associated Fisher information. The interference fringes in a) were scanned at the lowest point of the dip an therefore photons have the highest indistinguishability. The fringes in b) were scanned $\sim$50 μm away from the bottom of the dip and have an associated indistinguishability of $\sim$0.7, c) was taken outside the dip and have the lowest indistinguishability. The labels (11,20) correspond to the different coincidence detection outcomes, 11 is a coincidence between the two exit-ports of the interferometer, 20 is a coincidence in the transmission port of the interferometer. Error bars of the interference fringes assume a Poissonian distribution of the coincidence counts. Uncertainty of the Fisher information curves comes from a Monte-Carlo simulations of the results within the error bounds of the measurements and the fittings of the simulated fringes.The Monte-Carlo was done by generating a random Gaussian distribution of 100 points around the measured point and then fitting curves through them.

$$\theta = \left(\sqrt[4]{\frac{\chi^2 - 2\chi}{\mathcal{I}'^2(\chi-1)^2 - 1}} \right). \tag{6.7}$$

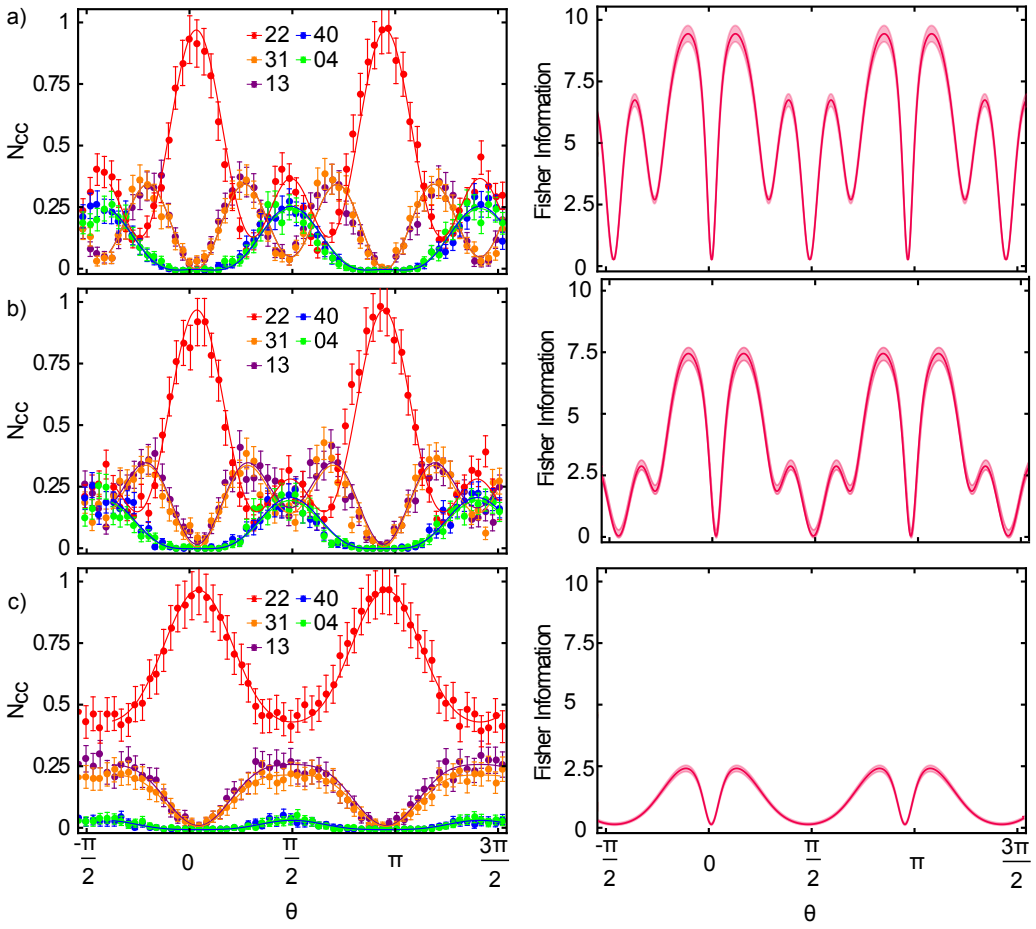

FIGURE 6.7: **Four-photon fringes and Fisher information.** The left hand side of a) b) and c) correspond to the four-photon normalized interference fringes and on the right their associated Fisher information. The fringes were scanned at the same points of the dip referenced in 6.5. The labels correspond to all the possible detection outcomes as explained in figure 6.6.

We can then calculate the optimal Fisher information at this point using Eq.6.3 and obtain an expression of it as a function of $\mathcal{I}'$

$$2 + 2\mathcal{I}'(\chi - 1)^2 + 2\sqrt{\chi(\chi - 2)[\mathcal{I}'^2(\chi - 1)^2 - 1]}, \tag{6.8}$$

inserting $\chi = 1.19\%$ into the expression. The graph in figure 6.8 shows the highest values of Fisher information at each point of the dip as a Function of $\mathcal{I}'$.

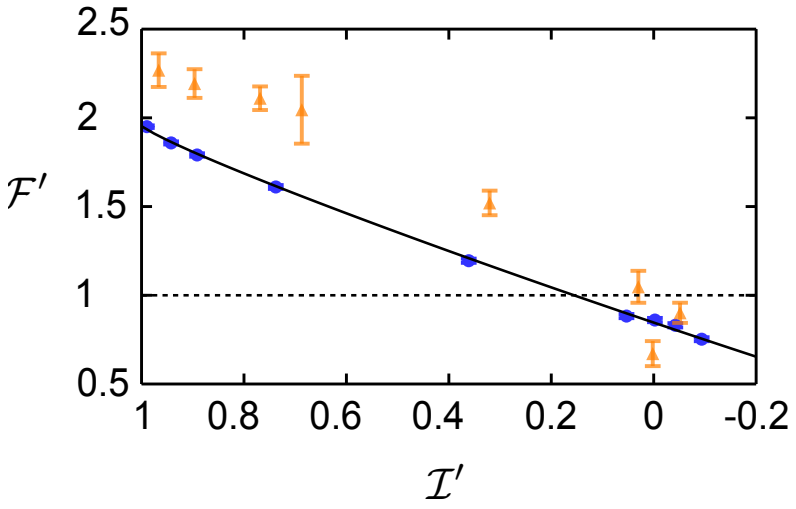

FIGURE 6.8: **Fisher information vs distinguishability.** $F' \equiv F/(2n)$. Values achieved with two photons are shown in blue and yellow for four photons. Error bars are found by Monte-Carlo simulation of experimental data.

6.5 Conclusions

In this chapter we have studied the effects of photon distinguishability for quantum enhanced phase estimation. We have analytically predicted that supra-classical performance remains with partially distinguishable photons. This was corroborated experimentally using an SPDC source of photons pumped with a femto second pulsed laser to generate multi-photons events. We interfered photonic states consisting of two and four photons controlling their temporal overlap. The experimental results show a gradual degradation of precision as distinguishability increases. In the experiment, we introduce temporal distinguishability but the analysis is valid for any other type of distinguishability. We conclude that sources of low-indistinguishable photons like NV centers, atomic sources or quantum dots can be significantly simplified since complete photon indistinguishability is not required to achieve a quantum advantage in metrological schemes similar to the one presented here. We also think that this work is beneficial for experiments where it is desired to combine two or more spontaneous sources to obtain multi-photon events, although further work has to be done to implement a model that would account for entanglement with higher order terms.

Chapter 7

Conclusions

7.1 Conclusions and Outlook

Throughout this thesis we have presented strategies to overcome practical limitations of quantum enhanced optical measurement schemes. We have mainly centered our attention in reducing the loss to improve the estimate of light flux through a sample in quantum enhanced transmission estimation protocols using twin beam sources. One of the motivations behind this work is to engineer sources of light capable of probing delicate photosensitive samples without inflicting damage. We have successfully shown that our source is capable to outperform classical sources of light in a per-probe-photon basis when measuring transmission. However, both the photon energy (∼810 nm) and the intensity (∼10 fW) of our source are far below the damage threshold for many applications, in such circumstances it would be more advantageous to increase the intensity of a classical source to improve the signal to noise ratio. Taking this into consideration we conclude that our efforts should now be set in two different fronts.

One, is to engineer a source that can compete with bright coherent laser light. For this we have to address both of the aforementioned problems; increase the energy of the emitted photons and increase the intensity of the source. In chapter 5 we discuss how feed-forward may be implemented with bright SPDC light following the method shown in Ref. [87]. But

much more effort has to be devoted to generating down-converted photons at lower wavelengths. There have been demonstrations of down-conversion in the x-ray spectrum [135] but the intensities are still too low. An alternative to spontaneous sources that can reach lower wavelengths might be quantum dots which have been demonstrated to emit in the UV spectrum [77], if collection efficiency at this wavelengths can be improved they might become a suitable source of single-photon UV light for biophotonic applications.

The second front where we need to focus our attention is on the quest to find appropriate applications and samples that are compatible with the specifications of our source, those which require a probe at the single-photon level.

Calibration of single-photon detectors is perhaps one of the most obvious applications. Ever since the first experimental demonstrations of SPDC it has been suggested that twin beams can be used as a tool to perform absolute measurements of detector quantum efficiency [136–138]. Our source, in combination with the imaging system described in chapter 5 could be used to perform detector calibration with spatial resolution.

Another important application is the study of the response of optic nerve cells when excited with single-photons. This is a very active field of research [64, 139–141] in particular, there is growing interest addressing the question: Can the human eye detect single-photons [74, 142, 143]? For this, we would need to generate photons near 555 nm, where the human eye has peak sensitivity. The design of our source can be modified to generate photons in the green spectrum, this has already been done using PPKTP [81], so our source would require a crystal phase-matched for these wavelengths and other minor alterations like changing the pump beam and anti-reflection coatings.

As well, we believe that our source or designs similar to ours could play an important role for experiments of molecules probed with quantum light [144]. A specific example for these type of experiments is the validation of a fully quantum mechanical understanding of the transduction of energy from sunlight to electron-hole pairs in photosynthetic complexes. A recent publication has set to understand the microscopic dynamics of absorption of individual photons by chromophores in light-harvesting complexes [145] and suggests

experimental work involving single-photon absorption measurements that are compatible with the capabilities of our source.

Finally we conclude that in analogy to the advent of laser light, single photon sources are a tool awaiting for an application. Therefore we foresee a future where multiple fields of science and technology will benefit from further developments.

Appendix A

Absolute quantum advantage in transmission measurement

This appendix is based on the manuscript: *Demonstrating an absolute quantum advantage in direct absorption measurement* by Paul-Antoine Moreau, Javier Sabines-Chesterking, Rebecca Whittaker, Siddarth K. Joshi, Patrick M. Birchall, Alex McMillan, John G. Rarity and Jonathan C. F. Matthews, Scientific Reports volume 7, Article number: 6256 (2017) [84].

Statement of Work: Jonathan Matthews, Paul-Antoine Moreau and John Rarity conceived and designed the experiment. I conducted the experiment with Paul-Antoine Moreau. Siddarth Joshi and Rebecca Whittaker built the source which I then aligned and optimized. The software for data acquisition was written by Paul-Antoine Moreau. The transmission estimator and the data analysis were also proposed and conducted by Paul-Antoine Moreau. This work was performed under the supervision Jonathan C. F. Matthews and John Rarity. All authors contributed to the published manuscript.

Advances in photodetctor technology have played a critical role in experiments and technologies that demonstrate a departure from classical behaviour in the field of optics. An example is how near-unity efficient detectors, like transition-edge sensors, have enabled loophole-free Bell tests that do not require the fair sampling assumption [97, 98]. Analogously to overcoming the fair-sampling assumption in Bell-test experiments, absolute demonstrations of sub-Shot-noise measurements should strictly avoid post-selection. By a strict avoidance of post-selection we mean not only accounting for negative experimental outcomes (e.g. accounting for false coincidences) but also accounting for detector inefficiencies. For example, photons that interact with the sample but are unaccounted for the estimator due to inefficient detection. In this sense absolute sub-Shot noise performance is only guaranteed when the noise of a measurement protocol using a quantum state of light is smaller to a equivalent classical protocol. This is a noiseless laser measured with a 100% efficient detector and a sample exposed with the same intensity, i.e, an absolute advantage per photon utilized[1]. Absolute sub-Shot-noise performance has been observed multiple times using squeezed states of light measured with homodyne detectors which have near unity efficiency [147–150]. However, such techniques may require prior knowledge of the sample under investigation, they work over narrow bandwidths and cannot directly achieve the theoretical maximal sensitivity per resource.

Here we present what to our knowledge is the first absolute measurement of absolute-sub-Shot noise performance using discrete variables[2]. We use a highly efficient photon-pair source and employ a low-noise, high efficiency CCD camera (90%) to demonstrate an absolute quantum advantage in an optical transmission measurement.

A common procedure to reduce the noise of an optical measurement is by performing a differential measure of intensity. In a differential measurement, a beam is split into two paths, a probe beam and a reference beam. The first interacts with the samples and the second does not, so that the intensity fluctuations of the reference beam are independent

[1] We avoid comparison to classical protocols that employ a multipass schemes. In Ref. [146] there is a clear comparison between the limits of classical multipass schemes and quantum schemes.

[2] After submitting an e-print of this work on the arxiv and before its final publication in *Scientific Reports* [84], there have been two other reports of an absolute advantage, one in wide field transmission imaging [83] and the second is in phase estimation [82]

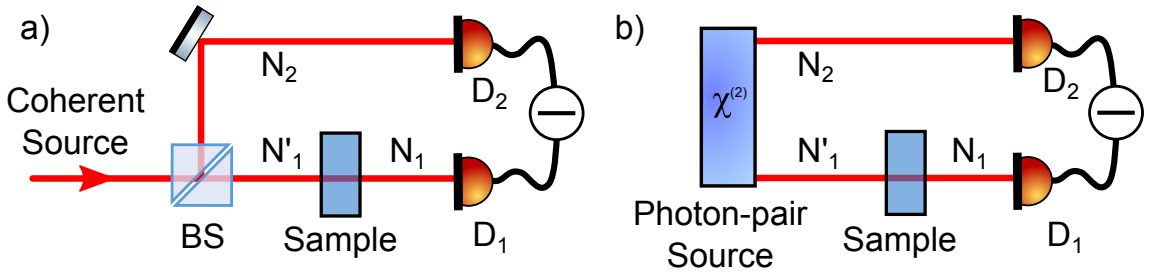

FIGURE A.1: **Transmission measurement schemes.** a)Classical differential measurement. Classical fluctuations are monitored and suppressed using a reference beam. b) Correlated beam measurement. Classical and quantum fluctuations are suppressed due to strong intensity correlations.

from the sample. This is illustrated in figure A.1 a). By subtracting the detected intensities of the two beams one can eliminate the classical noise contained in the original beam before the beam splitter and hence improving the signal-to-noise ratio (SNR) of the measurement. However, if the original beam does not contain any classical noise (power fluctuations of the laser, mechanical inestabilities, beam wondering, etc.), this scheme would only worsen the SNR as it would double the quantum fluctuations set by the Shot-noise-limit (SNL) [83]. A way of eliminating quantum fluctuations is by using correlated twin-beams generated with spontaneous parametric down-conversion (SPDC) [66] which have stronger photon number correlations than a coherent beam split into two channels, as depicted in figure A.1 b).

Given two beams separated in two channels 1 and 2 with photon number distribution N_1 and N_2 respectively we can estimate the degree of correlation between them, σ, as the ratio of the variance of the photon number difference $\Delta^2(N_1 - N_2)$ and the sum of the mean photon number $\langle N_1 \rangle + \langle N_2 \rangle$

$$\sigma = \frac{\Delta^2(N_1 - N_2)}{\langle N_1 \rangle + \langle N_2 \rangle}. \tag{A.1}$$

The value of σ is equal to 1 for a noiseless coherent state, it can be less than unity for SPDC twin beams, and in the ideal case of perfect correlations the value goes to zero. When the losses in both channels are symmetric σ can be related to the transmission of

the system, η, by $\sigma = 1 - \eta$. This estimator is useful when the detection scheme can only measure intensities and cannot perform coincidence based measurements, so that a Klyshko transmission estimate like the one used in [46, 67, 68] is not accessible.

In a classical direct measurement we can estimate the transmission as the ratio of the average number of photons before, N_1', and after the sample, N_1.

$$\eta_s = \frac{N_1}{\langle N_1' \rangle}. \tag{A.2}$$

Assuming $\langle N_1' \rangle$ is well calibrated and that the probe beam is a coherent state, then the precision of this measurement will be limited by fluctuations of N_1, i.e. the Shot-noise limit. However, when we use SPDC light to probe the sample as in figure A.1 b) we know that the fluctuation in the number of photons of the two output modes of the crystal, N_1, and , N_2, are correlated. Noise measured on N_1 can be suppressed using the knowledge gained by measuring N_2. Nevertheless, loss in either of the modes deteriorates the correlations and allows for uncorrelated single photons to be present in the experiment. Therefore, to maximize information per-photon exposure (PPE), we have developed a new, unbiased estimator that uses all detected photons that pass through a sample to estimate its absorption with quantum-enhanced noise-suppression PPE. This estimator is given by

$$\eta = \frac{\mathcal{N} + \delta E}{\langle N_1' \rangle} = \frac{N_1 - k\delta N_2 + \delta E}{\langle N_1' \rangle}, \tag{A.3}$$

where $\mathcal{N}$ is a corrected estimate for N_1 dependent on δN_2, the deviation of N_2 from its mean value $\langle N_2 \rangle$; δE, which corrects for any bias on the estimator, calibrated by taking images without a sample; and $k = CN_1$, a correction factor that encapsulates the sources of noise in our photon source obtained during the calibration phase. A full derivation of this estimator can be found in the supplementary material of [84].

A.1 Experimental Setup

The source used to generate correlated light in this experiment is the same as the one reported in 3. The experimental setup is presented in figure A.2. A periodically poled potassium titanyl phosphate (PPKTP) crystal phase matched for type-II SPDC is pumped using a 404 nm continuous wave (CW) laser. The crystal is set in an oven in order to tune the phase matching conditions. The down-converted photons are emitted at 798 nm for channel 1 (signal) and 818 nm for channel 2 (idler). The lower wavelength was chosen as a probe since it is closer to the maximum detection efficiency of the camera. The generated photon pairs are filtered using a long pass and a band pass filter and then deterministically separated using a polarizing beam splitter (PBS). After separated, the signal and idler photons are coupled into single mode fibers. Subsequently one beam is focused directly onto a CCD camera while the other goes through a sample composed of a half-wave plate (HWP) and a PBS before being detected at a different region of the CCD. The camera we used is an Andor iDus 416 cooled to -35° C. The quantum efficiency of the camera at this temperature is 90 ±3%. The transmissivity of the system was characterized first and then the absorptive sample was introduced. By rotating the HWP we recorded a plot of the performance of the system under different transmission conditions, as discussed below.

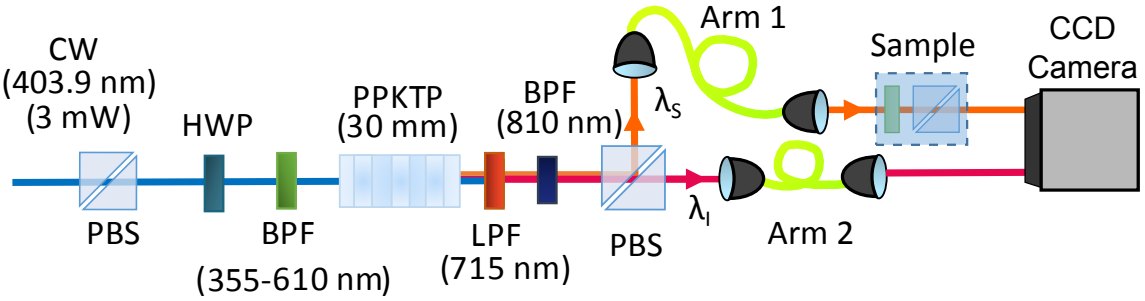

FIGURE A.2: **Experimental setup.** A 404 nm (Toptica TopMode) laser pumps a 30 mm PPKTP crystal generating correlated photon-pairs via type-II SPDC. After being separated with a PBS photons are collected using single mode fibers. A sample is set at the output of one of the arms before being focused onto a CCD camera. The other arm is directly focused onto a different region of the camera.

A.2 Results

The CCD camera used in this experiment (Andor iDus 416) is designed to perform spectroscopic measurements, where the second dimension of spatial information of the detected light is not required so the camera has a smaller readout noise when the photocurrent is binned in vertical columns of pixels. In this case for each data acquisition we obtain a plot of the vertically binned pixels vs. number of photon counts as the one shown in figure A.3. Each plots contains two peaks corresponding to the two down-converted beams. After obtaining a series of counts we can determine the region of interest from which we integrate the photocurrent to determine the number photons as seen in figure A.3 in each arm.

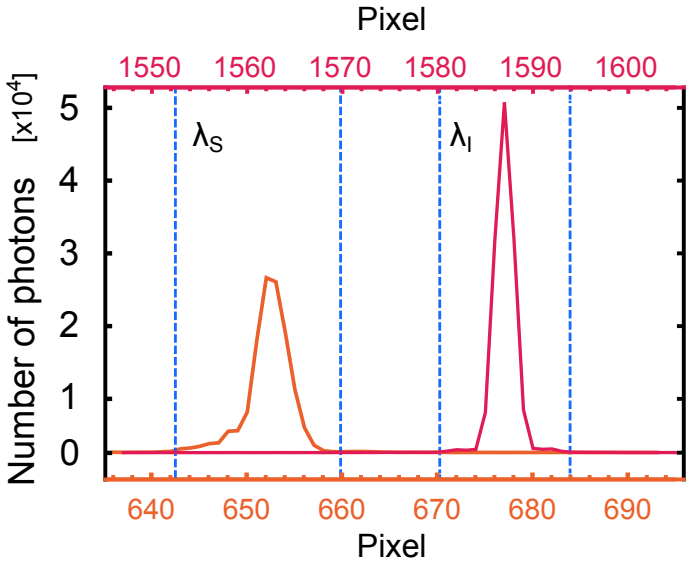

FIGURE A.3: **CCD data acquisition.** The camera is set to bin vertically the detected photo-current outputting a graph like the one presented in this figure for every acquisition. In orange we observe the counts corresponding to arm 1 (signal) and in pink the counts corresponding to arm 2 (idler). The blue lines correspond to the region of integration for each arm.

We first characterized the performance of the setup without the sample, obtaining a σ parameter equal to 0.38 $\pm$0.02. This guarantees sub-Shot noise behaviour. This value corresponds to a Klyshko efficiency of 62%. With values of σ below one, it is possible to perform transmission measurements that have an advantage over differential classical

scheme and with values below 0.5 an advantage over a direct classical scheme. We estimated σ with 10 series of measurements each with 100 acquisitions with an integration time of 0.5 s. The mean photon rate without the sample was 200 kHz. The data output of the camera is in gray scale level that has to be converted into number of photons through the relation $N = S(E_s - E_{Off})$ where N is the number of photons, E_s is the intensity signal in grey scale level, E_{Off} is an electronic offset obtained when no light is illuminating the sensor and S=0.71 photo-electrons per grey level is the sensitivity of the camera.

After characterization we repeated the same measurement process for each value of transmission (10 series with 100 acquisitions) estimating η using Eq. A.3. After obtaining all measurements we estimate the precision ratio, Γ, in which we account for detector efficiency and normalize to a per-photon exposure basis, between the scheme presented here, (η_{exp}) and an ideal coherent scheme η_{coh}

$$\Gamma = \frac{\Delta^2 \eta_{\mathrm{coh}}}{\Delta^2 \eta_{\mathrm{exp}}}. \tag{A.4}$$

Our results are presented in figure A.4. The maximum precision ratio we obtained was 1.46 $\pm$0.06 at a transmissivity of η=0.99 when compared to an ideal direct coherent state measurement with a 100% efficient detector. This translates into a factor of 1.63 $\pm$0.06 over a direct coherent measurement using the same detector efficiency (90%).

A.3 Conclusions

To conclude, we have demonstrated an absolute quantum advantage over the best classical optical strategy for direct transmission measurement over the range 0.5$<\eta<$1. This demonstrates that quantum-enhanced transmission measurements need not be confined to measuring highly transmisive samples. Furthermore, sub-Shot noise measurements with correlated intensities can be more practical since they are not limited to a low photon flux as are coincidence based measurements due to saturation at low intensities. The relative

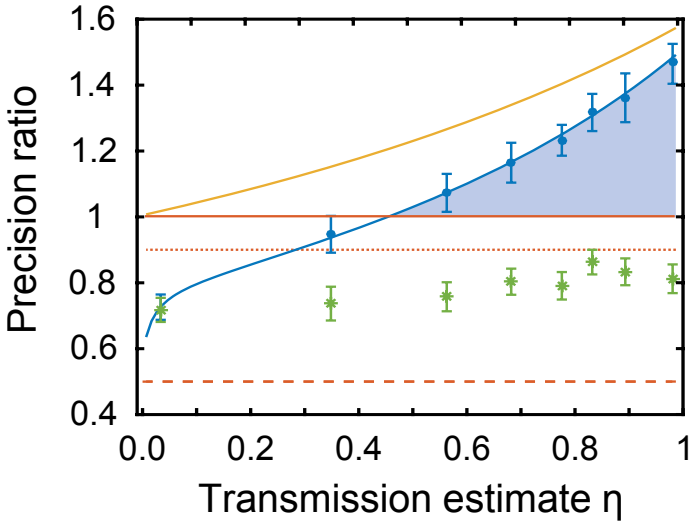

FIGURE A.4: **Absolute precision ratio in optical transmission measurement.** The plot shows the ratio between the variance of a classical transmission estimate for an ideal coherent scheme and our experimental measurements (curves and data are normalized to PPE). The red solid line corresponds to the ideal classical limit. The red dotted line corresponds to a noiseless classical beam detected with a 90% efficient detector (same efficiency as in our setup). The red dashed line corresponds to an ideal classical differential scheme. Blue points are our experimental results using correlations between both beams. Green asterisks correspond to measurements using a single beam. The blue shadow area corresponds to a region with an absolute quantum advantage. The blue line is a fit of the estimator.

simplicity of the scheme presented here can motivate analogous setups applied to high-energy optics, for example, the demonstrations of X-ray parametric down-conversion [135, 151] and the development of high efficiency direct hard X-ray detector arrays could be used to minimize radiation exposure in medical imaging.

Bibliography

[1] C. M. Caves, "Quantum-mechanical noise in an interferometer," *Phys. Rev. D*, vol. 23, pp. 1693–1708, Apr 1981.

[2] V. Giovannetti, S. Lloyd, L. Maccone, and J. H. Shapiro, "Sub-rayleigh-diffraction-bound quantum imaging," *Physical Review A*, vol. 79, no. 1, p. 013827, 2009.

[3] R. Demkowicz-Dobrzański, M. Jarzyna, and J. Kołodyński, "Chapter four-quantum limits in optical interferometry," *Progress in Optics*, vol. 60, pp. 345–435, 2015.

[4] P. Kok and B. W. Lovett, *Introduction to optical quantum information processing*. Cambridge University Press, 2010.

[5] Z. H. Shamsi, D. Kim, and Y. Kwon, "Quantum fisher information of fermionic cavity modes in an accelerated motion," *arXiv preprint arXiv:1409.6847*, 2014.

[6] S. L. Braunstein and C. M. Caves, "Statistical distance and the geometry of quantum states," *Physical Review Letters*, vol. 72, no. 22, p. 3439, 1994.

[7] M. Tsang, R. Nair, and X.-M. Lu, "Quantum theory of superresolution for two incoherent optical point sources," *Physical Review X*, vol. 6, no. 3, p. 031033, 2016.

[8] F. Yang, R. Nair, M. Tsang, C. Simon, and A. I. Lvovsky, "Fisher information for far-field linear optical superresolution via homodyne or heterodyne detection in a higher-order local oscillator mode," *Physical Review A*, vol. 96, no. 6, p. 063829, 2017.

[9] L. Mandel and E. Wolf, *Optical coherence and quantum optics*. Cambridge university press, 1995.

[10] G. Adesso, F. Dell'Anno, S. De Siena, F. Illuminati, and L. A. M. Souza *Phys. Rev. A*, vol. 79, p. 040305R, 2009.

[11] D. Stoler, B. Saleh, and M. Teich, "Binomial states of the quantized radiation field," *Journal of Modern Optics*, vol. 32, no. 3, pp. 345–355, 1985.

[12] A. Vidiella-Barranco and J. Roversi, "Statistical and phase properties of the binomial states of the electromagnetic field," *Physical Review A*, vol. 50, no. 6, p. 5233, 1994.

[13] J. P. Dowling, "Quantum optical metrology–the lowdown on high-n00n states," *Contemporary physics*, vol. 49, no. 2, pp. 125–143, 2008.

[14] M. Holland and K. Burnett, "Interferometric detection of optical phase shifts at the heisenberg limit," *Physical review letters*, vol. 71, no. 9, p. 1355, 1993.

[15] R.-B. Jin, M. Fujiwara, R. Shimizu, R. J. Collins, G. S. Buller, T. Yamashita, S. Miki, H. Terai, M. Takeoka, and M. Sasaki, "Detection-dependent six-photon holland-burnett state interference," *Scientific reports*, vol. 6, 2016.

[16] G. Xiang, H. Hofmann, and G. J. Pryde, "Optimal multi-photon phase sensing with a single interference fringe," *Scientific reports*, vol. 3, p. 2684, 2013.

[17] M. Eisaman, J. Fan, A. Migdall, and S. V. Polyakov, "Invited review article: Single-photon sources and detectors," *Review of scientific instruments*, vol. 82, no. 7, p. 071101, 2011.

[18] C. Hong and L. Mandel, "Theory of parametric frequency down conversion of light," *Physical Review A*, vol. 31, no. 4, p. 2409, 1985.

[19] Z.-Y. J. Ou, "Quantum state from parametric down-conversion," in *Multi-Photon Quantum Interference*, pp. 17–41, Springer, 2007.

[20] S. Castelletto and R. Scholten, "Heralded single photon sources: a route towards quantum communication technology and photon standards," *The European Physical Journal-Applied Physics*, vol. 41, no. 3, pp. 181–194, 2008.

[21] T. Pittman, B. Jacobs, and J. Franson, "Demonstration of feed-forward control for linear optics quantum computation," *Physical Review A*, vol. 66, no. 5, p. 052305, 2002.

[22] H. Cable and J. P. Dowling, "Efficient generation of large number-path entanglement using only linear optics and feed-forward," *Physical review letters*, vol. 99, no. 16, p. 163604, 2007.

[23] A. Yariv and P. Yeh, *Optical waves in crystals*, vol. 10. Wiley, New York, 1984.

[24] R. Weis and T. Gaylord, "Lithium niobate: summary of physical properties and crystal structure," *Applied Physics A: Materials Science & Processing*, vol. 37, no. 4, pp. 191–203, 1985.

[25] C. C. Davis, *Lasers and electro-optics: fundamentals and engineering*. Cambridge university press, 2014.

[26] D. Fukuda, G. Fujii, T. Numata, K. Amemiya, A. Yoshizawa, H. Tsuchida, H. Fujino, H. Ishii, T. Itatani, S. Inoue, *et al.*, "Titanium-based transition-edge photon number resolving detector with 98% detection efficiency with index-matched small-gap fiber coupling," *Optics express*, vol. 19, no. 2, pp. 870–875, 2011.

[27] F. Marsili, V. B. Verma, J. A. Stern, S. Harrington, A. E. Lita, T. Gerrits, I. Vayshenker, B. Baek, M. D. Shaw, R. P. Mirin, *et al.*, "Detecting single infrared photons with 93% system efficiency," *Nature Photonics*, vol. 7, no. 3, pp. 210–214, 2013.

[28] G. Brida, M. Genovese, and I. Rou Berchera, "Experimental realization of sub-shot-noise quantum imaging," *Nature Photon.*, vol. 4, p. 227, 2010.

[29] L. Ma, O. Slattery, and X. Tang, "Single photon frequency up-conversion and its applications," *Physics Reports*, vol. 521, no. 2, pp. 69–94, 2012.

[30] M. Bass, C. DeCusatis, J. Enoch, V. Lakshminarayanan, G. Li, C. Macdonald, V. Mahajan, and E. Van Stryland, *Handbook of optics, Volume II: Design, fabrication and testing, sources and detectors, radiometry and photometry.* McGraw-Hill, Inc., 2009.

[31] H. Earl, "Guide to detector selection," January 2018.

[32] E. F. Zalewski and C. R. Duda, "Silicon photodiode device with 100% external quantum efficiency," *Applied optics*, vol. 22, no. 18, pp. 2867–2873, 1983.

[33] 2015, *Single Photon Counting Module Datasheet*, vol. 1. Excelitas Technologies, 2015.

[34] H. Paul, P. Törmä, T. Kiss, and I. Jex, "Photon chopping: New way to measure the quantum state of light," *Physical review letters*, vol. 76, no. 14, p. 2464, 1996.

[35] D. Achilles, C. Silberhorn, C. Sliwa, K. Banaszek, I. A. Walmsley, M. J. Fitch, B. C. Jacobs, T. B. Pittman, and J. D. Franson, "Photon-number-resolving detection using time-multiplexing," *Journal of Modern Optics*, vol. 51, no. 9-10, pp. 1499–1515, 2004.

[36] C. Silberhorn, "Detecting quantum light," *Contemporary Physics*, vol. 48, no. 3, pp. 143–156, 2007.

[37] S. M. van den Wildenberg, B. Prevo, and E. J. Peterman, "A brief introduction to single-molecule fluorescence methods," in *Single Molecule Analysis*, pp. 93–113, Springer, 2018.

[38] R. Roy, S. Hohng, and T. Ha, "A practical guide to single-molecule fret," *Nature methods*, vol. 5, no. 6, pp. 507–516, 2008.

[39] S. C. Denson, C. J. Pommier, and M. B. Denton, "The impact of array detectors on raman spectroscopy," 2007.

[40] J. Tyson, "Progress in low-light-level charge-coupled device imaging in astronomy," *JOSA A*, vol. 7, no. 7, pp. 1231–1236, 1990.

[41] A. Tarun, "Types of charge-coupled devices with their working principles," January 2018.

[42] K. R. Spring, T. J. Fellers, and M. W. Davidson, "Introduction to charge-coupled devices (ccds)," January 2018.

[43] Andor, "Sensitivity of ccd cameras," January 2018. Available at `http://www.andor.com/learning-academy/sensitivity-of-ccd-cameras-key-factors-to-consider`.

[44] Andor, "Sensitivity," January 2018. Available at `http://www.andor.com/learning-academy/sensitivity-making-sense-of-sensitivity`.

[45] Andor, "Andor idus 420 specifications," January 2018. Available at `http://www.andor.com/pdfs/specifications/Andor_iDus_420_Specifications.pdf`.

[46] J. Sabines-Chesterking, R. Whittaker, S. Joshi, P. Birchall, P. Moreau, A. McMillan, H. Cable, J. O'Brien, J. Rarity, and J. Matthews, "Sub-shot-noise transmission measurement enabled by active feed-forward of heralded single photons," *Physical Review Applied*, vol. 8, no. 1, p. 014016, 2017.

[47] C. Gardiner and P. Zoller, *Quantum noise: a handbook of Markovian and non-Markovian quantum stochastic methods with applications to quantum optics*, vol. 56. Springer Science & Business Media, 2004.

[48] R. Schnabel, N. Mavalvala, D. E. McClelland, and P. K. Lam, "Quantum metrology for gravitational wave astronomy," *Nature communications*, vol. 1, p. 121, 2010.

[49] V. Giovannetti, S. Lloyd, and L. maccone, "Advances in quanutm metrology," *Nature Photon.*, vol. 5, pp. 222–229, 2011.

[50] N. Thomas-Peter, B. J. Smith, A. Datta, L. Zhang, U. Dorner, and I. A. Walmsley, "Real-world quantum sensors: evaluating resources for precision measurement," *Phys. Rev. Lett.*, vol. 107, no. 11, p. 113603, 2011.

[51] J. L. O'Brien, A. Furusawa, and J. Vuckovic, "Photonic quantum technologies," *Nature Photon*, vol. 3, pp. 687–695, 2009.

[52] N. Thomas-Peter, B. J. Smith, A. Datta, L. Zhang, U. Dorner, and I. A. Walmsley, "Real-world quantum sensors: Evaluating resources for precision measurement," *Phys. Rev. Lett.*, vol. 107, p. 113603, 2011.

[53] E. Jakeman and J. G. Rarity *Opt. Comm.*, vol. 59, p. 219, 1986.

[54] H. Cable and J. P. Dowling, "Efficient generation of large number-path entanglement using only linear optics and feed-forward," *Phys. Rev. Lett.*, vol. 99, p. 163604, 2007.

[55] K. T. McCusker and P. G. Kwiat, "Efficient optical quantum state engineering," *Phys. Rev. Lett.*, vol. 103, no. 16, p. 163602, 2009.

[56] R. Prevedel, P. Walther, F. Tiefenbacher, P. Böhi, R. Kaltenbaek, T. Jennewein, and A. Zeilinger, "High-speed linear optics quantum computing using active feed-forward," *Nature*, vol. 445, no. 7123, pp. 65–69, 2007.

[57] X.-s. Ma, S. Zotter, J. Kofler, T. Jennewein, and A. Zeilinger, "Experimental generation of single photons via active multiplexing," *Phys. Rev. A*, vol. 83, no. 4, p. 043814, 2011.

[58] M. J. Collins, C. Xiong, I. H. Rey, T. D. Vo, J. He, S. Shahnia, C. Reardon, T. F. Krauss, M. Steel, A. S. Clark, *et al.*, "Integrated spatial multiplexing of heralded single-photon sources," *Nature Commun.*, vol. 4, 2013.

[59] F. Kanadea, B. G. Christensen, J. J. Wong, H. S. Park, K. T. McCusker, and P. G. Kwiat, "Time-multiplexed heralded single-photon source," *Optica*, vol. 2, pp. 1010–1013, 2016.

[60] G. J. Mendoza, R. Santagati, J. Munns, E. Hemsley, M. Piekarek, E. Martín-López, G. D. Marshall, D. Bonneau, M. G. Thompson, and J. L. O'Brien, "Active temporal and spatial multiplexing of photons," *Optica*, vol. 3, no. 2, pp. 127–132, 2016.

[61] R. J. A. Francis-Jones, R. A. Hoggarth, and P. J. Mosley, "All-fubre multiplexed source of high-purity heralded single photons," *arxiv:1603.06260*.

[62] G. Brida, I. Degiovanni, M. Genovese, F. Piacentini, P. Traina, A. Della Frera, A. Tosi, A. B. Shehata, C. Scarcella, A. Gulinatti, *et al.*, "An extremely low-noise heralded single-photon source: A breakthrough for quantum technologies," *Applied Physics Letters*, vol. 101, no. 22, p. 221112, 2012.

[63] G. Brida, M. Genovese, and M. Gramegna, "Twin-photon techniques for photodetector calibration," *Laser Physics Letters*, vol. 3, no. 3, p. 115, 2006.

[64] N. M. Phan, M. F. Cheng, D. A. Bessarab, and L. A. Krivitsky, "Interaction of fixed number of photons with retinal rod cells," *Phys. Rev. Lett.*, vol. 112, no. 21, p. 213601, 2014.

[65] A. Heidmann, R. Horowicz, S. Reynaud, E. Giacobino, C. Fabre, and G. Camy, "Observation of quantum noise reduction on twin laser beams," *Physical review letters*, vol. 59, no. 22, p. 2555, 1987.

[66] J. Rarity, P. Tapster, and E. Jakeman, "Observation of sub-poissonian light in parametric downconversion," *Optics Commun.*, vol. 62, no. 3, pp. 201–206, 1987.

[67] D. Klyshko, "Use of two-photon light for absolute calibration of photoelectric detectors," *Quantum Electronics*, vol. 10, no. 9, pp. 1112–1117, 1980.

[68] R. Whittaker, C. Erven, A. Neville, M. Berry, J. O'Brien, H. Cable, and J. Matthews, "Absorption spectroscopy at the ultimate quantum limit from single-photon states," *New Journal of Physics*, vol. 19, no. 2, p. 023013, 2017.

[69] T. T. Ng, D. Gosal, A. Lamas-Linares, and C. Kurtsiefer, "Sagnac-loop phase shifter with polarization-independent operation," *Review of Scientific Instruments*, vol. 82, no. 1, p. 013106, 2011.

[70] M. Beck, "Comparing measurements of g (2)(0) performed with different coincidence detection techniques," *JOSA B*, vol. 24, no. 12, pp. 2972–2978, 2007.

[71] Y. Chen, M. Zopf, R. Keil, F. Ding, and O. G. Schmidt, "Highly-efficient extraction of entangled photons from quantum dots using a broadband optical antenna," *Nature Communications*, vol. 9, no. 1, p. 2994, 2018.

[72] P.-A. Moreau, J. Sabines-Chesterking, R. Whittaker, S. K. Joshi, A. McMillan, J. G. Rarity, and J. C. F. Matthews *In preperation.*

[73] F. Wolfgramm, C. Vitelli, F. A. Beduini, N. Godbout, and M. W. Mitchell, "Entanglement-enhanced probing of a delicate material system," *Nature Photon.*, vol. 7, pp. 28–32, 2013.

[74] J. N. Tinsley, M. I. Molodtsov, R. Prevedel, D. Wartmann, J. Espigulé-Pons, M. Lauwers, and A. Vaziri, "Direct detection of a single photon by humans," *Nature Commun.*, vol. 7, 2016.

[75] T. B. Hoang, G. M. Akselrod, and M. H. Mikkelsen, "Ultrafast room-temperature single photon emission from quantum dots coupled to plasmonic nanocavities," *Nano letters*, vol. 16, no. 1, pp. 270–275, 2015.

[76] X. Ding, Y. He, Z.-C. Duan, N. Gregersen, M.-C. Chen, S. Unsleber, S. Maier, C. Schneider, M. Kamp, S. Höfling, *et al.*, "On-demand single photons with high extraction efficiency and near-unity indistinguishability from a resonantly driven quantum dot in a micropillar," *Phys. Rev. Lett.*, vol. 116, no. 2, p. 020401, 2016.

[77] J.-H. Kim, Y.-H. Ko, S.-H. Gong, S.-M. Ko, and Y.-H. Cho, "Ultrafast single photon emitting quantum photonic structures based on a nano-obelisk," *Scientific reports*, vol. 3, 2013.

[78] S. Ramelow, A. Mech, M. Giustina, S. Gröblacher, W. Wieczorek, J. Beyer, A. Lita, B. Calkins, T. Gerrits, S. W. Nam, *et al.*, "Highly efficient heralding of entangled single photons," *Optics express*, vol. 21, no. 6, pp. 6707–6717, 2013.

[79] Thorlabs, "Electro-optic amplitude modulator user guide," *www.thorlabs.com*, vol. 1, no. 1, p. 5, 2012. Available at `https://www.thorlabs.com/drawings/6ae15ce037144017-78AC2A7C-EB50-44F0-3F9A9388B7184128/EO-AM-NR-C1-Manual.pdf`.

[80] T. Pittman, Y. Shih, D. Strekalov, and A. Sergienko, "Optical imaging by means of two-photon quantum entanglement," *Physical Review A*, vol. 52, no. 5, p. R3429, 1995.

[81] G. B. Lemos, V. Borish, G. D. Cole, S. Ramelow, R. Lapkiewicz, and A. Zeilinger, "Quantum imaging with undetected photons," *Nature*, vol. 512, no. 7515, pp. 409–412, 2014.

[82] S. Slussarenko, M. M. Weston, H. M. Chrzanowski, L. K. Shalm, V. B. Verma, S. W. Nam, and G. J. Pryde, "Unconditional violation of the shot-noise limit in photonic quantum metrology," *Nature Photonics*, vol. 11, no. 11, p. 700, 2017.

[83] N. Samantaray, I. Ruo-Berchera, A. Meda, and M. Genovese, "Realization of the first sub-shot-noise wide field microscope," *Light: Science & Applications*, vol. 6, no. 7, p. e17005, 2017.

[84] P.-A. Moreau, J. Sabines-Chesterking, R. Whittaker, S. K. Joshi, P. M. Birchall, A. McMillan, J. G. Rarity, and J. C. Matthews, "Demonstrating an absolute quantum advantage in direct absorption measurement," *Scientific Reports*, vol. 7, no. 1, p. 6256, 2017.

[85] E. Losero, I. Ruo-Berchera, A. Meda, A. Avella, and M. Genovese, "Unbiased estimation of an optical loss at the ultimate quantum limit with twin-beams," *arXiv preprint arXiv:1710.09307*, 2017.

[86] M. F. Duarte, M. A. Davenport, D. Takhar, J. N. Laska, T. Sun, K. F. Kelly, and R. G. Baraniuk, "Single-pixel imaging via compressive sampling," *IEEE signal processing magazine*, vol. 25, no. 2, pp. 83–91, 2008.

[87] T. S. Iskhakov, V. C. Usenko, U. L. Andersen, R. Filip, M. V. Chekhova, and G. Leuchs, "Heralded source of bright multi-mode mesoscopic sub-poissonian light," *Optics letters*, vol. 41, no. 10, pp. 2149–2152, 2016.

[88] N. Gisin, G. Ribordy, W. Tittel, and H. Zbinden, "Quantum cryptography," *Reviews of modern physics*, vol. 74, no. 1, p. 145, 2002.

[89] J. L. O'brien, A. Furusawa, and J. Vučković, "Photonic quantum technologies," *Nature Photonics*, vol. 3, no. 12, p. 687, 2009.

[90] V. Giovannetti, S. Lloyd, and L. Maccone, "Advances in quantum metrology," *Nature photonics*, vol. 5, no. 4, p. 222, 2011.

[91] A. E. Lita, A. J. Miller, and S. W. Nam, "Counting near-infrared single-photons with 95% efficiency," *Optics express*, vol. 16, no. 5, pp. 3032–3040, 2008.

[92] R. H. Hadfield, "Single-photon detectors for optical quantum information applications," *Nature photonics*, vol. 3, no. 12, p. 696, 2009.

[93] I. Aharonovich, D. Englund, and M. Toth, "Solid-state single-photon emitters," *Nature Photonics*, vol. 10, no. 10, p. 631, 2016.

[94] E. Moreau, I. Robert, J. Gérard, I. Abram, L. Manin, and V. Thierry-Mieg, "Single-mode solid-state single photon source based on isolated quantum dots in pillar microcavities," *Applied Physics Letters*, vol. 79, no. 18, pp. 2865–2867, 2001.

[95] R. S. Bennink, "Optimal collinear gaussian beams for spontaneous parametric down-conversion," *Physical Review A*, vol. 81, no. 5, p. 053805, 2010.

[96] S. Unsleber, Y.-M. He, S. Gerhardt, S. Maier, C.-Y. Lu, J.-W. Pan, N. Gregersen, M. Kamp, C. Schneider, and S. Höfling, "Highly indistinguishable on-demand resonance fluorescence photons from a deterministic quantum dot micropillar device with 74% extraction efficiency," *Optics express*, vol. 24, no. 8, pp. 8539–8546, 2016.

[97] M. Giustina, M. A. Versteegh, S. Wengerowsky, J. Handsteiner, A. Hochrainer, K. Phelan, F. Steinlechner, J. Kofler, J.-Å. Larsson, C. Abellán, *et al.*, "Significant-loophole-free test of bell's theorem with entangled photons," *Physical review letters*, vol. 115, no. 25, p. 250401, 2015.

[98] L. K. Shalm, E. Meyer-Scott, B. G. Christensen, P. Bierhorst, M. A. Wayne, M. J. Stevens, T. Gerrits, S. Glancy, D. R. Hamel, M. S. Allman, *et al.*, "Strong loophole-free test of local realism," *Physical review letters*, vol. 115, no. 25, p. 250402, 2015.

[99] M. Pant, D. Towsley, D. Englund, and S. Guha, "Percolation thresholds for photonic quantum computing," *arXiv preprint arXiv:1701.03775*, 2017.

[100] T. Guerreiro, A. Martin, B. Sanguinetti, N. Bruno, H. Zbinden, and R. Thew, "High efficiency coupling of photon pairs in practice," *Optics express*, vol. 21, no. 23, pp. 27641–27651, 2013.

[101] H. E. Guilbert and D. J. Gauthier, "Enhancing heralding efficiency and biphoton rate in type-i spontaneous parametric down-conversion," *IEEE Journal of Selected Topics in Quantum Electronics*, vol. 21, no. 3, pp. 215–224, 2015.

[102] D. Ljunggren and M. Tengner, "Optimal focusing for maximal collection of entangled narrow-band photon pairs into single-mode fibers," *Physical Review A*, vol. 72, no. 6, p. 062301, 2005.

[103] C. Branciard, E. G. Cavalcanti, S. P. Walborn, V. Scarani, and H. M. Wiseman, "One-sided device-independent quantum key distribution: Security, feasibility, and the connection with steering," *Physical Review A*, vol. 85, no. 1, p. 010301, 2012.

[104] F. Kaneda, K. Garay-Palmett, A. B. U'Ren, and P. G. Kwiat, "Heralded single-photon source utilizing highly nondegenerate, spectrally factorable spontaneous parametric downconversion," *Optics express*, vol. 24, no. 10, pp. 10733–10747, 2016.

[105] N. Montaut, L. Sansoni, E. Meyer-Scott, R. Ricken, V. Quiring, H. Herrmann, and C. Silberhorn, "High-efficiency plug-and-play source of heralded single photons," *Physical Review Applied*, vol. 8, no. 2, p. 024021, 2017.

[106] M. D. C. Pereira, F. E. Becerra, B. L. Glebov, J. Fan, S. W. Nam, and A. Migdall, "Demonstrating highly symmetric single-mode, single-photon heralding efficiency in spontaneous parametric downconversion," *Optics letters*, vol. 38, no. 10, pp. 1609–1611, 2013.

[107] A. B. U'Ren, C. Silberhorn, K. Banaszek, and I. A. Walmsley, "Efficient conditional preparation of high-fidelity single photon states for fiber-optic quantum networks," *Physical review letters*, vol. 93, no. 9, p. 093601, 2004.

[108] M. M. Weston, H. M. Chrzanowski, S. Wollmann, A. Boston, J. Ho, L. K. Shalm, V. B. Verma, M. S. Allman, S. W. Nam, R. B. Patel, *et al.*, "Efficient and pure femtosecond-pulse-length source of polarization-entangled photons," *Optics express*, vol. 24, no. 10, pp. 10869–10879, 2016.

[109] C. H. Monken, P. S. Ribeiro, and S. Pádua, "Transfer of angular spectrum and image formation in spontaneous parametric down-conversion," *Physical Review A*, vol. 57, no. 4, p. 3123, 1998.

[110] R. Fickler, M. Ginoya, and R. W. Boyd, "Custom-tailored spatial mode sorting by controlled random scattering," *Physical Review B*, vol. 95, no. 16, p. 161108, 2017.

[111] K. Shalm, "Spdcalc," March 2018. Available at `http://spdcalc.org/#`.

[112] A. Assion, T. Baumert, M. Bergt, T. Brixner, B. Kiefer, V. Seyfried, M. Strehle, and G. Gerber, "Control of chemical reactions by feedback-optimized phase-shaped femtosecond laser pulses," *Science*, vol. 282, no. 5390, pp. 919–922, 1998.

[113] A. Seri, A. Lenhard, D. Rieländer, M. Gündoğan, P. M. Ledingham, M. Mazzera, and H. de Riedmatten, "Quantum correlations between single telecom photons and a multimode on-demand solid-state quantum memory," *Physical Review X*, vol. 7, no. 2, p. 021028, 2017.

[114] S. A. Aljunid, G. Maslennikov, Y. Wang, H. L. Dao, V. Scarani, and C. Kurtsiefer, "Excitation of a single atom with exponentially rising light pulses," *Physical review letters*, vol. 111, no. 10, p. 103001, 2013.

[115] P. Powers, T. J. Kulp, and S. Bisson, "Continuous tuning of a continuous-wave periodically poled lithium niobate optical parametric oscillator by use of a fan-out grating design," *Optics letters*, vol. 23, no. 3, pp. 159–161, 1998.

[116] F. Steinlechner, O. de Vries, N. Fleischmann, E. Wille, E. Beckert, and R. Ursin, "Development of a space-proof polarization-entangled photon source," in *Lasers and Electro-Optics (CLEO), 2016 Conference on*, pp. 1–2, IEEE, 2016.

[117] H. Pourbeyram and A. Mafi, "Photon pair generation in multimode optical fibers via intermodal phase matching," *Physical Review A*, vol. 94, no. 2, p. 023815, 2016.

[118] S. Reitzenstein and A. Forchel, "Quantum dot micropillars," *Journal of Physics D: Applied Physics*, vol. 43, no. 3, p. 033001, 2010.

[119] P. M. Birchall, J. Sabines-Chesterking, J. L. O'Brien, H. Cable, and J. C. Matthews, "Beating the shot-noise limit with sources of partially-distinguishable photons," *arXiv preprint arXiv:1603.00686*, 2016.

[120] V. Giovannetti, S. Lloyd, and L. Maccone, "Quantum-enhanced measurements: beating the standard quantum limit," *Science*, vol. 306, no. 5700, pp. 1330–1336, 2004.

[121] S. Knysh, V. N. Smelyanskiy, and G. Durkin, "Scaling laws for precision in quantum interferometry and bifurcation landscape of the optimal state," *Phys. Rev. A*, vol. 83, p. 021804, 2011.

[122] R. Demkowicz-Dobrzański, J. Kołodyński, and M. Guţă, "The elusive heisenberg limit in quantum-enhanced metrology," *Nature communications*, vol. 3, p. 1063, 2012.

[123] H. Lee, P. Kok, and J. P. Dowling, "A quantum rosetta stone for interferometry," *Journal of Modern Optics*, vol. 49, no. 14-15, pp. 2325–2338, 2002.

[124] M. Müller, H. Vural, C. Schneider, A. Rastelli, O. Schmidt, S. Höfling, and P. Michler, "Quantum-dot single-photon sources for entanglement enhanced interferometry," *Physical review letters*, vol. 118, no. 25, p. 257402, 2017.

[125] C. Xiong, X. Zhang, Z. Liu, M. Collins, A. Mahendra, L. Helt, M. Steel, D.-Y. Choi, C. Chae, P. Leong, *et al.*, "Active temporal multiplexing of indistinguishable heralded single photons," *Nature communications*, vol. 7, 2016.

[126] W. Gao, P. Fallahi, E. Togan, A. Delteil, Y. Chin, J. Miguel-Sanchez, and A. Imamoğlu, "Quantum teleportation from a propagating photon to a solid-state spin qubit," *Nature communications*, vol. 4, p. 2744, 2013.

[127] M. Reindl, K. D. Jöns, D. Huber, C. Schimpf, Y. Huo, V. Zwiller, A. Rastelli, and R. Trotta, "Phonon-assisted two-photon interference from remote quantum emitters," *Nano Letters*, 2017.

[128] C.-K. Hong, Z.-Y. Ou, and L. Mandel, "Measurement of subpicosecond time intervals between two photons by interference," *Physical review letters*, vol. 59, no. 18, p. 2044, 1987.

[129] T. Close, E. M. Gauger, and B. W. Lovett, "Overcoming phonon-induced dephasing for indistinguishable photon sources," *New Journal of Physics*, vol. 14, no. 11, p. 113004, 2012.

[130] Y.-S. Ra, M. C. Tichy, H.-T. Lim, O. Kwon, F. Mintert, A. Buchleitner, and Y.-H. Kim, "Observation of detection-dependent multi-photon coherence times," *Nature communications*, vol. 4, p. 2451, 2013.

[131] Z.-Y. J. Ou, *Multi-photon quantum interference*. Springer, 2007.

[132] G.-Y. Xiang, B. L. Higgins, D. Berry, H. M. Wiseman, and G. Pryde, "Entanglement-enhanced measurement of a completely unknown optical phase," *Nature Photonics*, vol. 5, no. 1, pp. 43–47, 2011.

[133] J. C. Matthews, X.-Q. Zhou, H. Cable, P. J. Shadbolt, D. J. Saunders, G. A. Durkin, G. J. Pryde, and J. L. O'Brien, "Towards practical quantum metrology with photon counting," *npj Quantum Information*, vol. 2, p. 16023, 2016.

[134] T. Pittman, D. Strekalov, A. Migdall, M. Rubin, A. Sergienko, and Y. Shih, "Can two-photon interference be considered the interference of two photons?," *Physical Review Letters*, vol. 77, no. 10, p. 1917, 1996.

[135] S. Shwartz, R. Coffee, J. Feldkamp, Y. Feng, J. Hastings, G. Yin, and S. Harris, "X-ray parametric down-conversion in the langevin regime," *Physical review letters*, vol. 109, no. 1, p. 013602, 2012.

[136] D. Klyshko, "Utilization of vacuum fluctuations as an optical brightness standard," *Soviet Journal of Quantum Electronics*, vol. 7, no. 5, p. 591, 1977.

[137] J. G. Rarity, K. D. Ridley, and P. Tapster, "Absolute measurement of detector quantum efficiency using parametric downconversion," *Applied Optics*, vol. 26, no. 21, pp. 4616–4619, 1987.

[138] A. Migdall, "Absolute quantum efficiency measurements using correlated photons: A study of systematics," in *Precision Electromagnetic Measurements Digest, 2000 Conference on*, pp. 347–348, IEEE, 2000.

[139] J. Reingruber, D. Holcman, and G. L. Fain, "How rods respond to single photons: Key adaptations of a g-protein cascade that enable vision at the physical limit of perception," *Bioessays*, vol. 37, no. 11, pp. 1243–1252, 2015.

[140] F. Rieke and D. A. Baylor, "Single-photon detection by rod cells of the retina," *Reviews of Modern Physics*, vol. 70, no. 3, p. 1027, 1998.

[141] D. Takeshita, L. Smeds, and P. Ala-Laurila, "Processing of single-photon responses in the mammalian on and off retinal pathways at the sensitivity limit of vision," *Phil. Trans. R. Soc. B*, vol. 372, no. 1717, p. 20160073, 2017.

[142] R. M. Holmes, R. F. Wang, and P. G. Kwiat, "Correspondence: Still no evidence for single photon detection by humans," *arXiv preprint arXiv:1707.09341*, 2017.

[143] P. C. Nelson, "Old and new results about single-photon sensitivity in human vision," *Physical biology*, vol. 13, no. 2, p. 025001, 2016.

[144] K. E. Dorfman, F. Schlawin, and S. Mukamel, "Nonlinear optical signals and spectroscopy with quantum light," *Reviews of Modern Physics*, vol. 88, no. 4, p. 045008, 2016.

[145] H. C. H. Chan, O. E. Gamel, G. R. Fleming, and K. B. Whaley, "Single-photon absorption by single photosynthetic light-harvesting complexes," *Journal of Physics B: Atomic, Molecular and Optical Physics*, vol. 51, no. 5, p. 054002, 2018.

[146] P. M. Birchall, J. L. O'Brien, J. C. Matthews, and H. Cable, "Quantum-classical boundary for precision optical phase estimation," *Physical Review A*, vol. 96, no. 6, p. 062109, 2017.

[147] J. Aasi, J. Abadie, B. Abbott, R. Abbott, T. Abbott, M. Abernathy, C. Adams, T. Adams, P. Addesso, R. Adhikari, *et al.*, "Enhanced sensitivity of the ligo gravitational wave detector by using squeezed states of light," *Nature Photonics*, vol. 7, no. 8, p. 613, 2013.

[148] H. Yonezawa, D. Nakane, T. A. Wheatley, K. Iwasawa, S. Takeda, H. Arao, K. Ohki, K. Tsumura, D. W. Berry, T. C. Ralph, *et al.*, "Quantum-enhanced optical-phase tracking," *Science*, vol. 337, no. 6101, pp. 1514–1517, 2012.

[149] K. Schneider, R. Bruckmeier, H. Hansen, S. Schiller, and J. Mlynek, "Bright squeezed-light generation by a continuous-wave semimonolithic parametric amplifier," *Optics letters*, vol. 21, no. 17, pp. 1396–1398, 1996.

[150] M. Xiao, L.-A. Wu, and H. Kimble, "Detection of amplitude modulation with squeezed light for sensitivity beyond the shot-noise limit," *Optics letters*, vol. 13, no. 6, pp. 476–478, 1988.

[151] P. Eisenberger and S. McCall, "X-ray parametric conversion," *Physical Review Letters*, vol. 26, no. 12, p. 684, 1971.